공학박사 학위논문

Realization of Structural Colors and Dual Image Storage Based on Optical Micro-resonators

광학 공진기 기반 구조색 및 이중 이미지 저장 기술 연구

2016 년 8 월

서울대학교 대학원

공과대학 전기·컴퓨터공학부

이 인 호

Realization of Structural Colors and Dual Image Storage Based on Optical Micro-resonators

지도교수 이 신 두

이 논문을 공학박사 학위논문으로 제출함

2016 년 8 월

서울대학교 대학원

공과대학 전기·컴퓨터공학부

이 인 호

이인호의 공학박사 학위논문을 인준함

2016 년 6 월

위 원 장 이 병 호 (인)

부위원장 이 신 두 (인)

위 원 박 남 규 (인)

위 원 최 종 선 (인)

위 원 김 학 린 (인)

Abstract

Realization of Structural Colors and Dual Image Storage Based on Optical Micro-resonators

In-Ho Lee

Department of Electrical Engineering and Computer Science

Graduate School

Seoul National University

Recently, structural color has attracted tremendous interest owing to its potential as an alternative to colorant pigment. In contrast to conventional coloration where color is primarily determined by the intrinsic optical absorption of chemical pigments, structural colors arise from the resonant interaction of light with optical nanostructures. Accordingly, structural coloration has several unique features, being differentiated from chemical pigmentation. First of all, any materials can be used for coloration giving more flexibility in material choice. Secondly, overall optical efficiency is relatively high owing to small optical absorption. Thirdly, the size of color pixel can be miniaturized into the scale of diffraction limit. Fourthly, color can change in response to external input by employing active materials. Owing to these

attributes, structural colors are anticipated as new platform for the development of highly efficient nanoscale color devices as well as novel application areas that are inaccessible with conventional technologies.

Toward the realization of structural colors, there have been largely three strategies according to device platform; photonic crystals, plasmonic nanostructures, and optical micro-resonators. Among them, optical micro-resonators have been considered the most promising owing to high optical efficiency, simple fabrication process, and polarization-independent optical properties. For practical applications, however, several technical issues should be addressed. Firstly, low-cost and high-throughput color integration techniques should be developed. Secondly, the color properties such as angle-dependency and color gamut should be improved. Thirdly, new functionalities such as dynamic tunability should be imposed for use in more broad range of applications.

In this thesis, we investigate new device architecture and fabrication techniques to resolve above mentioned technical issues and by extension, develop novel applications by making use of these approaches. First, we present simple and powerful fabrication method based on a series of transfer printings of dielectric materials for the large-area integration of different color elements. By using proposed technique, we demonstrate the prototype of LCDs incorporating color filters based on optical micro-resonators. Toward improving optical properties, we investigate the effect of embedding metallic nanostructure as a phase-shifting element inside resonant cavity. Depending on the geometrical structure of metallic nanostructure, the resonant peak shifts to

longer or shorter wavelengths. The ultrathin thickness of a phase shifting element allows for the integration of different color elements as well as the extension of color palette within a uniform thickness of resonant cavity. Moreover, we demonstrate a flexible color element showing no color change during being bent by adopting metallic nanoislands that significantly reduce the angle dependency. Lastly, we also demonstrate novel polarization-tunable color elements having a liquid crystal polymer layer for resonant cavity. Color elements that have different directions of optical anisotropy can be easily integrated on a single substrate by using a series of photoalignment processes. This feature allows for recording two different images within the same device area and resolving them by applying different polarizations.

The new device architectures and fabrication techniques presented here would pave the way toward the practical implementation of structural colors for a wide range of visual applications ranging from color image storage to advanced display systems.

Keywords: Structural color, Optical micro-resonator, Fabry-Perot resonator, Optical image storage, Color filter

Student Number: 2012-30223

Contents

List of Figures

Chapter 1. Introduction

Color is one of the most fundamental attributes governing human visual perception. Although its definition should include human factors such as the spectral sensitivity of light receptors in eyes, it basically has one-to-one correspondence to certain electromagnetic spectrum of wavelengths ranging from 390 nm to 700 nm in a physical sense. This narrow portion of electromagnetic spectrum, called visible wavelengths, has intrigued human beings since ancient times. Particularly, a major concern has been the reproduction of colors in nature for use in paintings and decorating a variety of objects such as costumes and furniture. The longstanding interest in color has motivated the rapid advance of chemical pigment technology allowing for the reproduction of most natural colors and even, new ones that do not exist in nature. Until very recently, however, some colored surfaces in nature such as iridescent wings of Morpho Butterfly remain inaccessible with human technologies, arousing curiosity about its physical origin.

The iridescent wing of Morpho Butterfly is a typical example of structurally colored surface. In contrast to conventional coloration based on the absorption of certain portion of visible spectrum, the structural colors are produced by light interaction with nanostructured surface. In the case of Morpho species of butterflies, the structural colors arise from thin-film interference in the alternate layers of cuticle and air. Although these butterflies are the most famous creatures in this field, there are a lot of other animals, plants,

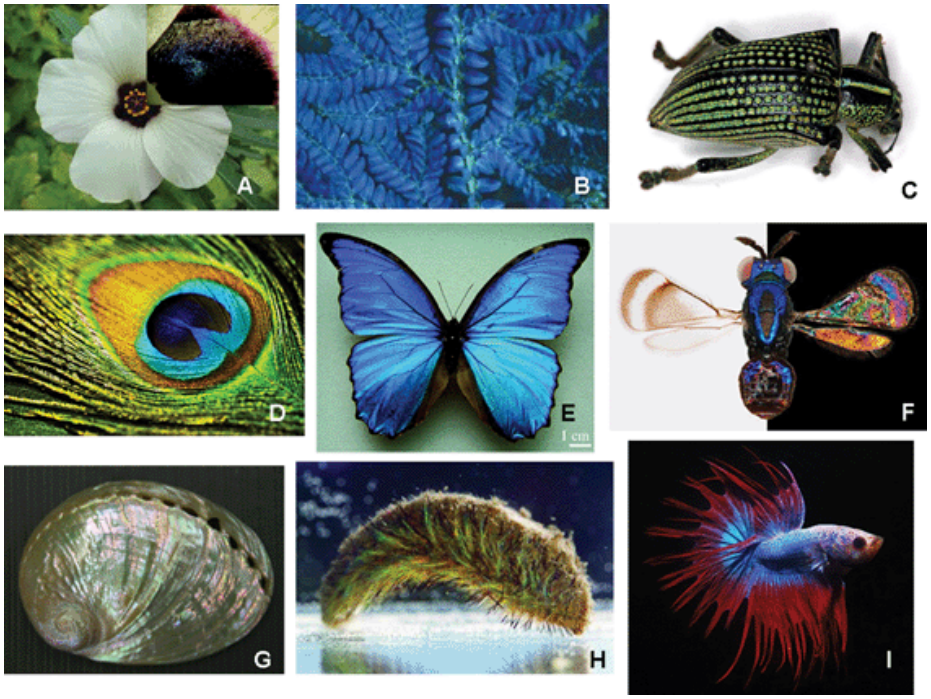

Figure 1.1: Structural colorations in nature [1]. (a) Base of *H. trionum* petal; (b) the fern-like tropical understory plants of the genus *Selaginella*; (c) the diamond weevil beetle, *Entimus imperialis*; (d) the male peacock's tail feathers; (e) broad blue dorsal wing color of the blue butterfly *Morpho rhetenor*; (f) *Closterocerus coffeellae* (Hymenoptera insect; (g) the polished shell of a mollusk, the nacre of *Haliotis glabra*; (h) hollow nanofiber bristles of *Aphrodita aculeata* (a species of sea mouse); (i) siamese fighting fish (*Betta splendens*).

and insects having structurally colored skins or feathers as shown in Fig. 1.1 [1]. Among them, some species can even change their skin colors to blend into environment for protecting themselves from predators.

Besides scientific interest, the structural colors are of engineering importance owing to several unique features compared to chemical pigmentation. First of all, any materials can be used for coloration giving more flexibility in material choice. Secondly, overall optical efficiency is relatively high owing to the suppression of optical absorption. Thirdly, the size of color pixel can be miniaturized into the scale of diffraction limit. Fourthly, color can change in response to external input by employing active materials. Owing to these attributes, structural coloration has been considered as an alternative to chemical pigmentation.

In this thesis, we investigate new device architecture and fabrication techniques toward the realization of artificial structural colors based on optical micro-resonators (OMRs). The effect of metallic nanostructures inside resonant cavity (RC) is numerically and experimentally studied to improve the optical properties of structural colors including color gamut and angle-dependency. For the integration of different color elements, simple patterning technique based on transfer printing is developed, which are applicable over large area in a massively parallel manner. We also demonstrate the novel concept of recording two different images within the same device area and resolving them by the polarization direction of incident light.

1.1. Mechanisms of structural color

Until now, there have been a number of approaches toward realizing artificial structural colors. These approaches can be largely divided into three categories according to device platform: photonic crystals (PCs), plasmonic

nanostructures, and OMRs. In this section, we briefly introduce the physical mechanisms underlying these types of structural colors.

Photonic crystals

The PC is a periodic optical nanostructure that influences the propagation of light in much the same way that atomic crystals does to electrons. In an analogy with electronic band gap, the photonic bandgap prohibits the transmission of certain wavelength bands [2]. In particular, the formation of photonic bandgap at visible wavelengths leads to the generation of reflective-type color [3-6]. Depending on the geometrical structure of PC, the number of dimensions in which photonic bandgap exists can vary from one to three as shown in Fig. 1.2(a) [5].

For the fabrication of PCs in various dimensions, numerous approaches have been demonstrated, most of which rely on bottom-up process due to the difficulty of three dimensional patterning in subwavelength scale [7]. For examples, colloidal particle assembly has been extensively studied for three dimensional PCs [4, 6, 8] while the spin-coating of multilayer films and the fixation of magnetically aligned nanoparticles have been demonstrated for one dimensional case [9, 10]. The PC-based structural colors exhibit high optical efficiency since no metallic part is involved. However, their complicated structure results in relatively bulky size, the complexity of fabrication and integration, and poor optical properties due to defect formation.

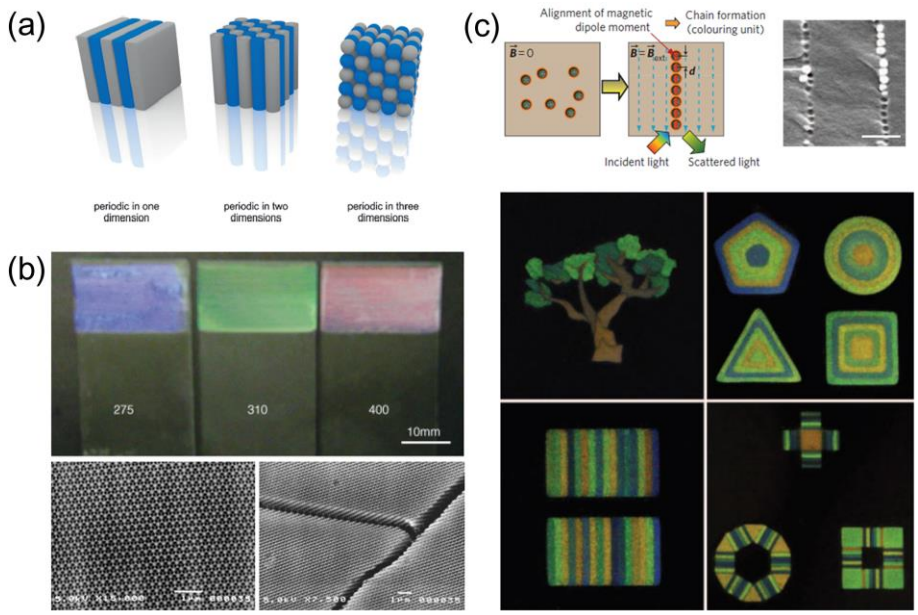

Figure 1.2: Structural colors based photonic crystals (PCs). (a) Three types of PCs depending on the number of periodic dimensions [5]. (b) The structural colors from inverse opal-type PCs fabricated from self-assembled colloidal crystals [8]. Three primary colors are obtained for colloidal particles having different diameters. (c) The structural colors from one-dimensional array of magnetic particles that are aligned under the application of external magnetic fields, and their patterns fabricated by a series of fixation processes by ultraviolet light exposure [10].

Plasmonic nanostructures

In plasmonic nanostructures, colors are generated owing to the excitation of surface plasmons (SPs), which is the collective oscillation of electrons coupled with incident electromagnetic wave [11]. Among various geometries, there are mainly two types of metallic nanostructures supporting color filtering function, i.e., periodic nanoholes perforated onto metallic thin film [12-16] and discontinuous nanopatterns [17-20]. In the former case, the propagating SPs are launched at specific wavelengths satisfying momentum matching condition under the incidence of white light. SPs propagate along the surface of metallic film and then, are squeezed into nanoholes before being out-coupled at the opposite side of film. The color filtering properties of plasmonic nanoholes and their dependence on periodicity and hole size are shown in Figs. 1.3(a) [12] and 1.3(b) [14]. In the case of discontinuous nanopatterns, the excitation of localized SPs leads to the extinction of certain wavelengths satisfying resonance condition. Owing to high extinction cross-section, the individual nanopattern can be used as a diffraction-limited color pixel as shown in Fig 1.3(c) [17]. Although plasmonic color elements are compact and have suitable design for integration, their optical efficiency is usually low due to significant damping in metallic nanostructures and the fabrication requires high-resolution patterning techniques such as electron beam lithography.

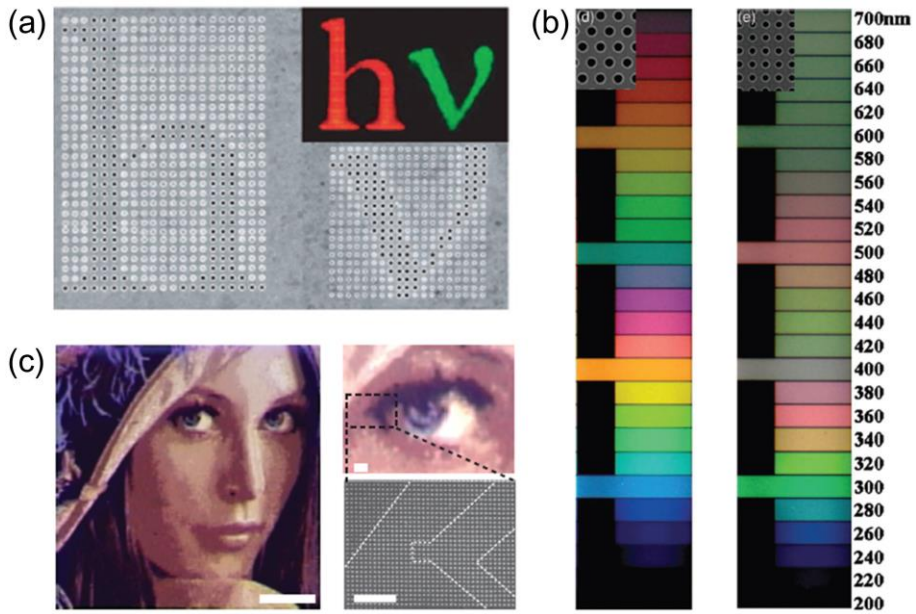

Figure 1.3: Structural colors from plasmonic nanostructures. (a) The structural colors from periodic nanoholes perforated onto metallic film [12]. The periodicity determines the resonance wavelength and resultant color. (b) The effect of lattice structure and periodicity on color palette in the case of periodic nanoholes milled in metallic film [14]. (c) The structural color images are obtained by using a metallic nanodisk as a diffraction-limited color pixel. The color can be tailored by the diameter of nanodisk [17].

Optical micro-resonators

Structural coloration based on OMRs usually relies on etalon-type structure to transmit or reflect certain wavelengths of light satisfying the condition for constructive interference [21-23]. Figure 1.4(a) schematically illustrates a typical OMR including two TRLs and RC between them [21]. Depending on the thickness of RC, different colors are obtained as shown in Fig. 1.4 (b). The advantages of this approach include high optical efficiency and polarization-independent optical property. In contrast to former approaches, in addition, the exceptionally simple metal-dielectric-metal configuration enables low-cost and large-area fabrication of highly uniform structure without any high-resolution techniques. For practical applications, however, challenges still remain in integrating different colors, expanding color palette, reducing angle-dependency, and by extension, exploiting their unique features for the development of novel color devices.

In this thesis, we mainly focus on structural coloration based on OMRs due to their strong potential for practical applications. Before the introduction to OMR-based color elements, we will briefly describe the potential application areas of structural colors in a following section.

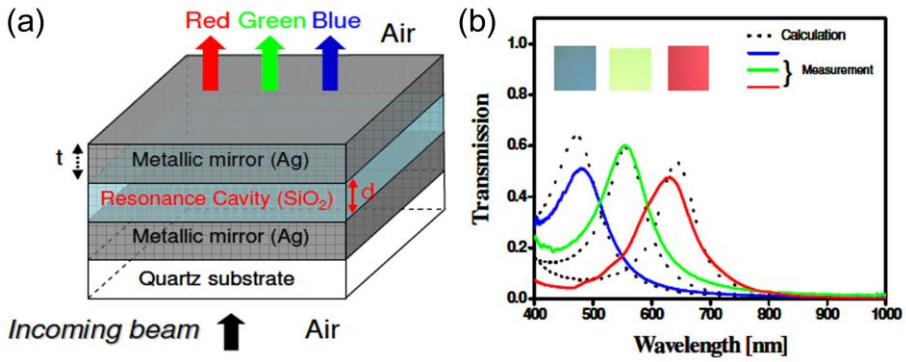

Figure 1.4: The structural colors from OMR [21]. (a) The scheme of OMR supporting Fabry-Perot resonance. Depending on the thickness of RC *d*, different color can be transmitted. (b) The optical transmittances of OMRs having different *d*. Three primary colors of red, green, and blue are obtained.

1.2. Applications of structural color

Color technology has been used in a wide range of visual applications including the coloration of industrial products, paintings and design, and even, electronic products such as color cameras and displays. The development of structural color elements is expected to replace the role of chemical pigment in such application areas. In this section, we introduce several potential application areas of structural colors and relevant research achievements.

Color filter arrays

Color filter arrays (CFAs) are most essential elements for the reproduction of visual information in color cameras and displays. Although there are several types, the most widely used CFAs contain three color elements of red (R), green (G), and blue (B) in a unit pixel. So far, color photoresists containing chemical pigments have been used for manufacturing CFAs [24]. Since this type of CFAs relies on the intrinsic absorption of chemical pigments, the maximum optical efficiency for each primary color is less than 33%. In addition, the fabrication requires at least three times of photolithography to define R, G, and B elements of different color photoresists.

In contrast, the CFAs based structural coloration, in principle, exhibit higher efficiency since it reflect the wavelengths other than those belonging to transmission band. The reflected wavelengths can be recycled after being reflected several times in the interior of electronic system [25, 26]. One of promising approaches toward the realization of CFAs based on structural coloration is to utilize plasmonic nanoholes perforated on metallic thin film.

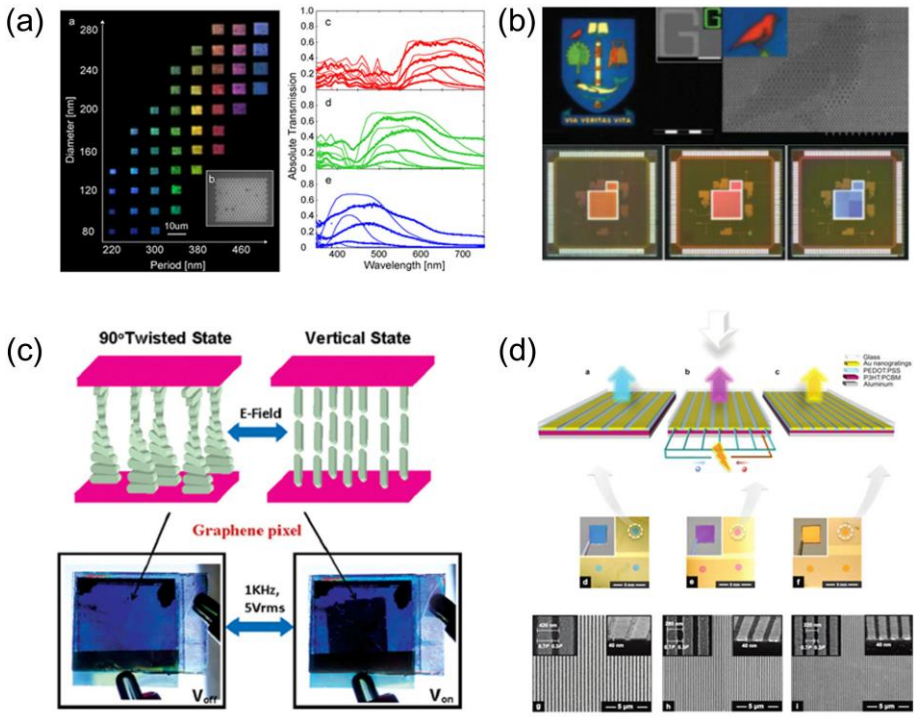

Figure 1.5: The color filter array applications. (a) The color filters based on plasmonic nanohole array [15]. (b) Complementary metal oxide semiconductor (CMOS) image sensors integrated with color filters based on plasmonic nanohole array [16]. (d) Liquid crystal display incorporating the color filter based on etalon-type OMR [27]. (d) Organic solar cells integrated with plasmonic color filters for decorative purpose [28].

This type of CFAs has compact size and allows the one-step integration of different color elements [15]. In particular, the nanoscale confinement of SPs enables the miniaturization of pixel size into the submicrometer scale, making this approach suitable for image sensor application [15, 16, 29].

The OMR-based color elements have also been demonstrated as color filters for liquid crystal displays (LCDs) [27]. This type of color filters can be used simultaneously as an electrode for driving the display systems. In contrast to previous cases where the color filtering function is intrinsically required, some researchers have focused on the decorative use of structural color elements in electronic systems. For examples, there have been several studies regarding the employment of plasmonic color filters into transparent organic solar cells for use in outdoor environment [28, 30].

Color image storage

Color image storage is one of the most feasible applications of structural coloration. Compared to conventional method for image storage, there is less limitation on material choice for substrate and color elements in structural color-based approach [18]. It allows for the employment of highly stable materials such as silicon oxide, benefiting storage time and stability against harsh external conditions such as strong light illumination, chemical solvents and humidity. Another important feature is that the pixel size can be miniaturized into the scale of diffraction-limit that is inaccessible with current technologies such as inkjet printing.

Since the first demonstration [17], there have been a lot of approaches employing an isolated metallic nanopattern as a color pixel [18, 19, 31, 32]. Although metallic nanoparticle itself exhibits coloration effect, small extinction cross-section significantly limits the image contrast. Toward increasing extinction efficiency and thus, image contrast, the reflecting mirror was used at

the rear side of metallic nanopatterns (Fig. 1.6(a)) [19]. In addition to high resolution, structural color-based approach provides the multiplexed storage of color images for high information density. By employing a metallic nanopattern having geometrical asymmetry as a color pixel, two different color images can be stored within the same device area and resolved by polarization [33]. Recently, D. Franklin et al. have also demonstrated the novel concept of actively tunable color images by using liquid crystals on imprinted plasmonic surfaces as shown in Fig. 1.6(c) [34].

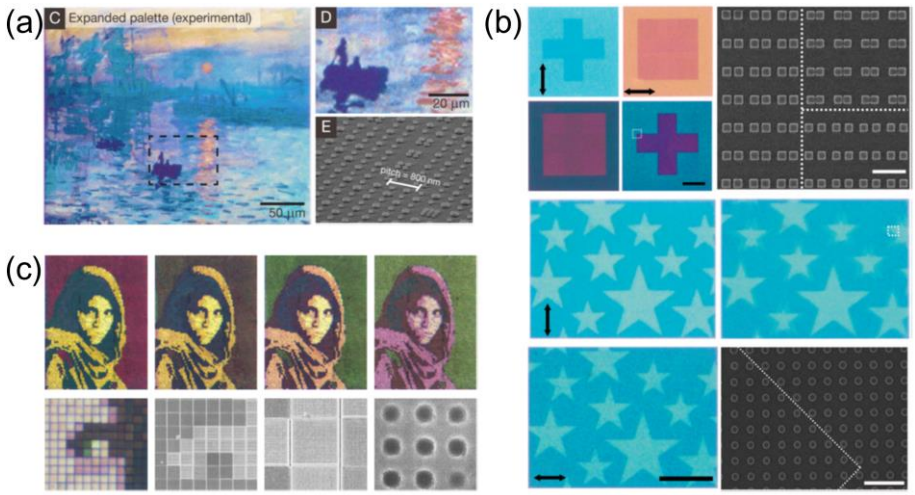

Figure 1.6: Color image storage applications. (a) The artistic color image consisting of color pixels based on metallic nanoparticles [19]. (b) Dual color images resolved by the polarization of incident light [33]. (d) Actively tunable color image based on imprinted plasmonic surfaces in combination with liquid crystal layer [34].

Sensors

In contrast to chemical pigmentation, the structural color can change in response to external stimuli such as mechanical stress [35-37], electric [38-40] and magnetic fields [41-43], the exposure to chemical solvents [44, 45] and humidity [46-48], and the specific binding of biomolecules [49] by adopting active materials. This unique feature allows for the realization of structural color-based sensors that transduce external stimuli into the change of color [45]. Compared to the other approaches, this type of sensors has unique advantages in that it does not consume power for signaling and require external circuitry for transducing signal into recognizable form.

There have been a lot of researches toward the realization of structural color-based sensors for various types of stimuli. The first example illustrated in Fig. 1.7(a) shows the sensing platform for gold nanoparticle-tagged biomolecules [49]. Here, the color properties of plasmonic nanodisks change due to the intercoupling effect when the tagged biomolecules forms specific binding to nearby antibodies. Beside biomolecules, many studies have focused on sensing humidity and chemical solvents by using the materials such as hydrogels and polymers that swell in response to these stimuli.

Usually, PCs have been considered promising for this purpose owing to the absence of metallic parts that forms crack during mechanical deformation. Under the introduction of humidity or chemical solvents, the geometrical structure of PCs changes due to swelling. Figures 1.7(b) [50] and 1.7(c) [51] show the typical examples of humidity and chemical solvent sensors based on one and three dimensional PCs.

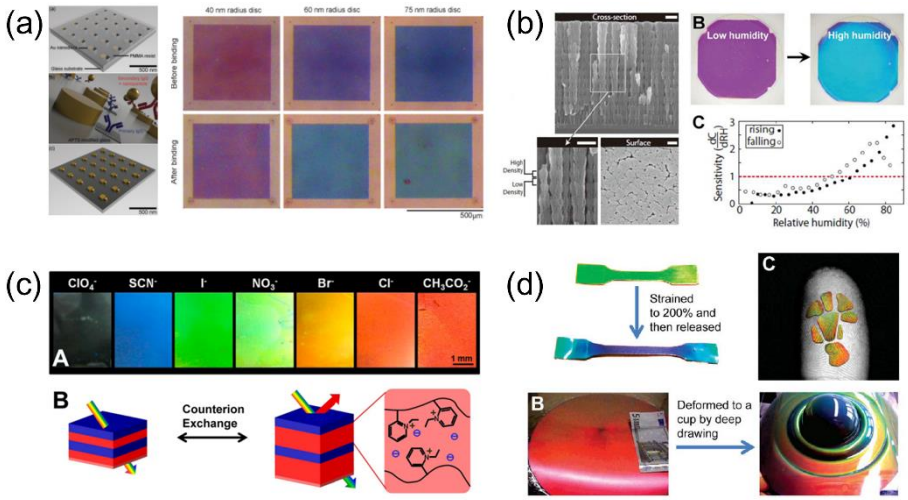

Figure 1.7: Sensing applications of structural colors. (a) Biomolecule sensing platform based on metallic nanodisks [49]. (b) Humidity sensing based on PCs. Color changes from purple to blue under the condition of high humidity [50]. (c) Chemical sensor based on one dimensional PCs [51]. The gel-type layer exhibit the different degree of swelling to different chemical solvents. (d) Mechanical sensor based on PCs [52].

The mechanical flexibility of PCs makes them suitable for mechanical sensing application. Under mechanical stress, the deformation in the lattice structure of PCs is visualized in the form of color change as shown in Fig. 1.7(d) [52].

On the contrary to PCs, plasmonic nanostructures have been exploited into refractive index sensors that response to the change of external environment. This scheme has been utilized for sensing biomolecules and chemical solvents [53-55]. Although the mechanical fragility usually hampers their use for mechanical sensors, some researches demonstrated the embedding metallic

nanostructures into the flexible matrix where the intercoupling effect between them changes upon mechanical deformation [56, 57]. Compared to two former device platforms, only a limited number of researches have focused on adopting OMR-based structural colors for sensing applications.

1.3. Structural colors based on optical micro-resonators

The main advantages of structural color elements based on OMRs are as follows. First of all, its simple structure facilitates the large-area and low-cost fabrication without high resolution patterning techniques. Second, the optical efficiency is relatively high since the optical loss mostly arises during propagation through optically thin reflecting mirrors. Third, their optical property is highly isotropic owing to the geometrical symmetry. Due to these advantages, this type of structural colors has been considered most promising for practical applications.

However, there are several technical issues to be addressed for practical implementation. First of all, it is difficult to integrate different color elements owing to the thickness variation among corresponding OMRs. Since it is essential for many applications such as CFAs for display systems, the integration of different color elements has been a major concern. So far, a few approaches based on a series of vacuum deposition [29, 30] and focused ion beam milling [58] have been demonstrated as shown in Fig. 1.8. However, these approaches inevitably suffer from low throughput and the complexity in fabrication. In addition, the unevenness of final structure leads to the inhomogeneity of electrical performance when incorporated into electro-optic

devices such as LCDs. Therefore, it is a critical challenge to develop simple and high-throughput integration techniques and device configuration that allows the color variation within a uniform thickness for RC.

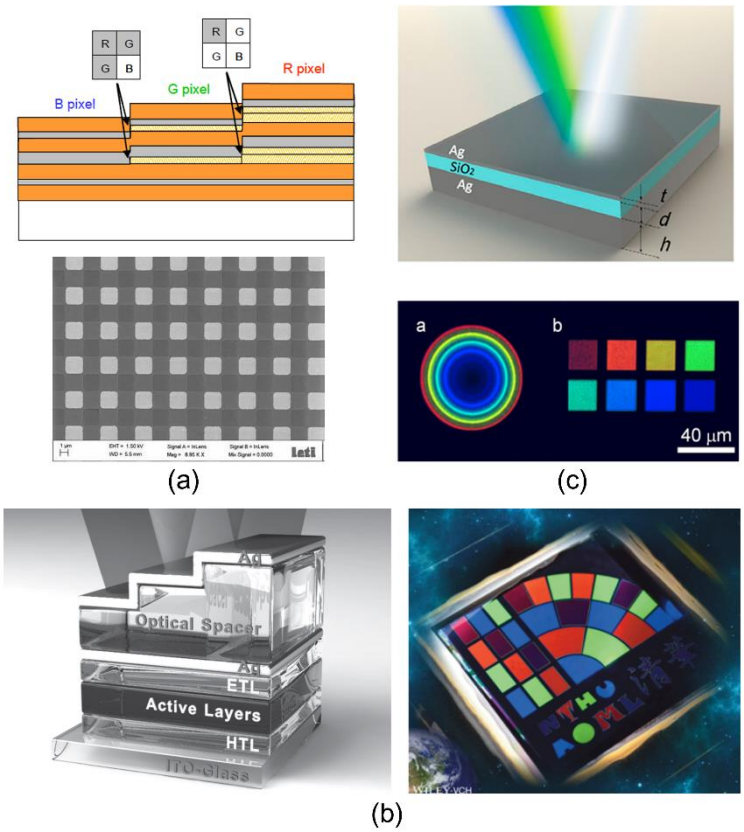

Figure 1.8: Approaches for the integration of different color elements of OMRs. CFA fabricated by a series of depositions of (a) inorganic material layers [29] and (b) transparent organic material layers [30]. (c) CFA fabricated through focused ion beam milling [58].

Another technical issue is to improve the angle dependency, which means how much color changes on different angles of incident light. The angle dependency is attributed to the fact that the resonant peak of an OMR is a cosine function of θ [59]. The simplest approach is to employ a dielectric overlay on the OMR for the impedance matching between color element and external environment as shown in Fig. 1.9(a) [22, 23]. However, the impedance matching condition would be not satisfied when color elements are incorporated into other devices, which significantly limits application range. Another means for impedance matching is stacking several OMRs having different thicknesses (Fig. 1.9(b)) [60]. In this case, the fabrication process of color element and their integration become far more complicated. Recently, the adoption of highly absorbing material such as amorphous silicon for RC has been also demonstrated for the improvement of angular properties but at the expense of significant transmittance (Fig. 1.9(c)) [61-64]. Therefore, new design with low angle dependency is still required, without much altering original device architecture and fabrication/integration process.

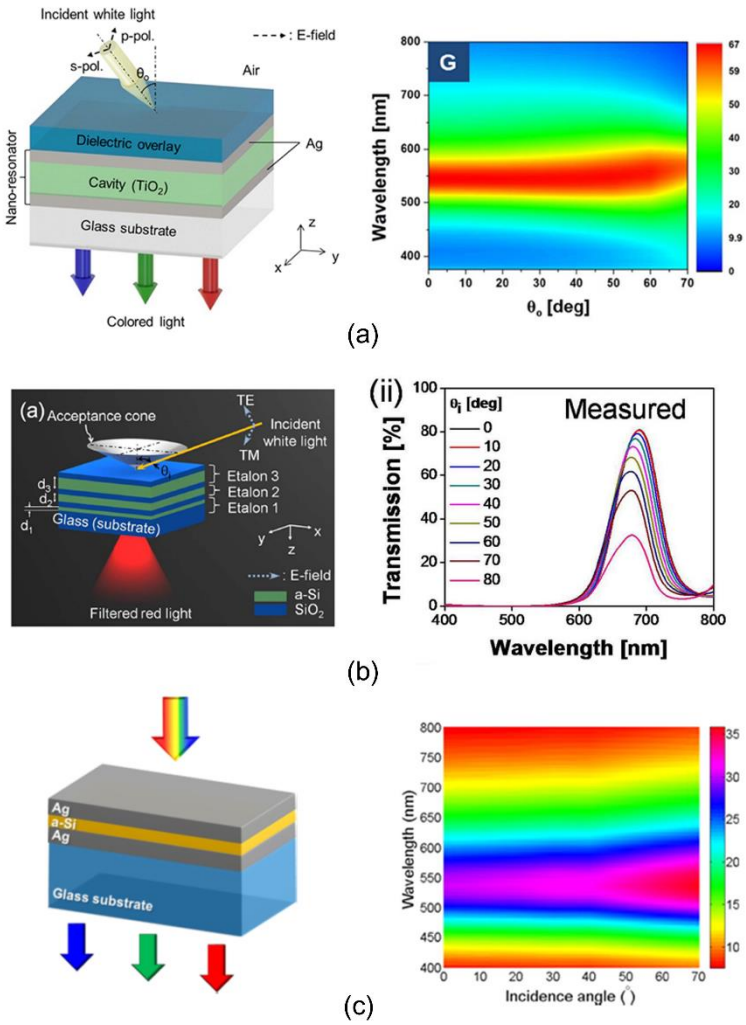

Figure 1.9: Approaches for improving the angular dependency of color property. (a) The employment of dielectric overlay for impedance matching between incident medium and OMR [22]. (b) Multilayer configuration based on stack of OMRs having different thicknesses [60]. (c) The employment of amorphous silicon layer for tailoring phase retardation of incident light during round trip in RC [62].

The last issue is to impose dynamic tunability for use in more broad range of application fields. Since it is one of the most unique features being differentiated from conventional coloration, many research groups have pursued such structural color elements which can be dynamically tunable through various external stimuli including the polarization of incident light, electric and magnetic fields, mechanical stress, and electrochemical reaction.

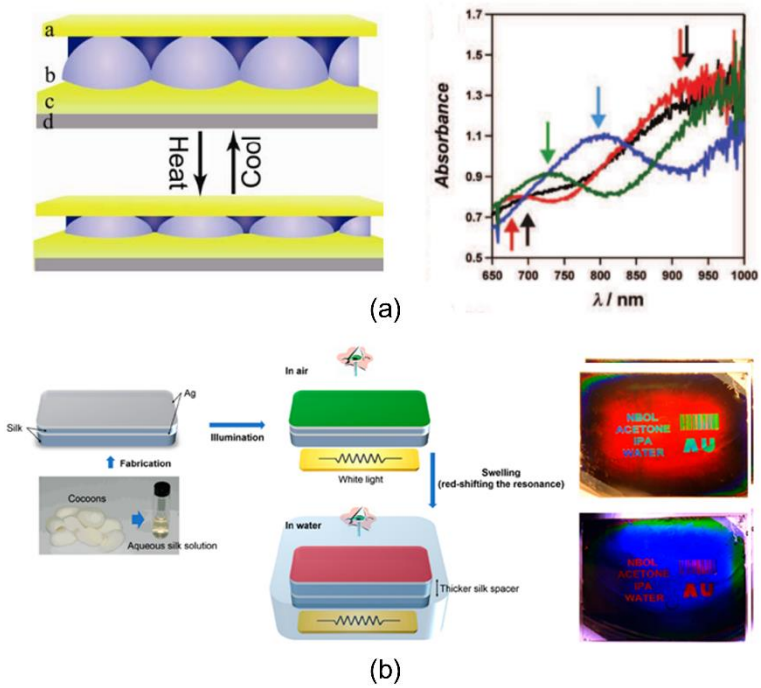

Figure 1.10: Approaches for dynamically tunable color elements based on OMRs [65]. (a) Thermally tunable color element employing temperature-sensitive microgel layer for RC. (b) Chemically tunable color element based on silk RC [66].

In contrast to the other platforms of PCs and plasmonic nanostructures, relatively few researches have focused on OMRs. In order to introduce dynamic tunability, most studies utilize a gel-type layer for RC that swells in response to humidity or chemical solvents as shown Fig. 1.10 [65, 66]. These types of tunable color elements can be utilized for sensing applications that allows for the naked-eye recognition of hazardous chemicals and environmental changes. For versatile use in various applications, the development of new schemes that response to other types of stimuli still remains a challenge.

1.4. Outline of thesis

This thesis contains six chapters including **Introduction** and **Concluding Remarks**. In **Chapter 1**, the general overview of structural colors, with an emphasis on the device platform of OMRs, is introduced. The relevant technical issues and the motivation of this research are also described. In **Chapter 2**, we present the theoretical background of this thesis. The general theory of an etalon-type OMR is described. In addition, the basic principle and mathematical formalism for rigorous coupled wave analysis method used for numerical simulation throughout this thesis are introduced. In **Chapter 3**, we present the simple and powerful fabrication method based on a series of transfer printings of dielectric materials for the large-area integration of different color elements. By using proposed technique, we demonstrate the prototype of LCDs incorporating color filters based on OMRs. In **Chapter 4**, we realize the wide range of color palette covering blue to red by employing metallic nanostructure as a phase-shifting element inside RC. Depending on the geometrical structure

of metallic nanostructure, the resonant peak shifts to longer or shorter wavelengths. The ultrathin thickness of a phase shifting element allows for the integration of different color elements within a uniform thickness for RC. Moreover, we demonstrate a flexible color element showing no color change during being bent by adopting red-shifting phase elements that significantly reduce the angle dependency. **Chapter 5** contains the novel concept of a polarization-tunable color element having a liquid crystal polymer layer for RC. Color elements that have different directions of optical anisotropy can be easily integrated on a single substrate by using a series of photoalignment process. This feature allows for recording two different images within the same device area and resolving them by the polarization direction of incident light. Finally, **Chapter 6** provides the summary and the concluding remarks.

Chapter 2. Theoretical Background

2.1. General theory of etalon-type optical micro-resonators

OMRs, confining light at certain wavelengths within RC, are one of the most fundamental optical components. From the viewpoint of scientific research, it provides viable platform to manipulate the resonant behavior of light. On the other hand, it is also a practically important device for a number of optical applications [67] such as lasers, optical parametric oscillators, and interferometers. Owing to its scientific and engineering importance, OMRs have been extensively studied. Among a number of configurations, the Fabry-Perot resonators or etalon are of the simplest form, consisting of two reflecting mirrors and optical spacer between them.

Until recently, Fabry-Perot resonators have been mostly used to selectively transmit certain bands of wavelengths in telecommunication regime [68, 69]. Since the potential of a Fabry-Perot resonator for structural color element was first demonstrated [21], there have been many studies to further improve this simple but powerful structural color elements. In this section, the general theory of Fabry-Perot resonators in the ray optics picture will be described to understand how they can be implemented as a structural color element. It should be noted that in this thesis, we will use the term OMR for Fabry-Perot resonator without distinction.

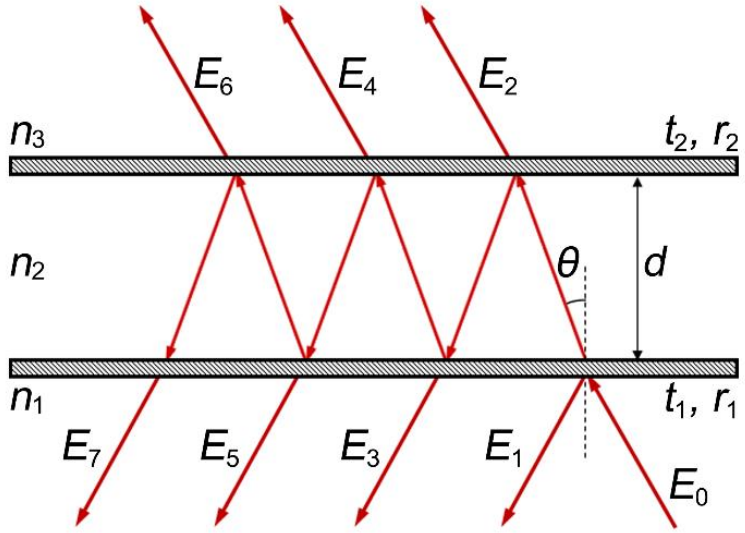

Figure 2.1: Etalon-type OMRs and the propagation of light rays within RC.

Figure 2.1 schematically illustrates the transmission of plane wave having electric field amplitude E_0 and wavelength λ through an OMR. Here, two TRLs having reflection coefficients of r_1 and r_2 as well as transmission coefficients of t_1 and t_2 are separated by the distance d. With respect to these TRLs, space is divided into three regions of incident medium, RC, and propagating medium whose refractive indices are n_1, n_2, and n_3, respectively. Due to the finite magnitude of r_1 and r_2, some of light rays are transmitted into propagating medium while the others reflected back to incident medium after being reflected back and forth several times within RC.

In the case of oblique incidence, in particular, the light rays make an angle of θ with the direction normal to TRLs. Of major interest is the calculation of optical transmittance and reflectance. Here, we will focus on optical transmittance but the mathematical treatment of reflectance is essentially same.

The optical transmittance, T, can be described as the intensity of the sum of light rays in propagating mediums as follows.

$$T = \frac{\left|E_2 + E_4 + E_6 + \cdots + E_{2m} + \cdots\right|^2}{\left|E_0\right|^2} = \frac{\left|\sum_{m=1}^{\infty} E_{2m}\right|^2}{\left|E_0\right|^2}. \tag{2.1}$$

Considering the number of reflections at each reflecting mirror before transmission, the amplitude of mth ray E_{2m} is represented as

$$E_{2m} = t_1 t_2 r_1^{m-1} r_2^{m-1} e^{jk(2m+1)d} E_0 . \tag{2.2}$$

Here, k is wavenumber, given by $2\pi n_2 \cos\theta/\lambda$. Therefore, the sum of transmitted light rays is an infinite geometric series with the start term of $t_1 t_2 E_0 e^{jkd}$ and the common ratio of $r_1 r_2 e^{2kn_2 d}$, which gives

$$T = \frac{T_1 T_2}{1 + R_1 R_2 - 2\sqrt{R_1 R_2}\cos\delta}, \tag{2.3}$$

where T_1, T_2, R_1, and R_2 are $|t_1|^2$, $|t_2|^2$, $|r_1|^2$, and $|r_2|^2$, respectively. δ is total phase difference between two successive rays which is given as

$$\delta = 2kd\cos\theta + \delta_{r1} + \delta_{r2}, \tag{2.4}$$

where δ_{r1} and δ_{r2} are the phase changes on reflection at two reflecting mirrors. As can be seen in Eq. (2.3), T has maxima when δ becomes integer multiples of 2π. From the physical viewpoint, it means that transmitted rays constructively interfere. In terms of wavelength, the condition can be given as

$$n_2 d\cos\theta = \frac{\lambda}{2}\left[m - \sum_l \frac{\delta_l}{2\pi}\right], \tag{2.5}$$

for the integer *m* greater or equal to 0. Eq. (2.3) shows that an OMR indeed exhibits band-pass filtering behavior for certain wavelengths satisfying Eq. (2.5).

Since two TRLs are identical and absorption through them is small in many cases, it is convenient to examine the simplified forms of above equations under these assumptions. In this case, Eq. (2.3) becomes

$$T = \frac{(1-R)^2}{1+R^2-2R\cos\delta}. \tag{2.6}$$

where $R_1 = R_2 = R$. Using the relationship of $\cos\delta = 1\text{-}2\sin^2(\delta/2)$,

$$T = \frac{1}{1+F\sin^2(\delta/2)}. \tag{2.7}$$

where

$$F = \frac{4R}{(1-R)^2} \tag{2.8}$$

is the coefficient of finesse, which determines the quality factor of an etalon-type OMR. Figure 2.2 shows a typical example of optical transmittances calculated from Eq. (2.7). With increasing *F*, the full-width at half maximum (FWHM) becomes small illustrating the role of *F* on quality factor. Since *F* increases with *R*, it means that high reflectance of TRL is advantageous for high quality factor. However, in real case, the increase of reflectance inevitably accompanies that of optical absorption limiting efficiency of system.

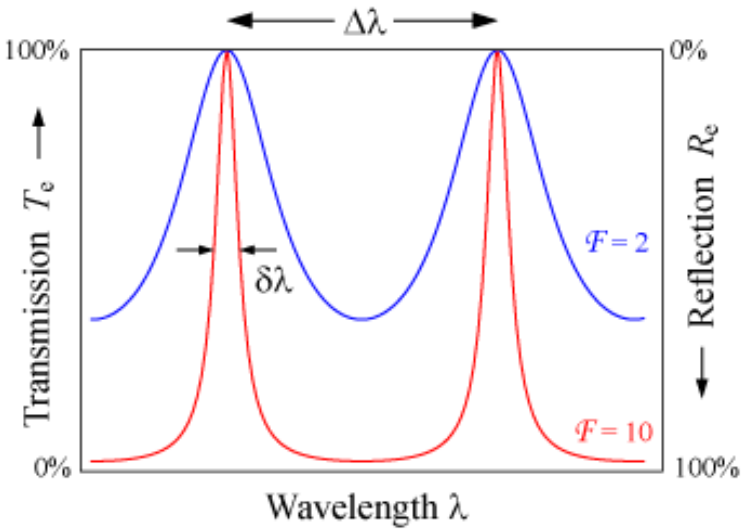

Figure 2.2: A typical example of optical response of etalon-type OMR. With increasing the finesses *F*, the full width at half maximum become small.

For structural color application, a single filtering band in visible regime is advantageous in terms of color purity and flexibility in design. Now we describe the condition that allows the presence of a single filtering band in visible regime. For the derivation of the condition, it is necessary to obtain the expression for the spectral distance between successive resonant peaks, which is called free spectral range $\Delta\lambda_{\mathrm{FSR}}$. From Eq. (2.5) and the assumption that no disperse behavior of δ_m, the spectral distance between *m*th order and (*m*+1)th resonance

$$\Delta\lambda_{\mathrm{FSR}} = \frac{\lambda_m}{m+1-\sum_l \delta_l / 2\pi}. \tag{2.9}$$

Here, λ_m is the peak wavelength for *m*th order. $\Delta\lambda_{\mathrm{FSR}}$ should be larger than the entire range of visible wavelengths, that is about 300 nm, which gives

$$\frac{\lambda_m}{300} \geq m + 1 - \sum_l \delta_l / 2\pi \,, \tag{2.10}$$

In the case of silver, most widely used material for a reflecting mirror, δ_l is about 0.82π at the wavelength of 550 nm. Taking this value for δ_l and considering λ_m ranges from 390 nm to 700 nm, a single band filtering condition is only satisfied for the first order of resonance, i.e., when m = 1. Neglecting δ_l, the corresponding d is about 200 nm at the longest wavelength of 700 nm in visible regime. It indicates that the thickness of RC should be under 200 nm for a single filtering band.

2.2. Rigorous coupled wave analysis

In this section, we introduce the numerical simulation method called rigorous coupled wave analysis (RCWA), which is used throughout this thesis to investigate the color properties of proposed devices. The RCWA provides an exact solution of Maxwell's equations for the electromagnetic problems of diffraction gratings [70, 71]. Compared to the other methods such as finite element method and finite difference time domain method, the RCWA is a relatively straightforward, non-iterative, and deterministic technique [72]. In RCWA, the grating is decomposed into many sufficiently thin planar grating slabs to approximate the original profile. The electromagnetic fields in each slabs are calculated by the coupled-wave method and the continuity of tangential electromagnetic field components are applied at the interfaces between them as well as with input and output regions. As a result, the amplitudes of transmitted or reflected diffraction orders are obtained.

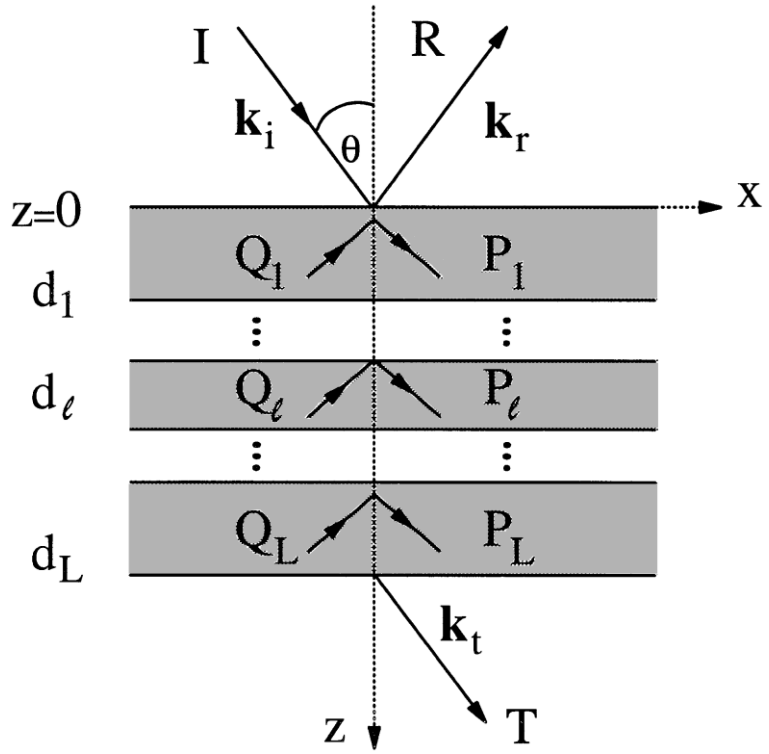

Figure 2.3: Geometry for multilayer of uniform films. The plane wave having the wavenumber of k_i is incident on at the angle of θ [72].

To understand the basic concept of RCWA method, let us consider the simplest case of multilayer of homogeneous films in Fig. 2.3 [72]. When the plane wave polarized in a transverse electric mode is incident at angle θ on L films having refractive indices n_1, …, n_L and thickness d_1, …, d_L as shown in Fig. 2.3. The normalized y component of electric fields in input region (n_I), all films, and output region (n_T) are sequentially given as

$$E_0 = \left(e^{-jk_{I,z}z} + e^{jk_{I,z}z}R\right)e^{-jk_x x}, \tag{2.11}$$

$$E_l = \left\{A_l e^{-k_0\gamma_l(z-D_{l-1})} + B_l e^{k_0\gamma_l(z-D_l)}\right\} e^{-jk_x x}, \tag{2.12}$$

$$E_t = Te^{-j\left\{k_x x + k_{T,z}(z-D_L)\right\}}, \tag{2.13}$$

$$k_0 = 2\pi/\lambda_0,$$

$$k_x = k_0 n_I \sin\theta,$$

$$k_{i,z} = k_0 n_I \cos\theta,$$

$$k_{T,z} = k_0(n_T^2 - n_I^2\sin^2\theta)^{1/2},$$

$$\gamma_l = j(n_l^2 - n_I^2\sin^2\theta)^{1/2},$$

$$D_l = d_1 + d_2 + \ldots + d_l,$$

where R and T are the reflected and transmitted amplitudes, A_l and B_l are the amplitudes in lth slab. Owing to the continuity of tangential electric and magnetic fields, we obtain two equations at $z = 0$,

$$1 + R = A_1 + B_1 e^{-k_0\gamma_1 d_1}, \tag{2.14}$$

$$j(k_{I,z}/k_0)(1-R) = \gamma_1(A_1 - B_1 e^{-k_0\gamma_1 d_1}), \tag{2.15}$$

at the boundaries between films,

$$A_{l-1}e^{-k_0\gamma_{l-1}d_{l-1})} + B_{l-1} = A_l + B_l e^{-k_0\gamma_l d_l}, \tag{2.16}$$

$$\gamma_{l-1}\left(A_{l-1}e^{-k_0\gamma_{l-1}d_{l-1}} - B_{l-1}\right) = \gamma_l\left(A_l - B_l e^{-k_0\gamma_l d_l}\right), \tag{2.17}$$

and at $z = D_L$,

$$A_L e^{-k_0\gamma_L d_L)} + B_L = T, \tag{2.18}$$

$$\gamma_L\left(A_L e^{-k_0\gamma_L d_L} - B_L\right) = j(k_{T,z}/k_0)T. \tag{2.19}$$

In total, 2(L+1) equations are generated. The system of equations can be solved for R or T by using the matrix-based approaches. In the matrix form, for examples, Eqs. (2.16) and (2.17) for l = L are combined to

$$\begin{bmatrix} A_{L\text{-}1} \\ B_{L\text{-}1} \end{bmatrix} = \begin{bmatrix} e^{-k_0\gamma_{L-1}d_{L-1}} & 1 \\ \gamma_{L\text{-}1}e^{-k_0\gamma_{L-1}d_{L\text{-}1}} & -\gamma_{L-1} \end{bmatrix}^{-1} \begin{bmatrix} 1 & e^{-k_0\gamma_L d_L} \\ \gamma_L & -\gamma_L e^{-k_0\gamma_L d_L} \end{bmatrix} \begin{bmatrix} A_L \\ B_L \end{bmatrix}, \tag{2.20}$$

and Eqs. (2.18) and (2.19) give

$$\begin{bmatrix} A_L \\ B_L \end{bmatrix} = \begin{bmatrix} e^{-k_0\gamma_L d_L} & 1 \\ \gamma_L e^{-k_0\gamma_L d_L} & -\gamma_L \end{bmatrix}^{-1} \begin{bmatrix} T \\ j(k_{\mathrm{T},z}/k_0)T \end{bmatrix}. \tag{2.21}$$

Eq. (2.20) can be substituted into Eq. (2.21) and this procedure can be repeated before obtaining the direct relationship between R and T, which is represented by

$$\begin{bmatrix} 1 \\ j(k_{\mathrm{I},z}/k_0) \end{bmatrix} + \begin{bmatrix} R \\ -j(k_{\mathrm{I},z}/k_0)R \end{bmatrix} = \prod_{l=1}^{L} \begin{bmatrix} 1 & e^{-k_0\gamma_l d_l} \\ \gamma_l & -\gamma_l e^{-k_0\gamma_l d_l} \end{bmatrix} \begin{bmatrix} e^{-k_0\gamma_l d_l} & 1 \\ \gamma_l e^{-k_0\gamma_l d_l} & -\gamma_l \end{bmatrix}^{-1} \times \begin{bmatrix} T \\ j(k_{\mathrm{T},z}/k_0)T \end{bmatrix}. \tag{2.22}$$

With all known constants, we can obtain R and T by solving the system of equations given by Eq. (2.22).

Let us now describe the mathematical framework for the calculation of electromagnetic field amplitudes for diffraction gratings having arbitrary profile. Figure 2.4 shows the geometry for the diffraction grating with the periodicity Λ and the depth d under the incidence of plane wave at angle θ. For completeness, the case of transverse-magnetic field is considered here.

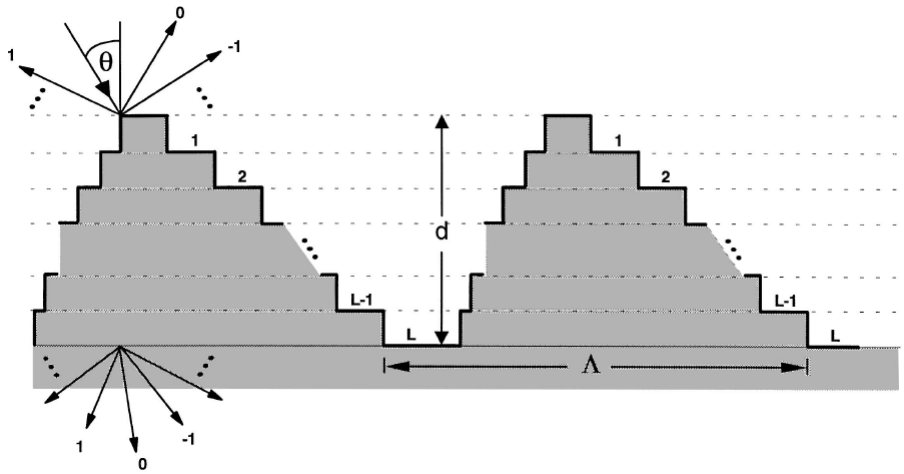

Figure 2.4: Geometry for the problem of diffraction grating having arbitrary profile [72].

In this case, the *y* components of magnetic fields in the incident and transmitted regions are given as

$$H_{\mathrm{I},y} = e^{-jk_0 n_0 (x\sin\theta + z\cos\theta)} + \sum_m R_m e^{-j(k_{xm}x - k_{\mathrm{I},zm})}, \tag{2.23}$$

$$H_{\mathrm{T},y} = \sum_m T_m e^{-j\{k_{xm}x + k_{\mathrm{T},zm}(D_L - z)\}}, \tag{2.24}$$

where R_m and T_m are the normalized magnetic field amplitudes of the mth reflected and transmitted waves. The wavenumbers k_{xm} and k_{zm} are

$$k_{xm} = k_0\left[n_{\mathrm{I}}\sin\theta - m(\lambda_0/\Lambda)\right], \tag{2.25}$$

$$k_{zp} = \left(k_0^2 n^2 - k_{xp}^2\right)^{1/2}. \tag{2.26}$$

The main purpose is to calculate T_m and R_m, from which diffraction efficiencies are determined. For this purpose, the coupled wave equations for

each slab should be constructed and solved for electromagnetic fields. After that, the boundary conditions are applied at every interfaces between two different regions in order to obtain the system of equations for T_m and R_m. Let us first derive the coupled wave equation governing each grating layer. For lth slab, the electric field component $E_{l,x}$ and the magnetic field component $H_{l,x}$ should satisfy the Maxwell equations, which gives

$$\partial H_{l,y} / \partial z = -j\omega\varepsilon_0\varepsilon_l(x)E_{l,x}, \tag{2.27}$$

$$\partial E_{l,y} / \partial z = -j\omega\mu_0 H_{l,x} + (\partial E_{l,z} / \partial x), \tag{2.28}$$

where ε_0, μ_0, ε_l, and ω denote the permittivity and the permeability of free space, the relative permittivity of grating and the angular frequency of incident light, respectively. Owing to the periodic nature of each slab, ε_l is a periodic function in x-y plane. According to the Floquet theorem, $E_{l,x}$ and $H_{l,x}$ becomes the linear combination of space harmonic functions.

$$\varepsilon_l(x) = \sum_p \varepsilon_{l,p} e^{j2\pi p/\Lambda}, \tag{2.29}$$

$$H_{l,y} = \sum_m U_{l,m}(z) e^{-jk_{xm}x}, \tag{2.30}$$

$$E_{l,x} = j(\mu_0 / \varepsilon_0)^{1/2} \sum_m S_{l,m}(z) e^{-jk_{xm}x}. \tag{2.31}$$

Here, $U_{l,i}$ and $S_{l,i}$ are the normalized amplitudes of the ith space harmonic fields. By the substitution of Eqs. (2.25), (2.26), and (2.27) into Eq. (2.23), we obtain

$$\left[\partial^2 \mathbf{U}_{l,\mathbf{y}} / \partial(\mathbf{z}')^2\right] = \left[\mathbf{E}_l\right]\left[\mathbf{B}_l\right]\left[\mathbf{U}_{l,\mathbf{y}}\right], \tag{1.32}$$

where

$$\mathbf{B}_l = \mathbf{K}_\mathbf{X}\mathbf{E}_L^{-1}\mathbf{K}_\mathbf{X} - \mathbf{I}.$$

Also, **z**' is $k_0 z$. **I**, $\mathbf{K_x}$, and $\mathbf{E}_l$ are the unity matrix, the diagonal matrix with $k_{x,i}/k_0$, and the matrix with $\varepsilon_{m,n}$ for its m, nth element. Therefore, the problem of solving the Maxwell equations in each slab becomes that of calculating the eigenvalues and the eigenvectors with the matrix of $\mathbf{E}_l\mathbf{B}_l$. By solving Eq. (2.32), we obtain the matrix of eigenvectors $\boldsymbol{W}_l$ and $\boldsymbol{Q}_l$, the latter of which is a diagonal matrix with the eigenvalues of $\mathbf{E}_l\mathbf{B}_l$.

As in the case of multilayered films, we calculate T_m and R_m by applying the boundary conditions at the interfaces between two different regions. The boundary conditions at $z = 0$ gives

$$\begin{bmatrix} \delta_{m0} \\ j\delta_{m0}\cos\theta / n_{\mathrm{I}} \end{bmatrix} + \begin{bmatrix} \mathbf{I} \\ -j\mathbf{Z}_{\mathrm{I}} \end{bmatrix} \mathbf{R} = \begin{bmatrix} \mathbf{W}_1 & \mathbf{W}_1\mathbf{X}_1 \\ \mathbf{V}_1 & -\mathbf{V}_1\mathbf{X}_1 \end{bmatrix} \begin{bmatrix} \mathbf{c}_1^+ \\ \mathbf{c}_1^- \end{bmatrix}, \tag{2.33}$$

at the boundary between l-1 and l slabs

$$\begin{bmatrix} \mathbf{W}_{l-1}\mathbf{X}_{l-1} & \mathbf{W}_{l-1} \\ \mathbf{V}_{l-1}\mathbf{X}_{l-1} & -\mathbf{V}_{1-1} \end{bmatrix} \begin{bmatrix} \mathbf{c}_{l-1}^+ \\ \mathbf{c}_{l-1}^- \end{bmatrix} = \begin{bmatrix} \mathbf{W}_l & \mathbf{W}_l\mathbf{X}_l \\ \mathbf{V}_l & -\mathbf{V}_l\mathbf{X}_l \end{bmatrix} \begin{bmatrix} \mathbf{c}_l^+ \\ \mathbf{c}_l^- \end{bmatrix}, \tag{2.34}$$

at $z = D_L$

$$\begin{bmatrix} \mathbf{W}_L & \mathbf{W}_L\mathbf{X}_L \\ \mathbf{V}_L & -\mathbf{V}_L\mathbf{X}_L \end{bmatrix} \begin{bmatrix} \mathbf{c}_L^+ \\ \mathbf{c}_L^- \end{bmatrix} = \begin{bmatrix} \mathbf{I} \\ j\mathbf{Z}_{\mathrm{T}} \end{bmatrix} \mathbf{T}, \tag{2.35}$$

where **V** is $\mathbf{E}_l^{-1}\mathbf{W}_l\mathbf{Q}_l$, $\mathbf{Z}_{\mathrm{I}}$ and $\mathbf{Z}_{\mathrm{T}}$ are diagonal matrices with $k_{\mathrm{I},zm}/(n_{\mathrm{I}}^2 k_0)$ and $k_{\mathrm{T},zm}/(n_{\mathrm{T}}^2 k_0)$ (m = 0, 1, 2,…). Also, $\mathbf{X}_l$ is a diagonal matrix with $\exp(-q_{l,v}d_l)$. Following the same procedures for Eq. (2.22), we then obtain

$$\begin{bmatrix} \delta_{m0} \\ j\delta_{m0}\cos\theta / n_{\mathrm{I}} \end{bmatrix} + \begin{bmatrix} \mathbf{I} \\ -j\mathbf{Z}_{\mathrm{I}} \end{bmatrix} \mathbf{R}$$

$$= \prod_{l=1}^{L} \begin{bmatrix} \mathbf{W}_l & \mathbf{W}_l\mathbf{X}_l \\ \mathbf{V}_l & -\mathbf{V}_l\mathbf{X}_l \end{bmatrix} \begin{bmatrix} \mathbf{W}_l\mathbf{X}_l & \mathbf{W}_l \\ \mathbf{V}_l\mathbf{X}_l & -\mathbf{V}_l \end{bmatrix}^{-1} \begin{bmatrix} \mathbf{I} \\ -j\mathbf{Z}_{\mathrm{T}} \end{bmatrix} \mathbf{T}. \tag{2.36}$$

By solving Eq. (2.36), T_m and R_m can be obtained. From them, the transmitted and reflected diffraction efficiencies for the mth order of resonance are determined by using following equations.

$$DE_{rm} = R_m R_m^* \,\mathrm{Re}\left[k_{\mathrm{I},zm} / k_0 n_{\mathrm{I}} \cos\theta\right], \tag{2.37}$$

$$DE_{tm} = T_m T_m^* \frac{\mathrm{Re}\left[k_{\mathrm{T},zm} / n_{\mathrm{T}}^2\right]}{k_0 \cos\theta / n_{\mathrm{I}}}. \tag{2.38}$$

Note that the extension of above method into the cases of TE incidence or conical mount is straightforward and found in Ref. [72]. The numerical calculation can be performed with arbitrary precision by adjusting the number of slabs and the order of truncations in Fourier transform. In this thesis where simple multilayered structures are mostly considered, the small order of truncations about 200 gives the convergence of solution.

Chapter 3. Monolithic Integration of Color Elements

3.1. Introduction

Despite several advantages, the practical implementation of structural color elements based on OMRs are largely impeded by the lack of suitable fabrication technique for the integration of different color elements in a versatile manner. Owing to the dependence on the thickness of RC, the integration of different color elements involves the patterning of OMRs in a multilevel architecture. In an effort to address this issue, there have been several approaches based on a series of vacuum deposition of dielectric layers [29, 30] and focused ion beam milling [58]. However, these approaches require expensive facilities and long process time, significantly limiting throughput and large-area application. Therefore, of central importance is the development of simple and low-cost color patterning technique applicable over large area in a massively parallel manner.

In this chapter, we present the monolithic integration of different color elements by a series of transfer-printing of dielectric patterns for RC. By using this method, two types of combinatorial color arrays integrating three building blocks of the etalon-type OMRs for R, G, and B are fabricated in monolithic architecture. The RCs between two TRLs were formed with a soluble fluorinated polymer by transfer-printing in a pattern-by-pattern or a pattern-on-pattern manner on a single substrate. The TRLs were made of silver by vacuum

deposition. The color palette was primarily dependent on the thickness and the refractive index of the fluorinated polymer. The reflectance of the TRL was over 75% in the wavelength range of visible light and the thickness of the polymer was varied from 56 to 173 nm. The self-defined lateral gap on the underlying background layer served as a light-blocking region which was capable of separating adjacent color units from each other. A prototype LCD incorporated with our combinatorial color array in the vertical configuration showed that the color filtration of the white backlight into R, G, and B by the corresponding micro-resonators was well achieved.

3.2. Elemental design and monolithic architecture

Figure 3.1(a) shows a schematic diagram illustrating the elemental micro-resonator for an etalon-type OMR filter. The OMR is composed of TRL 1, TRL 2, and RC between the two layers. The refractive index and the thickness of the RC are denoted by n and d, respectively. From Eq. (2.5), it is evident that the transmission peak is shifted to a longer wavelength with increasing the effective optical path (nd) in the RC, implying that for given RC medium, the wavelength of resonance or the color of the transmitted light through the OMR filter can be easily tailored by simply varying the RC thickness.

In Fig. 3.1(b), a monolithic architecture of three OMRs with different RC thicknesses, corresponding to three primary colors (R, G, and B), is illustrated. This architecture consists of two TRLs (TRL 1 and TRL 2) and two RCs (RC 1 and RC 2) whose refractive indices are n_1 and n_2, respectively. The entire substrate is covered with RC 1 having the thickness of d_1 for the purpose of

self-defining the lateral gap between adjacent OMRs during transfer-printing of RC 2 in sequence. Depending on the thickness (d_2) of RC 2 in addition to the thickness (d_1) of RC 1, different OMRs produce different colors, for example, R, G, and B. Note that the lateral gap provides a light-blocking element similar to a black matrix (BM) pattern in the CF for the LCD provided that no light is transmitted through only-RC 1 region.

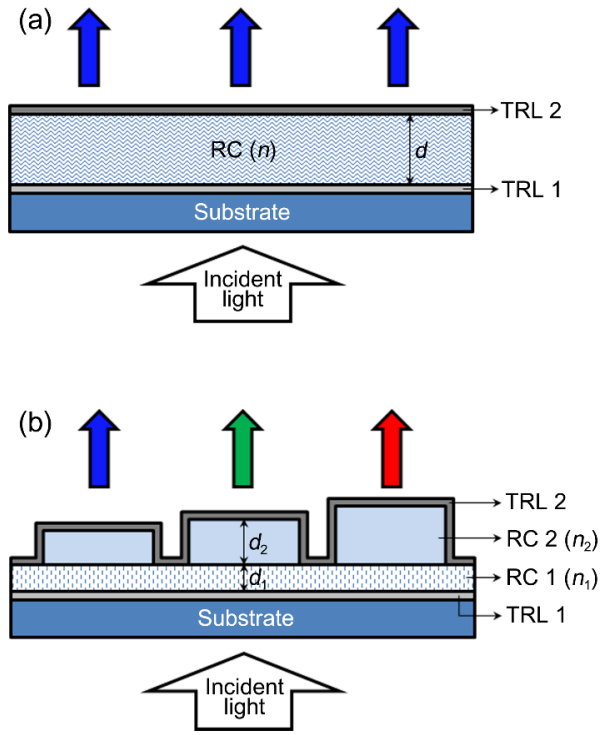

Figure 3.1: Schematic illustration of OMR-based color elements. (a) Cross sectional view of an elemental OMR for color selection (for example, blue). (b) Schematic illustration of monolithic architecture of three different OMRs for different colors (for example, R, G, and B) together with a self-defined lateral gap between adjacent micro-resonators. Here, d, d_1, and d_2 denote the thickness of RC, that of RC 1, and that of RC 2, respectively, between two TRLs. The refractive indices are n, n_1, and n_2 for the RC, RC 1, and RC 2, respectively.

3.3. Color selection in elemental micro-resonators

We first numerically investigate the color selection properties of elemental OMRs with different values of the thickness for the RC. Figure 3.2 shows the numerical results calculated by RCWA method for optical transmittances as a function of *d* from 0 to 200 nm. Here, *n* was 1.4 and the thickness of TRL was 25 nm. The optical constants for silver was taken from Ref. [73]. For concerned range for *d*, only a single resonant peak exists at visible wavelength, which is consistent with the expected from Eq. (2.10). For R, G, and B color elements, we select *d* to be 105, 130, and 170 nm, respectively.

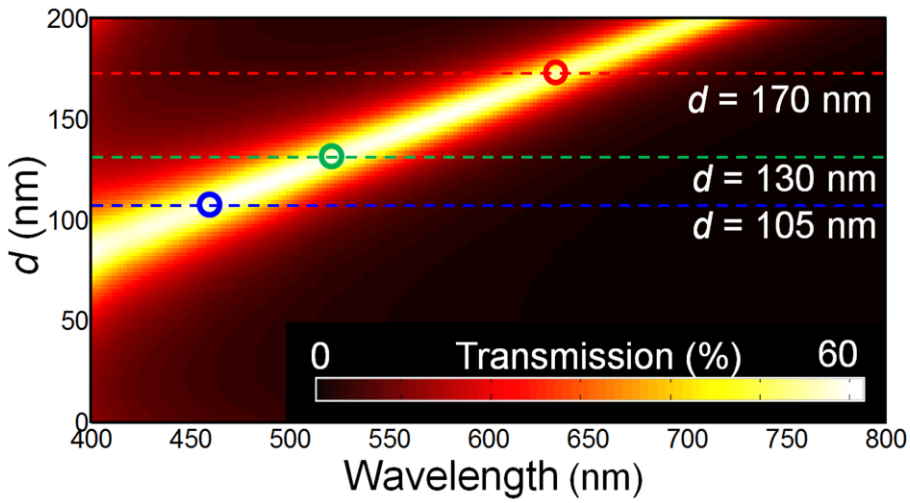

Figure 3.2: Simulation results for thickness-dependent optical transmittances of OMR element. The dashed lines represent the optical transmittances for different thicknesses of *d* = 170 nm, 130 nm, and 105 nm for R, G, and B filtering.

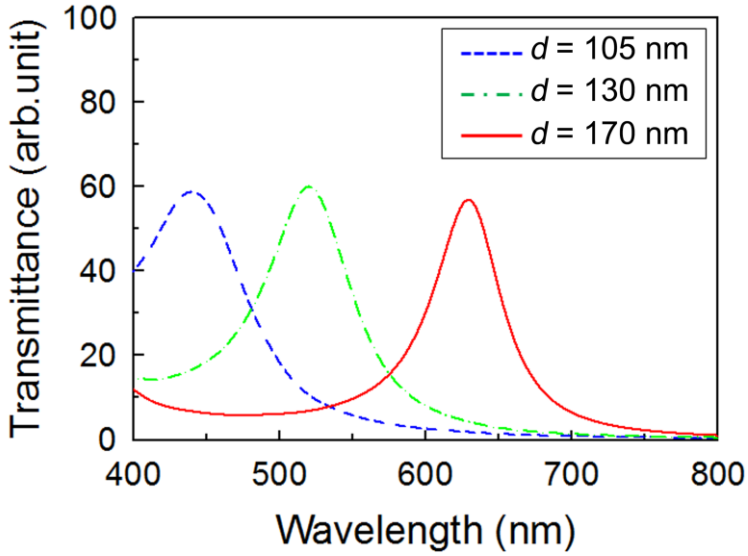

Figure 3.3: Simulation results for optical transmittances for *d* = 105, 130, and 170 nm.

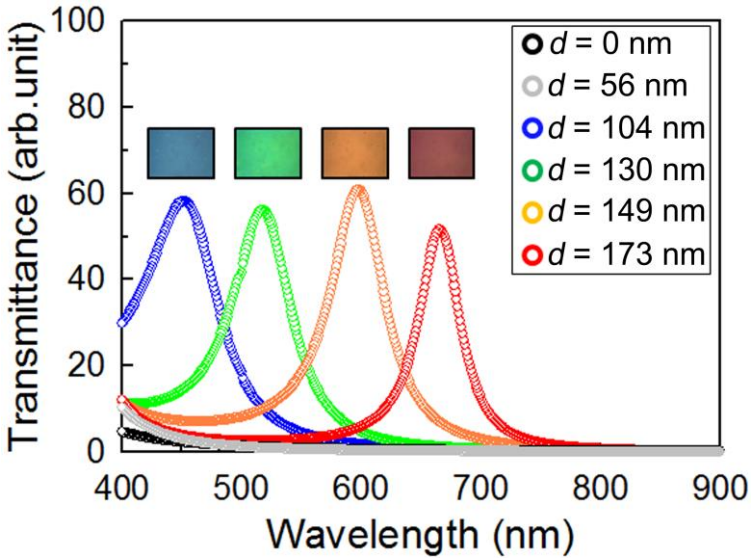

Figure 3.4: Experimental results for optical transmittances of OMRs for different *d*s. The insets show corresponding microscopic images.

Figure 3.3 shows the numerical results for optical transmittances of OMRs having *d* of 105, 130, and 170 nm. The well-defined resonant peaks are located at the wavelengths of 446, 528, and 630 nm, which correspond to B, G, and R, respectively. The transmittances at peak wavelengths are about 60%, being relatively high compared to other types of color filters based on PCs and plasmonic nanostructures [15, 16] and comparable to conventional pigment-based filters [24].

Based on the numerical design, color elements were fabricated for varying *d*. TRL 1 and TRL 2 were 25 nm-thick silver (Ag) layers produced by thermal evaporation at the rate of 2 Å/s under about 10^{-6} Torr. The reflectance of TRL 1 (or TRL 2) was over 75% in visible regime. For the RC, a fluorinated polymer (EGC-1700; 3M) having the refractive index of 1.38 was dip-coated on TRL 1. The concentration of the fluorinated polymer was 2 wt.% in a fluorinated solvent (HFE-7100; 3M).

The RC thickness (d = 0 ~ 173 nm) was varied with adjusting the dip-coating speed. For example, the dip-coating speeds of 100 mm/min and 250 mm/min yielded the RC thickness of about 56 nm and 104 nm (within 5 nm error) on TRL 1, respectively. The transmission spectra through the elemental OMRs were measured using a commercial spectrometer (V530; Jasco). For the measurement of the transmittance in unit of % relative to the input light source which was a broadband halogen lamp (λ = 340 ~ 1100 nm), the transmitted intensity through each color element was measured using a silicon photodiode on sweeping the wavelength from 400 nm to 900 nm in an interval of 0.5 nm.

Figure 3.4 shows the experimental results for optical transmittances of six color elements having different values of 0 nm, 56 nm, 104 nm, 130 nm, 149 nm, and 173 nm for *d*. For very thin RCs (*d* = 0 and *d* = 56 nm), no appreciable transmission was observed at visible wavelengths except for the near-ultraviolet region. The transmittance at around 400 nm was less than 10%. For relatively thick RCs of 104 nm, 130 nm, 149 nm, and 173 nm, the resonant wavelengths were obtained at 452 nm, 518 nm, 598 nm, and 666 nm, corresponding to B, G, orange, and R colors, respectively. The maximum values of the transmittance were about 60%. The optical transmittances for *d* = 104 nm, 130 nm, and 173 nm are in a good agreement with the numerical results for *d* = 105 nm, 130 nm, and 170 nm given in Fig. 3.3. The optical microscopic images of the color elements producing four different colors were shown in the insets of Fig. 3.4.

3.4. Monolithic integration for combinatorial color arrays

We now describe the monolithic integration of color elements for three primary colors (R, G, and B) into combinatorial color arrays. Figure 3.5 illustrates the sequential steps of integrating the primary color elements onto a single substrate by transfer-printing of the corresponding RCs. Both TRL 1 and TRL 2 were the same as those for color element. Likewise, the underlying background layer, RC 1, was simply the RC in the elemental device. Note that the fluorinated polymer used is optically transparent (over 90% for transmittance in the visible range), chemically inert, and mechanically compatible with a transfer-printing process [74].

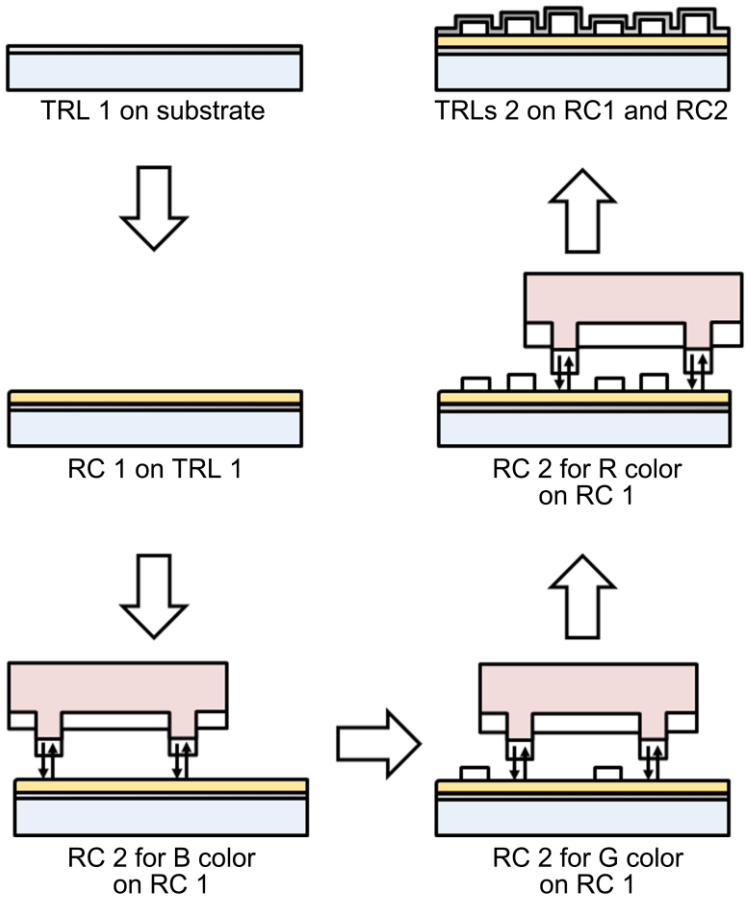

Figure 3.5: Monolithic integration of three primary color (R, G, and B) elements into a combinatorial color array. An identical stamp was used for transfer-printing different color patterns in sequence. The black upward- and downward-arrows represent the transfer-printing process.

The dip-coating speed for RC 1 on TRL 1 was chosen to be about 100 mm/min to produce the thickness d_1 = 56 nm for which no transmission in the visible wavelength range was obtained as shown in Fig. 3.4. This is critical for

self-defining the lateral gap between adjacent color elements during transfer-printing in sequence. A transfer-printing stamp was made of poly-dimethylsiloxane (PDMS) (Sylgard 184; Dow Corning) to ensure low adhesion at the interface between the stamp and the fluorinated polymer. For B color, RC 2 with the thickness d_2 = 51 nm was printed on the top of RC 1 by the transfer of the fluorinated polymer pattern prepared on the PDMS stamp at the dip-coating speed of 100 mm/min. Note that the total thickness of 107 nm, combining RC 1 and RC 2, corresponds to B color as expected from Fig. 3.4. For G color, RC 2 with the thickness d_2 = 79 nm was produced on RC 1 in a side-by-side manner using the fluorinated polymer prepared at 175 mm/min.

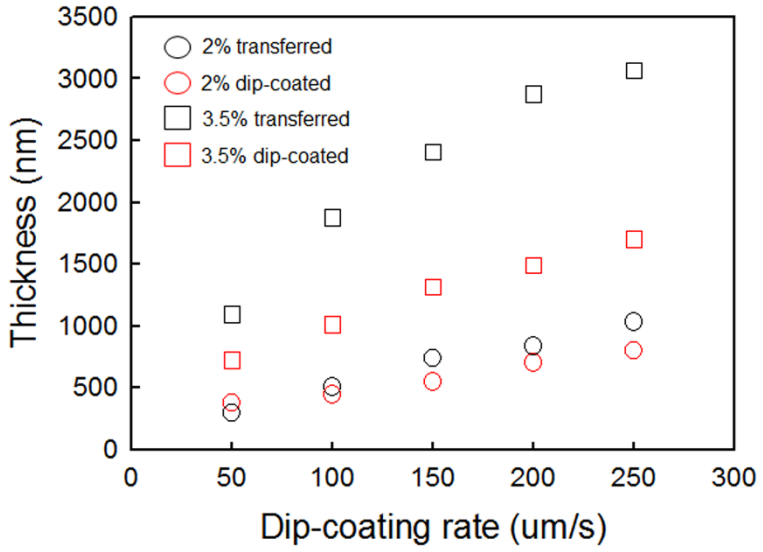

Figure 3.6: Effect of dip-coating speed and concentration on the thickness of EGC layer formed by two different methods of transfer-printing and dip-coating.

Similarly, for R color, RC 2 with the thickness d_2 = 103 nm was produced on RC 1 using the fluorinated polymer prepared at 250 mm/min. In general, different materials for RC 1 and RC 2 can be used as long as they are optically transparent, compatible with each other, and capable of easily defining desired patterns with thickness variations.

Here, it should be mentioned that the thicknesses of EGC layers formed by two different methods of transfer-printing and dip-coating can be different as shown in Fig. 3.6. For the dilute solution with 2 wt.% concentration, no appreciable difference in thickness was observed. For higher concentration of 3.5 wt.%, on the other hand, the thickness for the transfer-printing case was significantly larger than that for the dip-coating case. It is largely due to the presence of surface structure on transfer-printing mold and slow drying speed in the high concentration case.

3.5. Combinatorial color arrays

As the first type of combinatorial color arrays, Fig. 3.7(a) shows a schematic diagram of a unit cell composed of R, G, and B color elements in rectangular shape. The three color elements were arranged in a pattern-by-pattern fashion and separated from neighboring elements by the self-defined gap on the underlying background layer of RC 1. Figure 3.7(b) shows the microscopic image of a lateral color array which represents Fig. 3.7(a). The width (W_r) and the length of each color element were about 100 μm and 300 μm, respectively. The gap or separation (W_b) between adjacent color elements was about 10 μm.

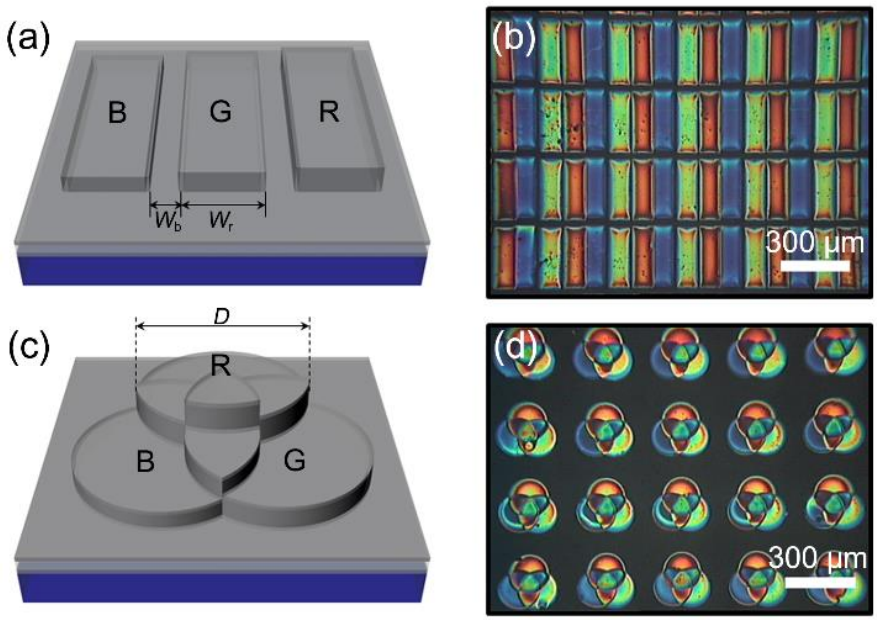

Figure 3.7: Schematic illustration of combinatorial color arrays in (a) a pattern-by-pattern configuration and (c) a pattern-on-pattern configuration. (b) and (d) show the microscopic images of the fabricated color arrays corresponding to (a) and (c). Here, W_r, W_b, and D denote the width of the rectangular color element, the separation between adjacent color elements, and the diameter of the circular color element, respectively.

It should be emphasized that the thickness (d_1 = 56 nm) of RC 1 for the background layer allows to spontaneously form light-blocking patterns as clearly seen in Fig. 3.7(b).

The second type is schematically illustrated in Fig. 3.7(c) where a unit cell composed of R, G, and B color elements in circular shape are partially overlapped with each other in a pattern-on-pattern fashion. In this case, the

overlapped regions exhibit different colors from surrounding regions. The microscopic image of such multi-level color array, corresponding to Fig. 3.7(c), was shown in Fig. 3.7(d). The diameter (D) of each color element was about 100 μm. Again, the background of only RC 1 serves as a light-blocking layer. Depending on the total thickness of the overlapped region, the resonance conditions for the higher-orders of resonance can be met [59]. For example, the region overlapped by G and R color elements exhibited bluish color and the central region overlapped by three color elements became greenish due to the resonance of the second-order (m = 2). The non-uniformity appeared near the boundaries between different colors are attributed to the errors involved in transfer-printing and can be improved by adopting a more sophisticated technique for transfer-printing [75].

3.6. Application to liquid crystal displays

Let us investigate the functionality of our color array for the CF in an LCD. The basic principle of such CF in the vertically aligned LC cell is schematically illustrated in Figs. 3.8(a) and 3.8(b). Here, the LC cell is composed of a bottom glass substrate having patterned transparent electrodes, a vertical alignment (VA) layer on the bottom substrate, a vertically aligned LC having negative dielectric anisotropy, the VA layer on the top substrate, and the top glass substrate with three OMRs for R, G, and B colors. The unit pixels in the LC cell are defined by the patterns of the transparent electrode on the bottom substrate.

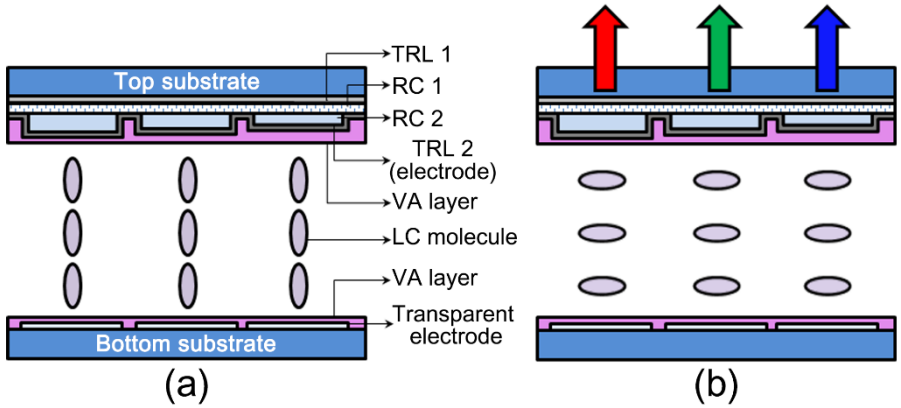

Figure 3.8: Schematic diagram of the LC cell incorporated with a lateral color array as the CF in the vertical configuration (a) under no applied voltage and (b) under the applied voltage above a threshold.

In our LC cell, TRL 2 made of metal can be used as a top electrode and thus no additional electrode is required for the application of the operation voltage. The LC cell is placed between crossed polarizers such that the rubbing direction makes an angle of 45˚ with respect to the optic axis of one of the two polarizers. Under no applied voltage, the polarization state of light from the backlight unit through the first (bottom) polarizer remains unchanged on passing through the LC layer. The light is then completely blocked by the second (top) polarizer as shown in Fig. 3.8(a). In the presence of the applied voltage above a threshold in three unit pixels of R, G, and B colors, the LC molecules are reoriented horizontally along the rubbing direction. As a result, the change in the polarization state of light occurs on passing through the LC layer and the light is transmitted through the second polarizer as shown in Fig. 3.8(b).

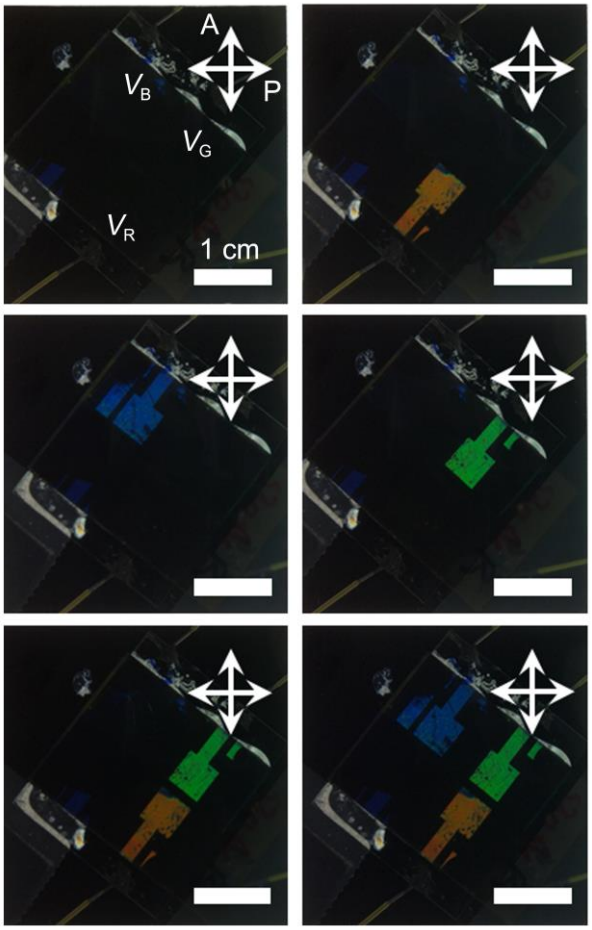

Figure 3.9: Microphotographs showing the LC cell between crossed polarizers under different combinations of voltages for R, G, and B color elements. The alignment direction of LC makes an angle of 45° with the optic axis of one of polarizer. V_R, V_G, and V_B denote voltages applied for R, G, and B color elements, respectively. The turn-on voltage was 5 V in all cases.

Finally, a simple prototype LCD, incorporated with the lateral color array as the CF for three primary colors of R, G, and B in the vertical configuration, was fabricated for the purpose of proving the above concept. Here, the patterned indium-tin-oxide (ITO) on a glass substrate was used as the bottom electrode. Both the VA layers on the top and the bottom substrate were spin-coated with polyimide and rubbed along antiparallel directions. A nematic LC (MLC-2038; Merck) was used for the vertically aligned LC layer. The cell gap between the two substrates was maintained using glass spacers of 6 μm thick. In facilitating the fabrication, the lateral color array (of a macroscopic scale of millimeters) was prepared on the top substrate through transfer-printing. Note that the scalability to smaller dimensions primarily depends on the pattern size (or resolution) of the stamp for transfer-printing. Figure 3.9 shows the microphotograph of our LC cell under different combinations of applied voltages for R, G, and B color elements. While the dark state was obtained under no applied voltage, different colors of R, G, and B from pixel to pixel were clearly observed under the applied voltage of 5 V. The unit pixels of R, G, and B colors can be independently operated by the application of different voltages to the patterned ITO electrodes. Note that our lateral color array indeed provides the color filtration capability for the LCD as an alternative to a conventional pigment-based CF.

3.7. Summary

In summary, we demonstrated two types of combinatorial color arrays where color elements based on OMRs for three primary colors of R, G, and B

were monolithically integrated. For the optical RCs, a soluble fluorinated polymer having the refractive index of 1.38 was transfer-printed between two TRLs in a pattern-by-pattern or a pattern-on-pattern manner on a single substrate. In our case, the thickness of the RC for R, that for G, and that for B were 107 nm, 135 nm, and 159 nm, respectively. The relative transmission to the input light source at the peak wavelength was about 60%. A self-defined optical resonator, formed by the background layer (RC 1) of 56 nm thick between TRL 1 and TRL 2, was found to effectively block the light in the visible range so that it provides naturally a light-blocking element to separate adjacent color elements from each other. Our approach to the construction of combinatorial color arrays in monolithic architecture presented here will serve as a versatile platform to build up a new class of color elements for a variety of visual applications such as the LCDs, white organic light-emitting diodes, and complex color palettes.

Chapter 4. Realization of Full Color Palette by Embedded Plasmonic Nanostructures

4.1. Introduction

In previous chapter, the color integration technique by multiple transfer printing of dielectric patterns was described. Despite of its strong advantages, the unevenness of multilevel architecture can result in serious problem including inhomogeneity of electrical performance when the final device is incorporated into electro-optic device such as LCDs. In addition, this approach suffers from inherent angle-dependency owing to its linear dependence on the thickness of RC. Note that the adoption of highly absorbing materials such as amorphous silicon for RC reduces the thickness variation required for different color elements to a few nanometers and accordingly improves the angle dependency by the help of the non-trivial value of the phase retardation on reflection at internal interfaces [61-63]. However, this approach still requires a series of vacuum depositions for the integration process and suffers from the significant increase of optical absorption.

One possible approach to tailor the color palette of etalon-type OMRs within the given thickness for RC is the introduction of the nanoscale phase-shifting element which modulates the phase of incoming electromagnetic wave depending on their geometry. In the field of metasurfaces, for example, metallic or dielectric nanostructures have been used as phase-shifting elements to engineer the wave front of light in a planar configuration [76-78]. However, the

phase-modulation property of nanostructures has been rarely exploited into OMRs except for a few cases where the nanostructures such as gold nanoparticles [79] and graphene nanosheets [80] are used to tune the cavity mode in the near- and infrared regime. Even in these cases, the magnitude of tuning is significantly limited by the small scattering efficiency of nanostructures. Since the interior architecture plays a critical role on the interaction of light with coupled structures [81, 82], the effect of the geometrical parameters of phase-shifting elements on the cavity mode should be investigated further in order to expand above concept toward the acquisition of a full-color palette in an OMR simultaneously improving the angle dependency.

In this chapter, the effect of silver nanostructures on the cavity mode was investigated to tailor the color palette of an OMR without changing the thickness of RC for different color elements. Two types of silver nanostructures having continuous (nanofilm) and discontinuous (nanoislands) features were incorporated as phase shifting elements into the middle of RC. Depending on the geometry of nanostructures, the resonant wavelengths can be tailored within the entire range of visible wavelengths for given thickness for RC. In the case of nanoislands, in particular, the angle-dependency was reduced owing to the decrease of RC thickness compared to reference case. The general features of the effect of the nanostructures on the cavity mode agreed well with the numerical results. Based on the effect of silver nanostructures, we demonstrated an angle-independent full-color element on a flexible substrate for the given thickness of RC.

4.2. Basic concept

Let us first describe the geometrical structure of OMR having nanoscale phase-shifting elements inside RC as schematically illustrated in Fig. 4.1. In our case, two elementary types of metallic nanostructures are considered as phase-shifting elements: a nanofilm and nanoislands. Here, the etalon-type OMR consists of two TRLs and RC between them. The thicknesses of all the TRLs are identical to be t_T and that of RC is d, respectively. The geometrical structure of the nanofilm is characterized only by the thickness (t_1) while that of nanoislands is by three geometrical parameters of the periodicity (p), the width (w), and the thickness (t_2). Phase-shifting elements are placed at the middle of RC, which is represented by the dashed line. Except for TRLs, the dielectric materials having low extinction coefficients are used for the other parts to minimize optical loss. Thus, the refractive indices of the RC and the substrate are assumed to have only real parts of n and n_s, respectively.

We now explain the basic concept of tuning the color palette of an OMR by the introduction of a nanoscale phase-shifting element. From the viewpoint of ray optics where the Fabry-Perot resonance is considered as the constructive interference between direct (passing through the resonator without reflections) and indirect beam (two times reflections on TRLs before passing through the resonator), the indirect one passes through the phase-shifting element two times more than the direct one. Analytically, this effect of phase retardation by a phase-shifting element is represented as an additional term in the resonance condition as follows.

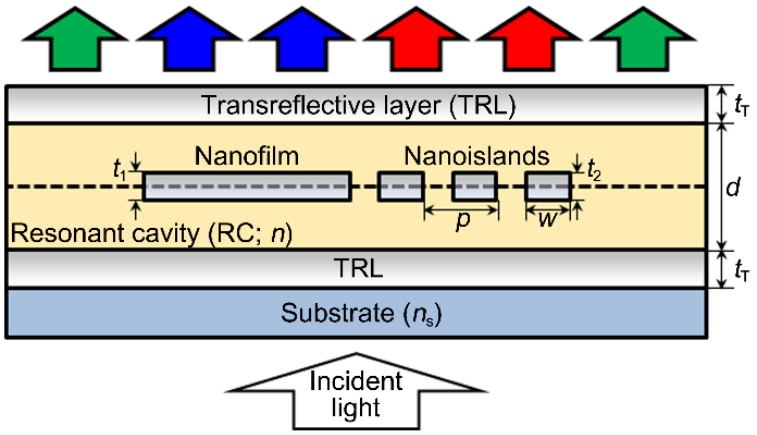

Figure 4.1: Geometrical configuration of the OMR having a nanofilm and nanoislands inside a RC. Here, the thicknesses of RC and two TRLs are d and t_T, respectively. The nanofilm and nanoislands are placed at the middle plane of RC denoted by the black dashed line. The nanofilm is characterized by its thickness, t_1 while the nanoislands are their thickness t_2, width w, and periodicity p. Also, n and n_s denote the refractive indices of RC and a substrate, respectively.

$$nd\cos\theta = \frac{\lambda_R}{2}\left[m - \sum_{i,j}\frac{\Delta\phi_{r,i} + \Delta\phi_{t,j}}{2\pi}\right]. \tag{4.1}$$

Here, λ_R, θ, and m represents the resonant wavelength, the incident angle and the order of resonance, respectively. Compared to the original case where only the phase retardation on the reflection at TRLs, $\Delta\phi_{r,i}$ (i = 1, 2), are considered, those by a phase-shifting element, $\Delta\phi_{t,j}$ (j = 1, 2), are additionally included. Therefore, it is expected that, for the positive value of $\Delta\phi_{t,j}$, λ_R red-shifts

whereas, for the negative value of $\Delta\phi_{t,j}$, λ_R blue-shifts from the reference case where no phase-shifting element is present inside RC. For both cases, in addition, the magnitude of the shift will be determined by the absolute value of $\Delta\phi_{t,i}$.

4.3. Phase modulation property of freestanding nanostructures

To understand the effect of embedding phase-shifting elements into an OMR, the phase modulation property of such elements should be first investigated. Figure 4.2 shows the geometry for numerical simulation where the transverse magnetic (TM)-polarized plane wave having wavenumber k is incident on either freestanding nanofilm or nanoislands in vacuum. We used silver for phase-shifting elements due to its low optical loss and strong interaction with light at visible wavelengths. Here, the refractive index of the vacuum was 1.00. Following the convention used in the equation for the Fabry-Perot resonance condition [79], the phase retardation in the unit of radian, $\Delta\phi$, is positive when the plane wave passing through the phase-shifting element lags behind the one propagating the same distance in vacuum.

To illustrate general features, the simulated phase retardations together with transmittances as a function of wavelength for typical nanofilm (t_1 = 8 nm) and nanoislands (t_2 = 8 nm, w = 30 nm, and p = 60 nm) are given as examples in Fig. 4.3. Here, $\Delta\phi$ is converted into the unit of degree.

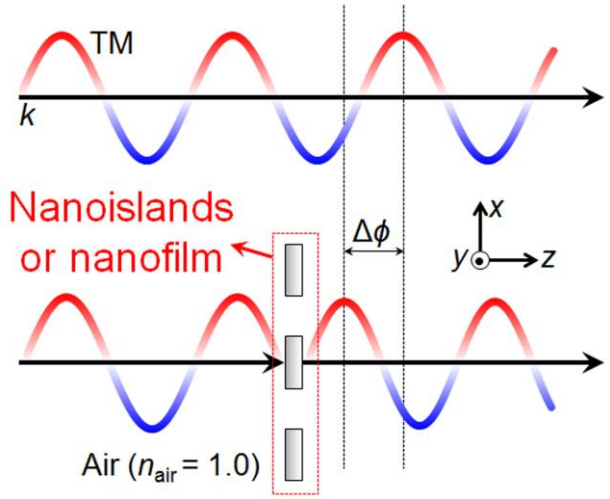

Figure 4.2: Geometry for the numerical simulation of phase retardation on transmission through freestanding nanofilm and nanoislands.

From the transmittance for the nanofilm in Fig. 4.3(a), it is clear that no optical resonance is present at visible wavelengths. Accordingly, $\Delta\phi$ shows no abrupt change but linearly increases toward negative direction with increasing wavelength. Note that the sign and the magnitude of $\Delta\phi$ is covariant with the real part of the dielectric constant of silver when the refractive indices of both sides with respect to a nanofilm are matched [83]. Thus, near the wavelength of 324 nm where the real part becomes positive [84], the sign of $\Delta\phi$ also changes to be positive. In the case of nanoislands in Fig. 4.3(b), the localized surface plasmon resonance (LSPR) occurs at 430 nm, leading to the abrupt change of $\Delta\phi$ in the vicinity of the resonant wavelength.

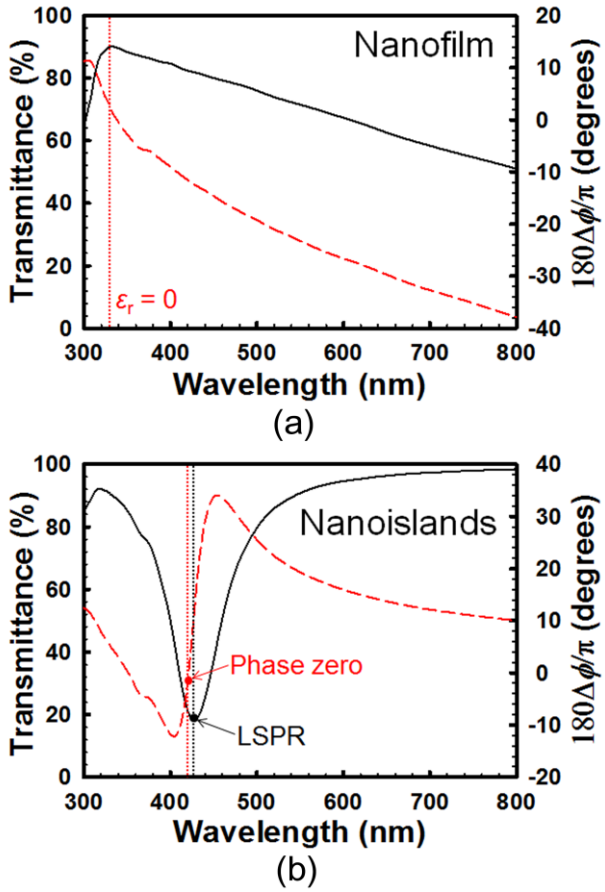

Figure 4.3: Typical transmittances and phase retardations by (a) nanofilm (t_1 = 8 nm) and (b) nanoislands (t_2 = 8 nm, w = 30 nm, and p = 60 nm). In (a), short dashed lines denote the wavelength where the real part of dielectric constant of silver becomes zero (ε_r =0). In (b), LSPR point represents the wavelength for localized surface plasmon resonance.

Since resonant wavelength is always close to the zero of $\Delta\phi$ [85], the sign of $\Delta\phi$ for nanoislands changes near LSPR from negative for the wavelengths under LSPR, to positive for the other side. It indicates that the location of LSPR is important in predicting that of cavity mode when nanoislands are incorporated into an OMR.

From now on, we describe the effect of geometrical parameters on the phase modulation property of a nanofilm and nanoislands. Above all, the periodicity of nanoislands should be first considered since it determines the coupling efficiency between the scattered fields by an individual nanoisland. For different p of 20, 30, 60, and 200 nm, $\Delta\phi$s as a function of wavelength are numerically simulated where t_2 and w are 8 nm and 18 nm, respectively. In Fig. 4.4(a), as p increases, $\Delta\phi$ becomes small, which comes from the decrease in the surface coverage of nanoislands as well as resultant weak coupling between scattered fields. Another notable feature is the blue-shift of the zero of $\Delta\phi$ with increasing p. This is because, for TM polarization, the longitudinal electrical dipoles formed in the individual nanoislands at LSPR interact in a bonding mode so that the excitation wavelength required for resonance becomes small with decreasing p [86, 87]. Although small p is desirable in terms of phase modulating property, p should be at least more than 30 nm to avoid the opposite sign of $\Delta\phi$ in the regime of visible wavelengths since it might result in the splitting of the cavity mode as will be discussed later. Considering two criteria, p is fixed to be 60 nm when investigating the effect from the variation of the other geometrical parameters.

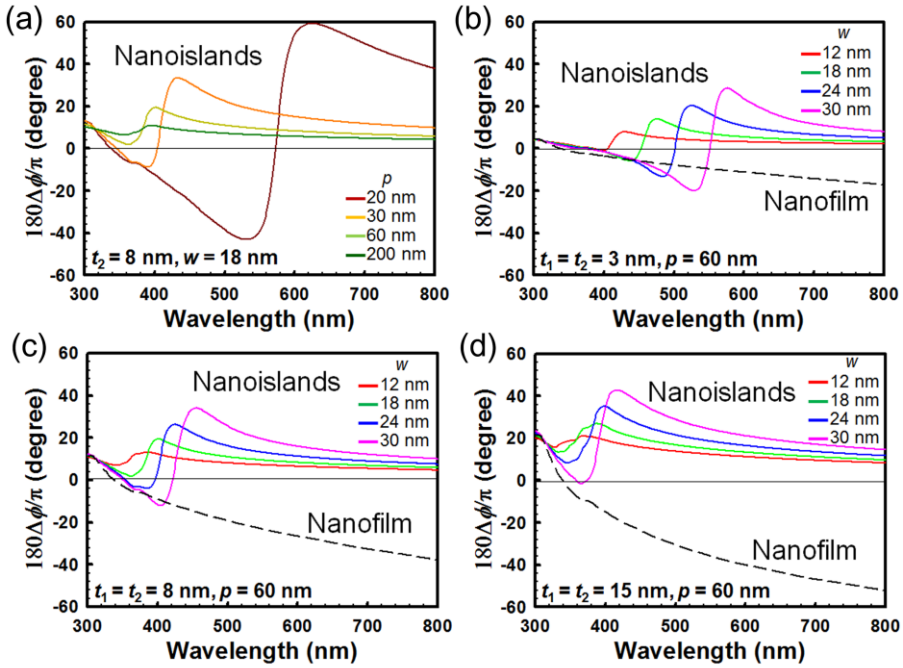

Figure 4.4: (a) The phase retardations by nanoislands (t_2 = 8 nm and w = 18 nm) as a function of wavelength for different p from 20 to 200 nm. The phase retardations by both nanofilm and nanoislands for different w (12, 18, 24, and 30 nm) as a function of wavelength in the case of (b) $t_1 = t_2$ = 3 nm, (c) $t_1 = t_2$ = 8 nm, and (d) $t_1 = t_2$ = 15 nm, respectively.

Figures 4.4(b)-(d) show the calculated $\Delta\phi$s as a function of wavelength by a nanofilm and nanoislands for $t_1 = t_2$ = 3 nm, 8 nm, and 15 nm, respectively. In the case of nanoislands, in addition, w varies from 12 nm to 30 nm at 6 nm interval for each t_1. As can be seen in the figure, the increase of t_1 leads to no significant change in the general behavior of $\Delta\phi$ in the nanofilm case although its magnitude becomes large at the given wavelength. Irrespective of t_1, the sign

of $\Delta\phi$ is mostly negative at the concerned wavelengths. In contrast, the sign of $\Delta\phi$ for nanoislands changes near LSPR wavelength at the middle of visible wavelengths. For given t_2, the LSPR wavelength governing the location of the zero of $\Delta\phi$ red-shifts with increasing w while, for given w, it blue-shifts with increasing t_2. Note that such behavior is consistent with the case of silver nanorods owing to the geometrical similarity [88-90]. As for the magnitude of $\Delta\phi$, it generally becomes large with increasing w and t_2, both of which results in the increase of the effective dipole moment of an individual nanoisland at the resonant wavelength, thus, scattering efficiency [89]. As t_2 increases, the phase retardation curves shift to the positive direction so that, for t_2 = 8 nm and 15 nm, it is almost always positive in whole spectrum regardless of t_2. Assuming that the nanofilm and nanoislands having the same thickness of more than 8 nm are embedded in a OMR, it is expected from Eq. (4.1) that cavity mode shifts to shorter wavelengths for the former case while it does to longer wavelengths for the latter case.

4.4. Effect of silver nanostructures on cavity mode and color palette

4.4.1. Effect of nanofilm on cavity mode

Let us now describe the effect of nanofilm on the cavity mode of an OMR based on the results for the freestanding case. From now on, n and n_s are set to be 1.6 and 1.5 in all cases, where the former is within the range of the refractive

indices of transparent polymers and the latter is that of a glass substrate. Figure 4.5 shows the zero-order transmittances of an OMR having a nanofilm as a phase shifting element for different t_1 from 0 nm to 15 nm. Here, d is 110 nm which corresponds to the resonance at λ_R = 550 nm when no nanofilm is involved, being indicated by the gray dotted line. The cavity mode represented by the dashed black line clearly shifts to shorter wavelengths with increasing t_1, being consistent with the prediction made earlier. Despite small decrease, the transmittance is as high as 46% at t_1 = 15 nm.

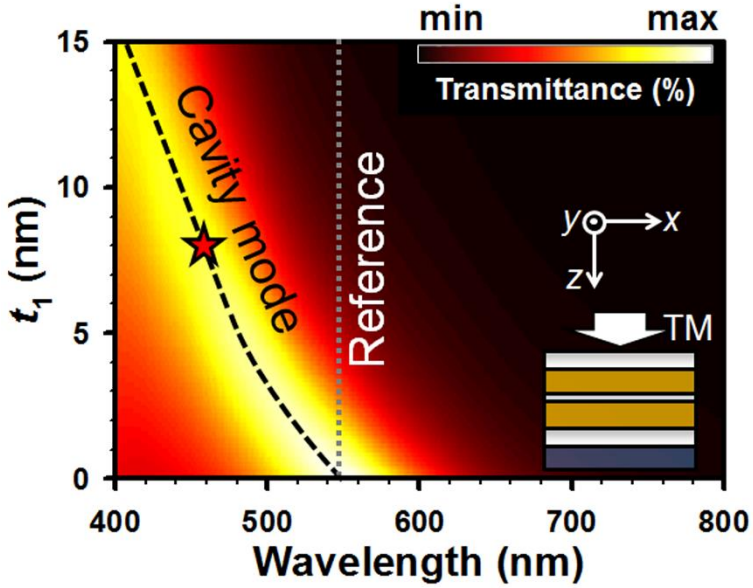

Figure 4.5: Zero order optical transmittances through the Fabry-Perot resonator with a nanofilm in RC under the incidence of the plane wave in a transverse magnetic (TM) polarization for varying t_1 from 0 to 15 nm. Here, the gray dotted and black long dashed line represent the resonant wavelength in the reference and nanofilm cases, respectively.

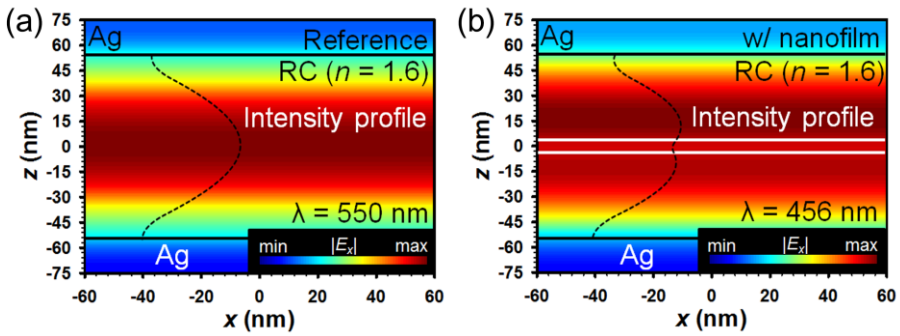

Figure 4.6: The electric field distribution for *x* component in RC (a) at λ_R = 550 nm (reference) and (b) at λ_R = 456 nm with 8 nm-thick nanofilm (corresponding to the red star in Fig. 4.5). In (a) and (b), the black short dashed lines denote the intensity profiles along the *z* direction.

To investigate the nature of the cavity mode, electric field distribution is calculated for t_1 = 8 nm. For comparison, the normalized *x*-component of electric fields are first calculated for the reference case at λ_R = 550 nm together with the intensity profile along *z* axis represented by the black dashed line in Fig. 4.6(a). As can be seen in the figure, the intensity is maximum at the middle of RC. It means that, for the effective coupling to the cavity mode, a phase-shifting element should be placed at the middle of RC. In addition, the intensity profile is mirror-symmetric to the mid-plane. Note that this mirror symmetry is one of main features at the Fabry-Perot resonance expected from the governing equation [40]. Figure 4.6(b) shows the numerical result for the normalized *x*-component of the electric fields of the cavity mode (λ_R = 456 nm) for the OMR with 8 nm-thick nanofilm together with the intensity profile. Although it becomes somewhat asymmetric owing to the significant reflectance by the

nanofilm, the electrical field distribution shows no significant difference from the reference case. The local minimum shown in the intensity profile comes from the abrupt phase change at the nanofilm.

4.4.2. Effect of nanoislands on cavity mode

Figure 4.7 shows the calculated zero-order transmittance of a Fabry-Perot resonator with nanoislands as a function of p ranging from 20 to 200 nm under the incidence of TM-polarized plane wave. Here, t_2 and w of an individual nanoisland are 8 nm and 18 nm, respectively. As before, d is 110 nm which corresponds to λ_R = 550 nm (gray dotted line). The white dashed lines indicate the resonant wavelength of the LSPR mode of freestanding nanoislands in the medium having the refractive index of 1.6. Owing to the increase of the refractive index of environment, LSPR wavelength red-shifts compared to the freestanding case in Fig. 4.4. Interestingly, the LSPR mode of freestanding nanoislands exactly coincides with the dip of the transmittance. It indicates that no hybridization between the LSPR and the cavity mode occurs in our case. As expected from Fig. 4.4(a), the cavity mode red-shifts from the reference owing to the positive sign of $\Delta\phi$ at the right side of the LSPR mode and the magnitude of the red-shift becomes large with decreasing p. In the strong coupling regime for p under 60 nm, the magnitude of the red-shift rapidly increases on further decreasing p.

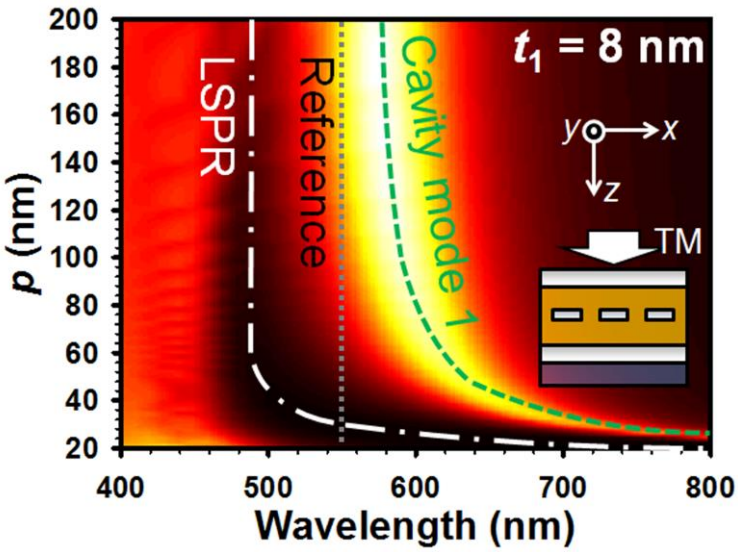

Figure 4.7: Zero order optical transmittances through the OMR with nanoislands inside RC under the incidence of TM-polarized plane wave for varying p at t_2 = 8 nm and w = 18 nm.

Figure 4.8 show the effect of w and t_2 on the cavity mode. For small t_2 of 3 nm, the opposite sign of $\Delta\phi$ at visible wavelengths with respect to the LSPR mode leads to two cavity modes, i.e., cavity mode 1 and 2. In the case of the red-shifted one, cavity mode 1, the magnitude of the shift becomes large with increasing w while the rate of change with respect to w becomes small with increasing t_2. It is clearly consistent with the behavior of the LSPR mode as described in Fig. 4.4. As for the transmittance at the resonant wavelength, it becomes small with increasing w while it becomes large with increasing t_1. In the case of t_2 = 15 nm, for example, the transmittance is over 40% irrespective of w.

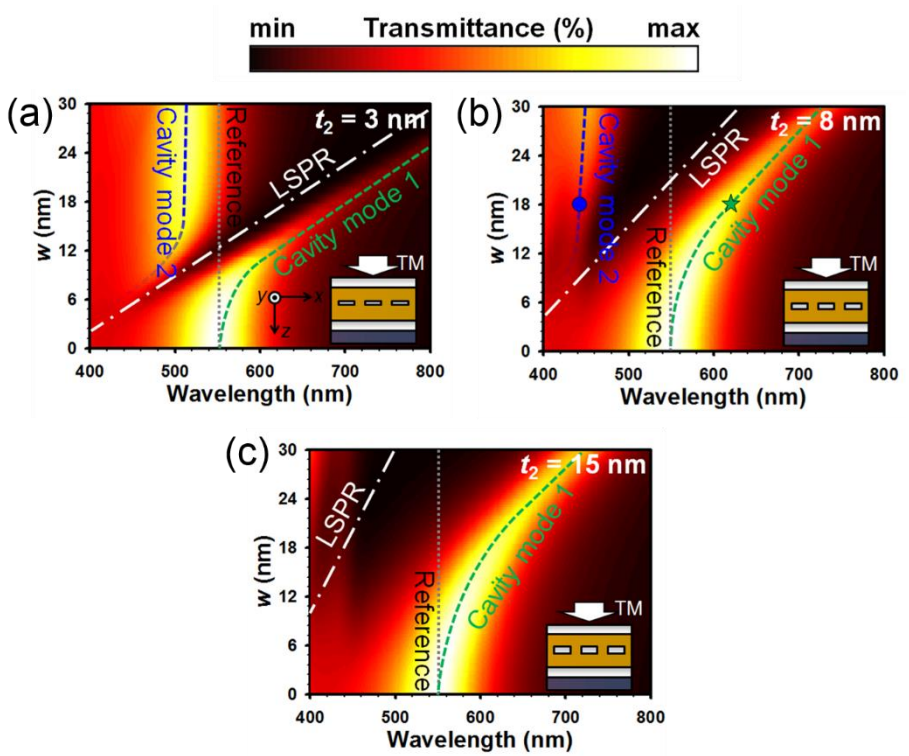

Figure 4.8: Zero order optical transmittances through the OMR with nanoislands inside RC under the incidence of TM-polarized plane wave for varying w at (a) t_2 = 3 nm, (b) t_2 = 8 nm, and (c) t_2 = 15 nm. In (a), (b), and (c), p is 60 nm. Here, the gray dotted line represents the reference while the blue and green dashed line represent the cavity mode 1 and 2 when the nanoislands are present inside RC. The white alternating dashed line represents the wavelength of the localized surface plasmon resonance (LSPR) for freestanding nanoislands in the same dielectric material as RC.

On the other hand, in the case of t_2 = 3 nm, it becomes as small as 13% at w = 20 nm. The significant decrease of the transmittance for t_2 = 3 nm comes from the overlap between the LSPR and cavity mode 1 due to the small $\Delta\phi$. In contrast to the cavity mode 1 which significantly shifts depending on w, the cavity mode 2 does not change appreciably. As for t_2, with increasing t_2, the cavity mode 2 shifts to shorter wavelengths before disappearing into ultraviolet (UV) regime. In the case of t_1 = 15 nm, as a result, the cavity mode 2 is out of visible wavelengths and there is only the cavity mode 1.

To investigate the nature of the cavity mode 1 and 2, the distributions of electric fields are calculated for t_2 = 8 nm and w = 18 nm. Figure 4.9 shows the calculated results for the normalized magnitude of the x-component of the electric fields inside RC. Here, the cavity mode 1 at λ_R = 618 nm (Fig. 4.9(b)) and 2 at λ_R = 441 nm (Fig. 4.9(a)) correspond to the case denoted by the blue circle and the green star denoted in Fig. 4.8(b). In contrast to the cavity mode 2 where the scattering by nanoislands is not intense, the strong scattering by nanoislands occurs in a diffusive manner for the cavity mode 1. In the case of the cavity mode 2, the nanoislands can be considered to behave similar to isolated nanofilms owing to the relatively small wavelength compared to that of LSPR. This intuition is partially verified from the fact that, at the left side of LSPR in Figs. 4.4(a)-4.4(c), the signs for two cases almost coincide to be negative and the magnitudes are covariant. In the case of the cavity mode 1, on the other hand, the strong diffusive scattering by nanoislands leads to the increase of the optical path and thus, the positive $\Delta\phi$.

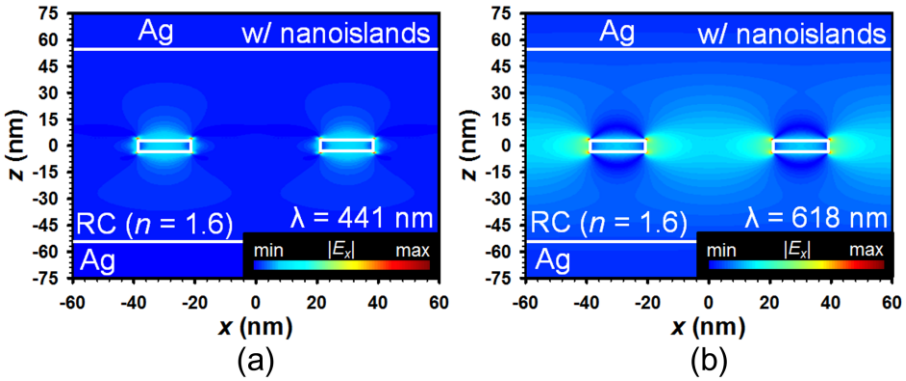

Figure 4.9: The electric field distribution for *x* component in RC at (a) λ_R = 441 nm and (b) λ_R = 618 nm corresponding to the blue circle and green star in 4.8(b) (t_2 = 8 nm and w = 18 nm), respectively.

4.4.3. Effect of nanostructures on color palette

Based on the above results, we numerically calculate the color palette of the OMR depending on the geometrical parameters when nanofilm and nanoislands are embedded at the middle of RC. Here, the color matching function of a standard observer is used to obtain the color coordinates from the transmittances [91]. The column surrounded by the white dashed line corresponds to the reference case where no phase-shifting elements are involved. When a nanofilm is embedded, the color changes from green to blue tone and, with increasing t_1, color becomes more bluish according to the shift of the cavity mode to shorter wavelengths. In the nanoislands case where two geometrical parameters of t_2 and w are involved, a wide range of colors is obtained. For small t_2 of 3 and 5 nm, color changes from green to turquoise or blue tone with increasing w since the cavity mode 2 plays a dominant role on

transmittance. For larger t_2, color mainly comes from the cavity mode 1 so that it becomes reddish with increasing w. Therefore, depending on the geometry of phase-shifting element, the full-color palette ranging from blue to red is obtained without changing the thickness of an OMR.

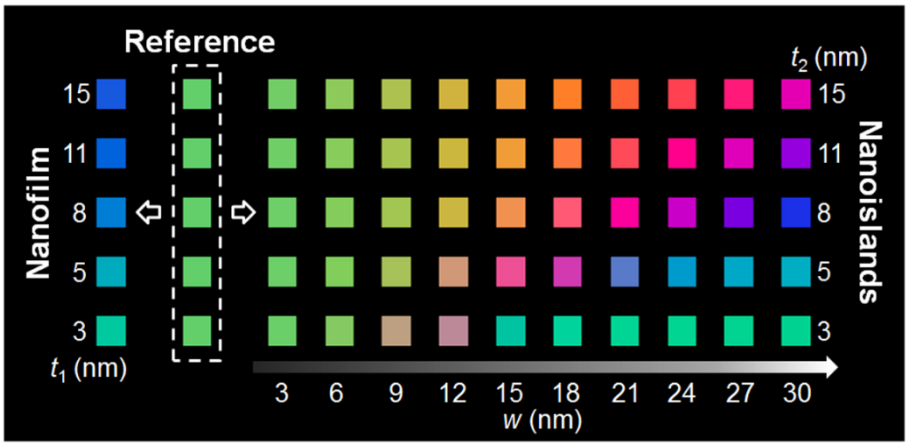

Figure 4.10: Color palette of the OMR with a nanofilm and nanoislands. The column enclosed by the white dashed line corresponds to the reference case where d = 110 nm. With respect to the reference, the column at the left side corresponds to the nanofilm case while those at the right side correspond to the nanoislands case.

4.5. Fabrication process

For the demonstration of our concept, of importance is to construct nanofilm and nanoislands and control their geometry. For this purpose, we use the island growth of silver during vacuum deposition under percolation threshold thickness [92-95]. Compared to the other options such as electron

beam lithography, the fabrication process is simple and suitable for a flexible substrate. In this approach, the size and the surface coverage of nanoislands can be controlled by the surface energy of silver and substrate and deposition conditions including rate, thickness, and chamber pressure. In general, as deposition thickness increases, the size and the surface coverage of nanoislands become large until it forms a continuous film. Using vacuum deposition, thus, both nanostructures can be constructed by controlling the deposition thickness.

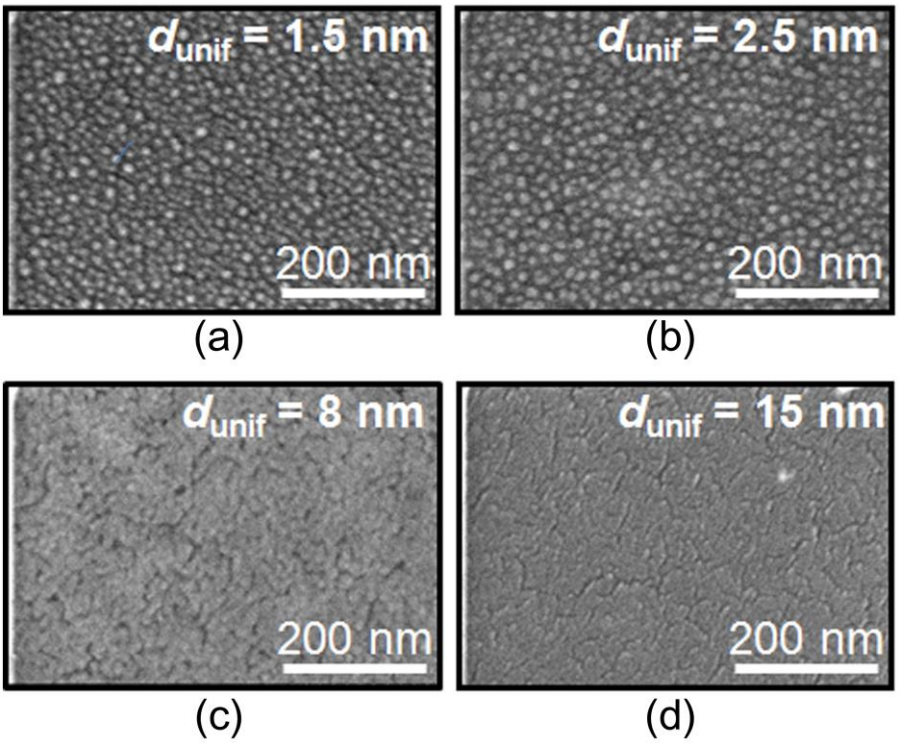

Figure 4.11: Scanning electron microscopic images of thermally deposited silver nanostructures for different thickness assuming uniform layer (d_{unif}) of (a) 1.5 nm, (b) 2.5 nm, (c) 8 nm, and (d) 15 nm.

For the fabrication of etalon-type OMRs having phase-shifting elements, a 20 nm-thick silver was first deposited as a TRL on a pre-cleaned glass or flexible polyethylene naphthalate (PEN) substrate. After that, RC was spin-coated at the rate of 3000 rpm for 30 s with a photopolymer (SU-8 2005; MicroChem) diluted in 5 wt. % with propylene glycol monomethyl ether acetate (PGMEA; Sigma Aldrich). Note that SU-8 is highly transparent (over 90 % in transmittance) at visible wavelengths and orthogonal to most of solvents after being cured by UV light, allowing for spin-coating another layers on a preformed SU-8 layer.

To construct phase shifting elements, silver was vacuum-deposited on the photopolymer layers for different thicknesses. For nanoislands, silver was deposited at the rate of 0.1 nm/s and the chamber pressure of 1×10^{-5} Torr at the thickness of 1.5 nm and 2.5 nm using thermal evaporator (MHS-1800; Muhan Vacuum). For nanofilms, the silver was deposited in 8 nm and 15 nm thicknesses using electron gun evaporator (ZZS550-2/D; Maestech) since higher vacuum is required for the formation of a uniform film near the percolation threshold thickness. The deposition rate and the chamber pressure was 2 nm/s and 5×10^{-6} Torr, respectively. In addition, the surface of the photopolymer layer was treated with UV/ozone (AHS-1700; Ahtech LTS) for high surface energy to promote the film growth of silver during deposition.

The deposited silver nanostructures were characterized using scanning electron microscopy (SEM) (S-4800; Hitachi) and atomic force microscopy (AFM) (XE-150; PSIA). In the case of a full-color element, photolithography was carried out to pre-define patterns on SU-8 layer before silver deposition for

phase-shifting elements. The photoresist (AZ 1512; AZ electronic materials) was then removed by acetone (Sigma Aldrich). These processes were repeated several times to pattern different phase-shifting elements. After that, RC was spin-coated again at the same condition so that the nanstructures were at the middle of RC. The fabrication of color elements were completed by the thermal deposition of the other TRL on the top of RC.

The observed SEM images of silver nanostructures are shown in Fig. 4.11. Since the deposition thickness is generally different from the height of nanostructures, the thickness assuming a uniform layer (d_{unif}) is considered. From the SEM images of Figs 4.11(a) and 4.11(b), it is clear that, for d_{unif} = 1.5 nm and 2.5 nm, silver nanoislands were constructed.

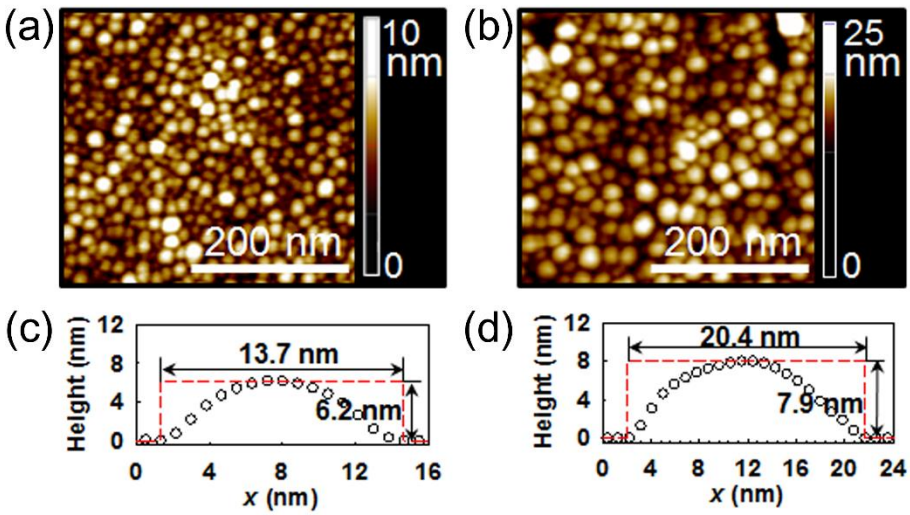

Figure 4.12: (a) and (b) show the atomic force microscopic images corresponding for d_{unif} = 1.5 nm and 2.5 nm. (c) and (d) represent the average profile of an individual nanoislands in (a) and (b).

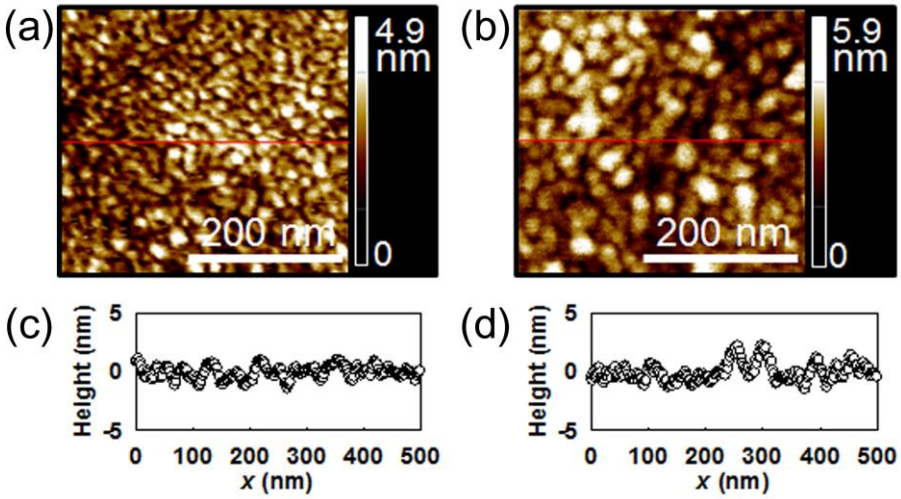

Figure 4.13: (a) and (b) show the atomic force microscopic images corresponding for d_{unif} = 8 nm and 15 nm. (c) and (d) represent the line profile along the red solid lines in (a) and (b).

The surface coverage, r_s, being the ratio of the area occupied by nanoislands in unit area, was 24.2% and 31.7%, respectively. It should be noted that, owing to low r_s, their optical behaviors are well described in the framework of an effective medium theory. It enables to obtain reasonable numerical results for three-dimensional cases from two-dimensional approximation [96]. In contrast, the SEM images in Figs. 4.11(c) and 4.11(d) shows that although incidental crack are present, silver forms nanofilm structures for d_{unif} = 8 nm and 15 nm. Figure 4.12 shows the AFM images as well as average profiles of nanoislands for d_{unif} = 1.5 nm and 2.5 nm. From the AFM images of Figs. 4.12(a) and 4.12(b), twenty individual nanoislands are randomly selected and their profiles were extracted to obtain average profiles. The average profiles in Fig. 4.12(c) shows

that, for d_{unif} = 1.5 nm, the thickness and the width are 6.2 nm and 13.7 nm, respectively. For d_{unif} = 2.5 nm in Fig. 4.12(d), the dimensions increase to 7.9 nm and 20.4 nm, respectively. Figure 4.13 shows the AFM images of nanofilms for d_{unif} = 8 nm and 15 nm. From the AFM images in Figs. 4.13(a) and 4.13(b), it is clear that the grain size becomes large for larger d_{unif} of 15 nm. Figures 4.13(c) and 4.13(d) represent the line profiles along the red solid lines in the AFM images, showing significantly low surface roughness in both cases.

4.6. Color characteristics of nanostructure-embedded optical micro-resonators

Figure 4.14(a) shows the experimental and the numerical results for the transmittances of OMRs having two different nanofilms for d_{unif} = 8 nm and 15 nm in RC together with that for the reference case having no nanofilm. For numerical simulation, d is set to be 114 nm, giving the resonant wavelength of 570 nm for the reference. In this case, the cavity mode blue-shifts to 442 nm for d_{unif} = 8 nm and 422 nm for d_{unif} = 15 nm, which are in an appreciable agreement with 453 nm and 421 nm from the numerical results. The discrepancy between the peak transmittances for the experimental and numerical results originates from the incidental cracks present in the film. Figure 4.14(b) corresponds to the case of nanoislands for d_{unif} = 1.5 nm and 2.5 nm together with the reference case.

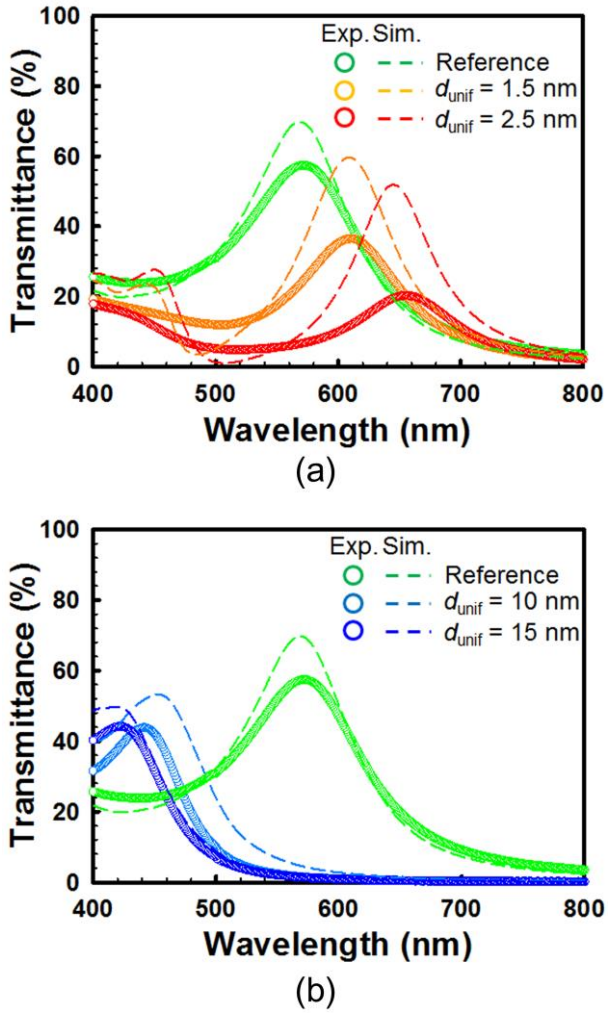

Figure 4.14: Transmittances of an OMR (a) with a nanofilm for d_{unif} = 8 nm and 15 nm (b) with nanoislands for d_{unif} = 1.5 nm and 2.5 nm, together with that for the reference where no nanostructures are present inside RC.

Here, the profile of nanoislands was assumed to be rectangular and their geometrical parameters are obtained from Fig. 4.12. The periodicity of nanoislands is determined so that the surface coverage for two-dimensional

case coincides with that for three dimensional case. It requires that the periodicities for d_{unif} = 1.5 nm and 2.5 nm are 56.7 nm and 64.4 nm, respectively. As can be seen in the figure, with nanoislands, the cavity mode 1 red-shifts to 610 nm for d_{unif} = 1.5 nm and 656 nm for d_{unif} = 2.5 nm. The increase in the magnitude of the red-shift with d_{unif} comes from the resultant increase of nanoisland size (t_2 and w) as well as surface coverage. The positions of the cavity modes 1 show no significant deviation from 609 nm and 645 nm expected from the numerical results although the peak transmittances are relatively lower owing to the random distribution as well as poly-diversity of real nanoislands. Note that the absence of the cavity mode 2 might be attributed to the hemispherical profile of the real nanoislands which helps to scatter incident light in a more diffusive manner.

Figure 4.15(a) shows a flexible color element on PEN substrate. From the figure, it is clearly shown that three primary colors of R, G, and B are well achieved on a single substrate. Here, white backlight is placed behind the color element. The green color for the background comes from the OMR without any nanostructures. For the red color of 'SNU', the nanoislands for d_{unif} = 2.5 nm (the average height of 7.9 nm) are employed while, for the blue color of 'MIPD', the nanofilm for d_{unif} = 8 nm is. Figure 4.15(b) shows the flexible color element during being bent. Since the incident angle of the backlight on the color element increases at the periphery of the color element, the color changes from green to blue. In contrast, the colors of 'SNU' and 'MIPD' exhibit no significant changes. In the case of 'SNU', the cavity mode 1 plays an important role on the generation of red color. The cavity mode 1 is more independent on incident

angle than the cavity mode for the reference case since it requires smaller RC thickness for the given resonant wavelength.

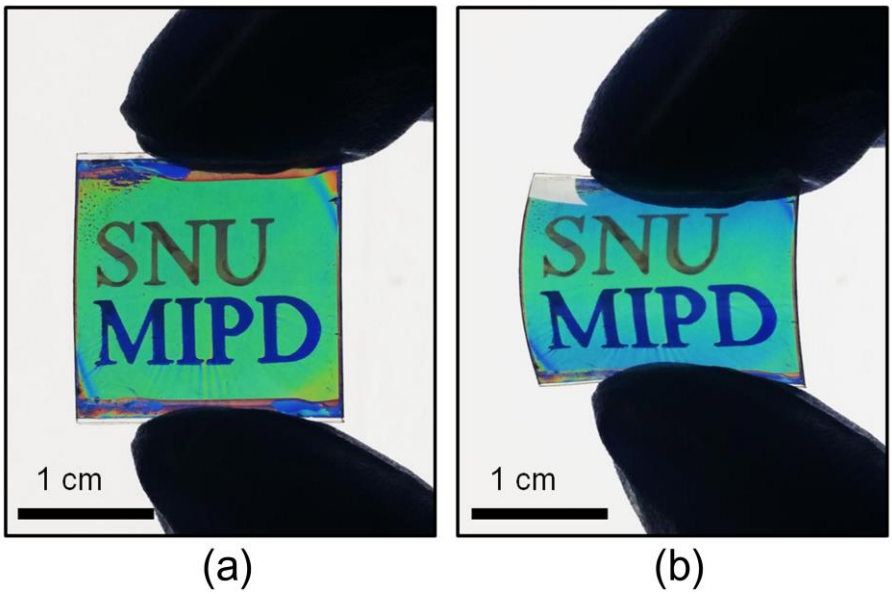

Figure 4.15: Microscopic images of a color element based on the nanostructure-embedded OMR constructed on a flexible substrate (a) before and (b) after bending. Here, the green color for background comes from the OMR without nanostructures (reference) while the red and blue colors for 'SNU' and 'MIPD' are attributed to the embedded nanoislands (d_{unif} = 2.5 nm) and nanofilm (d_{unif} = 8 nm), respectively.

4.7. Angle-independency in nanoislands case

As shown in Eq. (2.5), the angle dependency of resonant peak is proportional to d for given order of resonance. In nanoislands case where the

resonant peak red-shifts without change in d, thus, angle-dependency is expected to be reduced compared to reference case for given peak wavelength. Figures 4.16(a) and 4.16(b) show the simulation results for the angle-dependency of conventional OMRs having peak wavelengths at 550 nm and 580 nm for varying the incident angle from 0° to 90°. The shifts of peak wavelengths are both about 100 nm. In addition, the bandwidth becomes significantly large with increasing the incident angle. It is attributed to the decrease of reflectance at TRL under the incidence of TM-polarized light.

Figures 4.16(c) and 4.16(d) show the angle dependency of OMRs having metallic nanoislands inside RC. Here, d of all OMRs is 85 nm. In the case of metallic nanoislands for d_{unif} = 1.5 nm in Fig. 4.16(c), w and h are 13.7 nm and 6.2 nm, respectively. On the other hand, figure 4.16(d) shows the results for d_{unif} = 2.5 nm, where w and h are 20.4 nm and 7.9 nm, respectively. Compared to the reference case, the shift of resonant peaks becomes as small as 20 nm in both cases. As shown in the figure, the resonant wavelengths of the localized surface plasmon and corresponding optical transmittances are almost invariant with the incident angle. It suggested that the angle dependency mostly comes from $nd\cos\theta$ term in Eq. (2.5). Therefore, the angle dependency in nanoislands case is essentially identical with or even better than that of OMRs having d of 85 nm. The experimental results shows a good agreement with the numerical results.

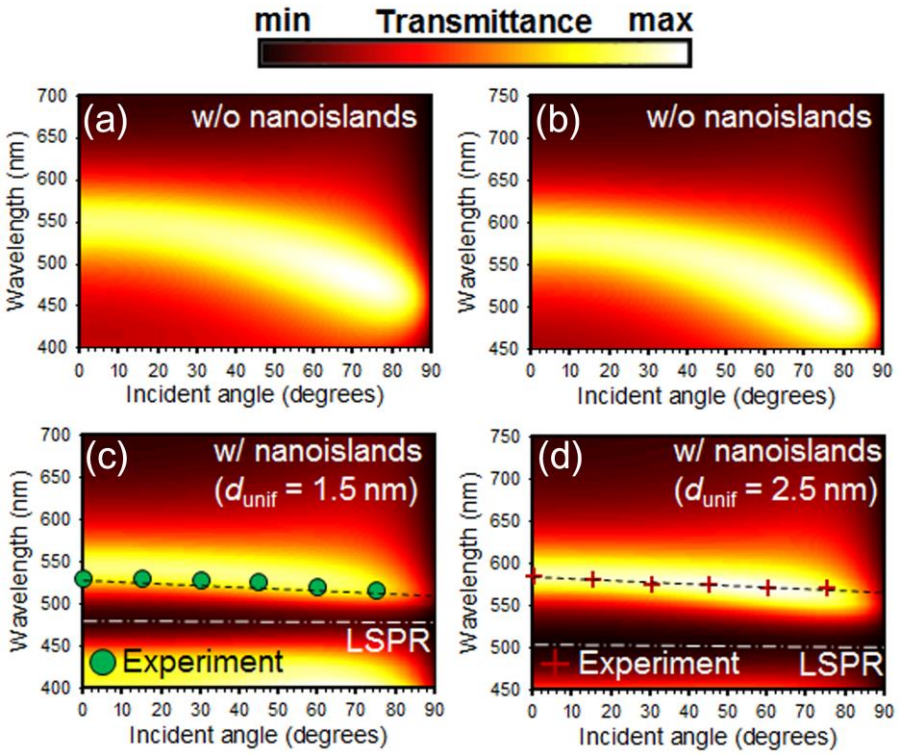

Figure 4.16: Angle dependency of optical transmittances through conventional OMRs having the resonant wavelength at (a) λ_R = 550 nm and (b) λ_R = 580 nm, and through OMRs incorporating nanoislands for (c) d_{unif} = 1.5 nm and (d) d_{unif} = 2.5 nm. In (c) and (d), the symbols of green circle and red cross represent the experimental results for peak wavelengths as a function of incident angle and white alternate lines does localized surface plasmon resonances.

By utilizing the angle-independent property in the nanoislands case, we fabricated an angle-invariant and flexible color element as shown in Fig 4.17. For d = 85 nm, different sizes of nanoislands are deposited onto different regions. In the region of 'SNU', nanoislands for d_{unif} = 1.5 nm are deposited

while in the region of ‘MIPD’, those for d_{unif} = 2.5 nm are. On the other hand, no nanoislands are deposited onto the marginal space. In comparison with the blue color for the background, the regions of ‘SNU’ and ‘MIPD’ become green and red, which is consistent with the results in Fig 4.16. As shown in Fig. 4.17 (b), there is no color changes at the large viewing angle of 75°. Accordingly, our color elements retain its colors during being bent as shown in Fig. 4.17(c).

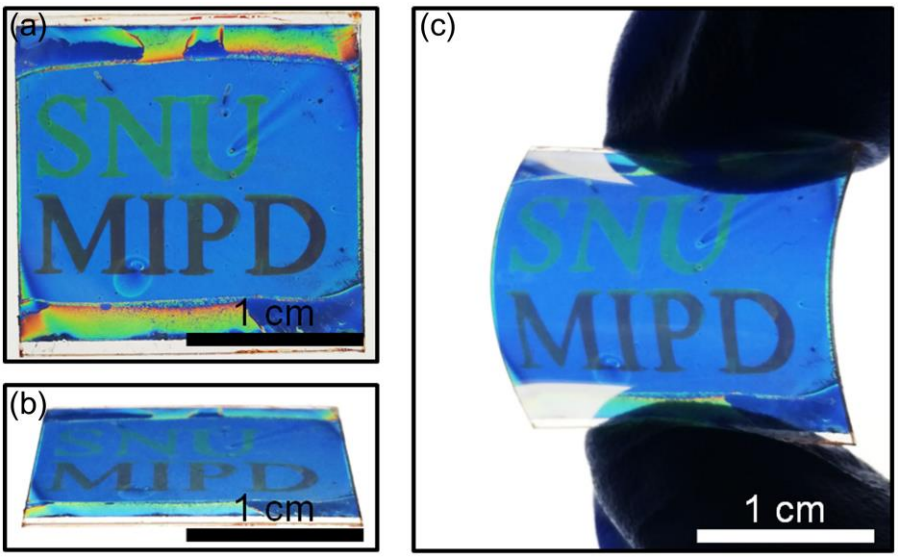

Figure 4.17: Microscopic images of a color element based on the nanoislands-embedded OMR constructed on a flexible substrate (a) from a front view and (b) at the viewing angle of 75˚. Here, the blue color for background comes from the OMR without nanoislands (reference) while the green and red colors for ‘SNU’ and ‘MIPD’ are attributed to the embedded nanoislands for d_{unif} = 1.5 nm and d_{unif} = 2.5 nm, respectively.

4.8. Summary

In summary, we investigated the effect of embedded silver nanofilm and nanoislands on the cavity mode of an OMR for full-color generation. It was found that, in both cases, the direction of the shift of the cavity mode is opposite to each other and the magnitude of the shift depends on the geometrical parameters of silver nanostructures. From the numerical results, the opposite effect by nanoislands and nanofilm was found to come from the different signs of phase retardation on transmission through these nanostructrues. The experimental results agreed well with the numerical results. In addition, the flexible color element incorporating nanoislands showed no significant color changes during being bent owing to the angle independent nature of the cavity modes. The effect of silver nanostructures presented here would pave the way toward realizing the angle-invariant and flexible full-color elements for a variety of visual applications such as electro-optic devices and images storage systems.

Chapter 5. Recording and Reading of Dual Images by Polarization

5.1. Introduction

Structural coloration has been extensively studied as a new platform for optical data storage since it provides a unique feature of coloring information. This feature facilitates the easy readout of information, making this platform suitable for image storage [10, 17-19, 31], bioassay [97-99], and anti-counterfeiting [6, 100, 101] applications. In particular, the image storage based on structural colors have attracted a lot of interest owing to long storage time and high stability against harsh conditions including strong light illumination, high temperature, and the exposure to humidity and chemicals. Until now, plasmonic nanostructures have been mostly employed as an image pixel whose color property is precisely controlled by the geometrical dimensions. However, the static nature of image pixel allows for the storage of only a single image limiting information density.

To record multiple images, an image pixel should exhibit different optical responses for the change of reading conditions. Until now, only a few cases have been reported toward multiplexed image storage, where metallic nanostructures having geometrical asymmetry are employed as an image pixel for anisotropic optical response [33, 102]. This optical anisotropy enables the recording of different images within the same device area and resolving them by polarization of incident light. However, this approach inevitably suffers

from low optical efficiency due to plasmon damping and the recording process requires high-resolution patterning techniques such as electron beam lithography limiting low-cost and large-area fabrication for practical applications. Therefore, it still remains as a challenge to develop new image storage platform for the simple and direct recording of dual images in a massively parallel manner.

In this chapter, we demonstrated the recording and reading of dual images resolved by the polarization of incident light. In our approach, an OMR incorporating photoalignment and liquid crystal polymer (LCP) layers is used as an image pixel. The optical anisotropy of an image pixel is determined by the polarization direction of exposure light for photoalignment. Two images are divided into three parts including the intersection between them, and two complementary images excluding the intersection. By applying a series of photoalignment processes through photomasks, three sets of image pixels for three regions are aligned in different directions and orthogonally arranged on the same substrate. Under certain reading polarizations, two original images are resolved. Moreover, we also demonstrate the recording of dual holograms within a single device area and the reconstruction of corresponding dual holographic images according to the polarization direction of monochromatic light source.

5.2. Basic concept

Figure 5.1 shows the basic concept of recording and reading dual images by the polarization of incident light. In our approach, we employ optically anisotropic image pixels whose optical responses are tunable by the polarized direction of incident light. Under unpolarized backlight, no image appears since the optical responses of image pixels are homogeneous over whole device area. For certain polarized light, however, the set of pixels for each of two images having identical optical axes exhibit the same colors being resolved from the other pixels. Depending on the direction of polarization, two different images are accordingly resolved.

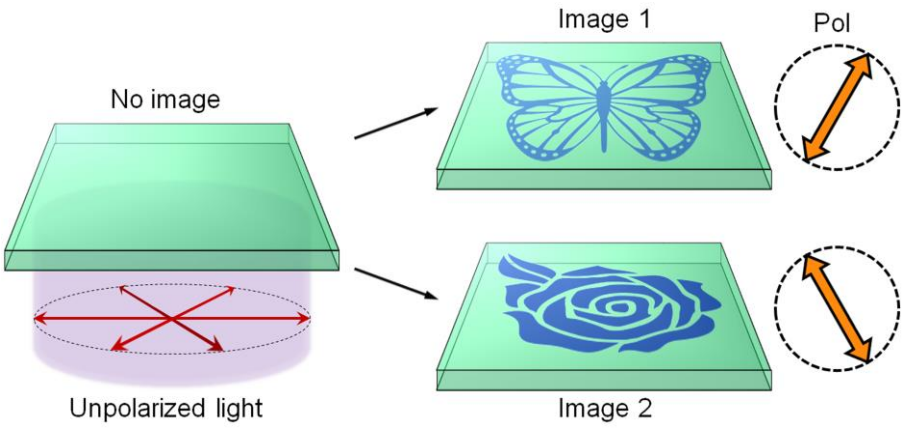

Figure 5.1: Schematic illustration of reading two different images recorded within the same device area. Under the incidence of unpolarized light, no image appears while, for polarized light, two different images are resolved by the direction of polarization.

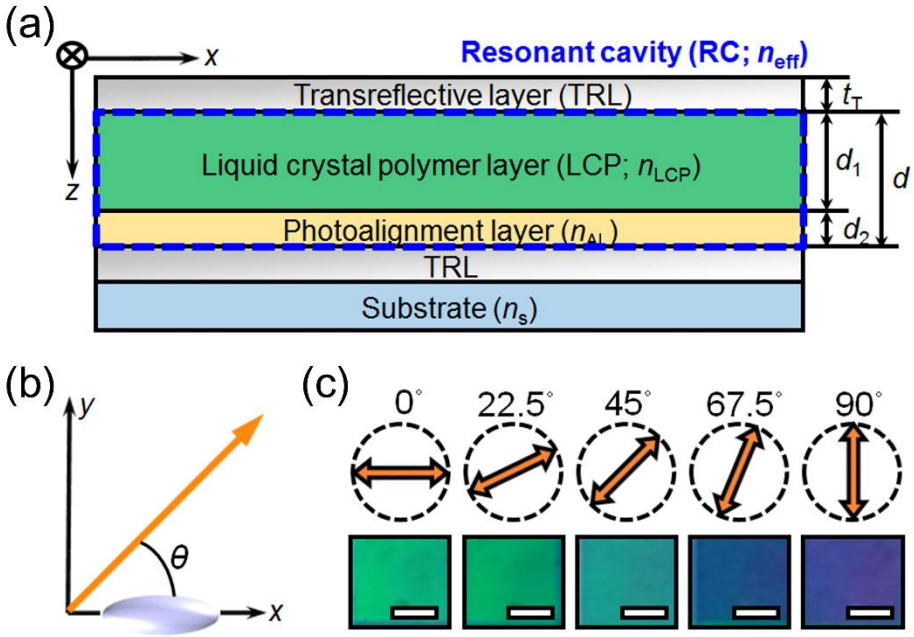

Figure 5.2: (a) Device architecture of an optically anisotropic image pixel. (b) The direction of LCP molecule alignment and polarization of incident light. (c) Microscopic images showing colors of an image pixel depending on θ.

5.3. Optical anisotropy of image pixel

The device structure of an optically anisotropic image pixel is schematically illustrated in Fig 5.2(a). It is basically an OMR having LCP and photoalignment layers as RC between two TRLs. Here, the thicknesses of LCP and photoalignment layers, and TRLs are d_1, d_2, and t_T, respectively. In addition, the refractive indices of LCP and photoalignment layer are denoted by n_{LCP} and n_{AL}, respectively. Since the optical path difference is determined by the product of the thickness (d) and refractive index (n_{eff}) of RC, the resonant wavelength

changes according to the polarized direction of incident light for given molecular alignment.

Figure 5.2(c) shows the microscopic images of an anisotropic OMR for different polarization angles for given direction of molecular alignment. Here, d_1 and d_2 are 603 nm and 80 nm, respectively. The direction of molecular alignment and the angle θ made with polarization is defined in Fig. 5.2(b). As you can see in the figure, the increase of θ from 0° to 90° leads to the color change from green to purple.

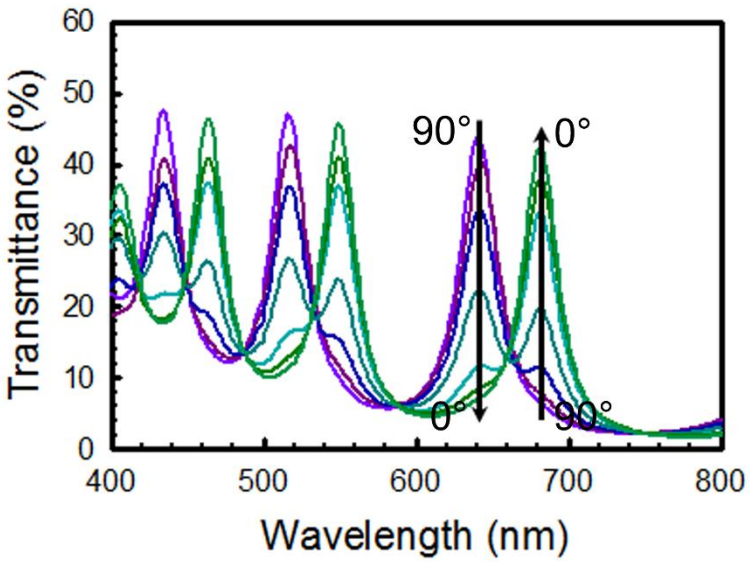

Figure 5.3: Optical transmittances through an anisotropic OMR for d_1 and d_2 of 603 nm, and 80 nm, under the incidence of different polarizations. The polarized angle changes from 0° to 90° at the interval of 15°.

Figure 5.3 shows corresponding optical transmittances for different θs. Owing to large d, three resonant peaks having different orders are within visible range. The optical transmittances at peak wavelengths are larger than 40%, which are significantly larger than the other systems based on surface plasmon resonance. Two independent spectrums are obtained for two orthogonal polarizations of 0° and 90°. The spectrum for θ = 90° shifts to the shorter wavelengths compared to that for θ = 90° owing to smaller n_{LCP}.

Under intermediate polarized directions, the spectrum is given as the linear combination of two independent basis. It can be easily understood from the fact that these polarizations can be decomposed into the linear combination of two orthogonal ones with the coefficients of cosθ and sinθ. Considering that transmittance is proportional to the intensity of electric fields, the transmittance under the polarization angle of θ, $T(\theta)$, is represented by

$$T(\theta) = \cos^2\theta \cdot T(0) + \sin^2\theta \cdot T(90^\circ). \quad (5.1)$$

The calculated results by using above equation show a good agreement with the experimental results.

5.4. Selection of color basis

In previous section, we showed that two independent spectrums for two orthogonal polarizations act as two basis spanning colors for intermediate polarizations. Since optical transmittance is mainly determined by d, we can select desired color basis for an image pixel. Figure 5.4 shows optical transmittances for two orthogonal polarizations when d_1 = 331 nm, 603 nm, and

943 nm. Three features with increasing thickness should be noted here. First, the number of resonant peaks become large, being consistent with Eq. (2.6) where the increase in the order of resonance leads to smaller $\Delta\lambda_{FSR}$. Second, the bandwidth of each resonant peak becomes small. It is attributed to the fact that the increase of thickness leads to the larger ratio of change in δ with respect to wavelength as inferred from Eq. (2.4). Third, the shift of peak wavelengths for two orthogonal polarizations becomes large. The last feature should be paid more attention since it is important parameter in terms of image contrast.

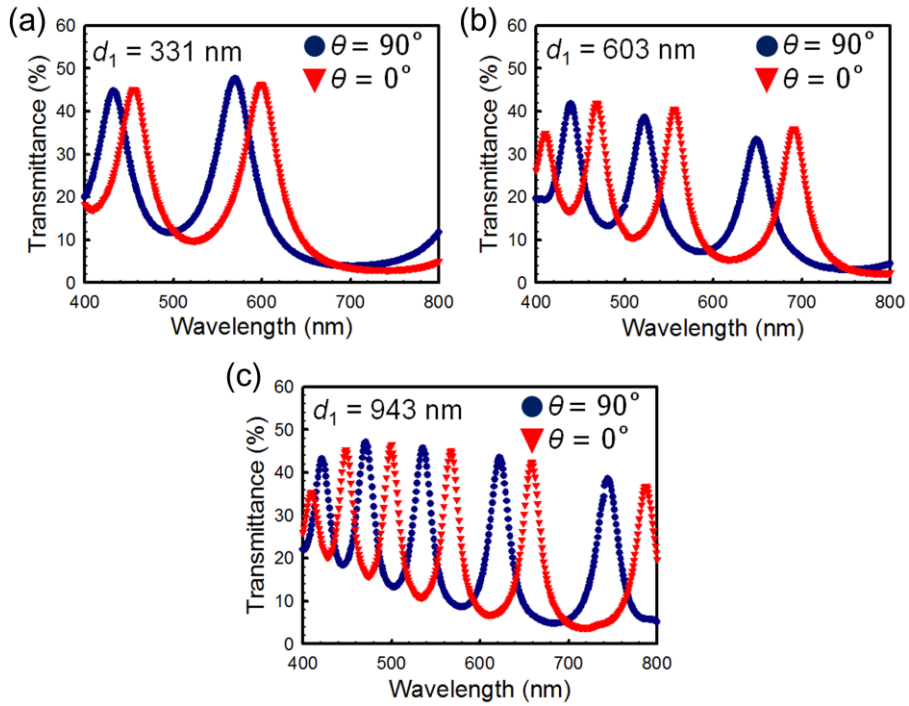

Figure 5.4: Polarization-dependent optical transmittances for (a) d_1 = 331 nm, (b) d_1 = 603 nm, and (c) d_1 = 943 nm. In all cases, d_2 is 80 nm.

Let us derive the expression for the peak shift for two orthogonal polarizations. Assuming that the refractive indices for θ = 90° and 0° are n and $n+\Delta n$, the resonance condition for the former case is given as Eq. (2.5) while that for the latter case is

$$(n+\Delta n)d\cos\theta = \frac{(\lambda+\Delta\lambda)}{2}\left[m - \sum_l \frac{\delta_l + \Delta\delta_l}{2\pi}\right]. \tag{5.2}$$

The subtraction of Eq. (2.5) from Eq. (5.2) gives

$$\Delta n d\cos\theta = \frac{\Delta\lambda}{2}\left[m - \sum\frac{\delta}{2\pi}\right] - \frac{\lambda}{2}\sum\frac{\Delta\delta}{2\pi}. \tag{5.3}$$

By dividing Eq. (5.3) by Eq. (2.5), we obtain

$$\frac{\Delta\lambda}{\lambda} = \frac{\Delta n}{n} + \frac{\sum\Delta\delta/2\pi}{m - \sum\delta/2\pi}. \tag{5.4}$$

Since rightmost term mostly becomes negative, the maximum value for normalized peak shift $\Delta\lambda/\lambda$ is $\Delta n/n$.

The experimental value of $\Delta\lambda/\lambda$ is plotted as a function of the order of resonance in Fig. 5.5. With increasing the order of resonance, $\Delta\lambda/\lambda$ becomes large, showing qualitative agreement with theoretical results calculated from Eq. (5.4). The discrepancy mainly comes from neglecting the isotropy of photoalignment layer and imperfection in molecular alignment. In both experimental and theoretical results, $\Delta\lambda/\lambda$ becomes saturated to the theoretical limitation of $\Delta n/n$.

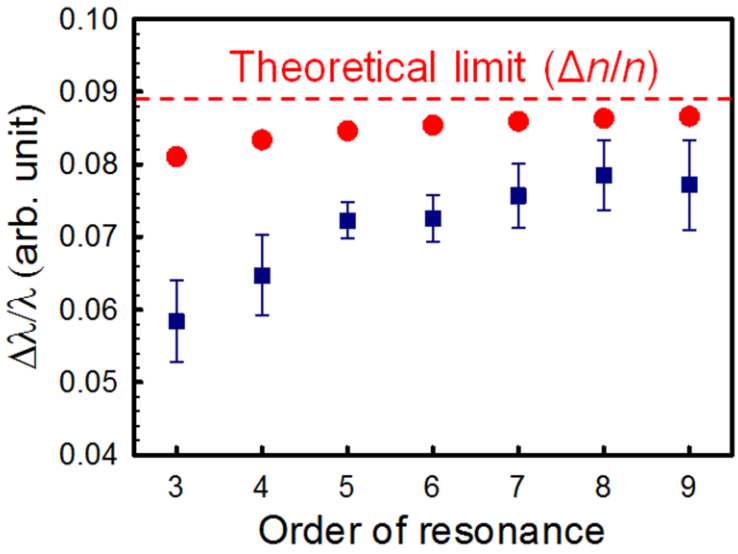

Figure 5.5: The normalized shift of peak wavelengths for two orthogonal polarizations as a function of the order of resonance. Circle and square symbols represent theoretical and experimental results, respectively. The each value is averaged from those obtained for different d_1s. The theoretical values are calculated from Eq. (5.4).

5.5. Dual direct image storage

5.5.1. Direct image recording scheme

Figure 5.6 shows the basic concept of recording and reading dual images. Three different polarization directions are designated to two images of 'SNU', 'MIPD', and background region. Here, it is important to choose three farthest directions in a polarization space for image contrast. In this case, three polarization should make an angle of 60° to each other as shown in Fig. 5.6(b).

In the general case of *n* polarizations, the angles between them should be 180°/*n*. By a series of photoalignment process, these polarization data are recorded in the direction of molecular alignment in an OMR.

In the symmetric case in Fig. 5.6(b), each image is readable by applying the same polarization as that for recording. On applying one of such polarizations, only corresponding image appears while two other images merge since the molecular directions for them make the same angle with the reading polarization.

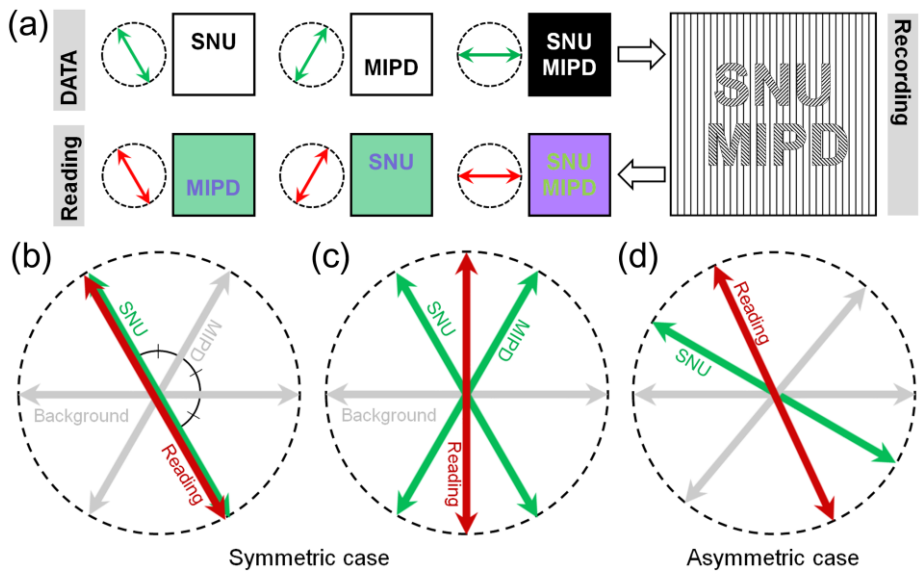

Figure 5.6: (a) Schematic illustration of recording process. (b) Reading one of images by applying the polarization having the same direction as that for recording in symmetric case. (c) Reading two images simultaneously under the mid-polarization in symmetric case. (d) Reading one of images in asymmetric case.

For mid-polarizations between those for two images (Fig. 5.6(c)), two images simultaneously appear. In the asymmetric case in Fig. 5.6(c), the reading polarization is different from that for recording and the image contrast accordingly decreases.

5.5.2. Recording dual images

Figure 5.7 shows the fabrication process for recording images. On glass substrate, 28 nm-thick silver is deposited by using thermal evaporator (MHS-1800; Muhan Vacuum) under the chamber pressure of 10^{-6} Torr at the rate of 5 nm/s. Then, the photoalignment layer (AL1084; JSR) was spin-coated at the rate of 10,000 rpm for 30 s, which gives the thickness of about 80 nm. The photoalignment layer was exposed several times through different photomasks for recorded images by UV light (center wavelength of 365 nm), which generate the spatial distribution of alignment directions. After that, LCP material (RMS-013C) was spin-coated on the photoalignment layer. During spin-coating process, LCP molecules are spontaneously aligned in different directions in each image domain. The alignment direction is perpendicular to that of exposure polarization. The spin-coated LCP layer was immediately cured by UV light for 1 minute. 28 nm-thick silver was then deposited again under the same condition before.

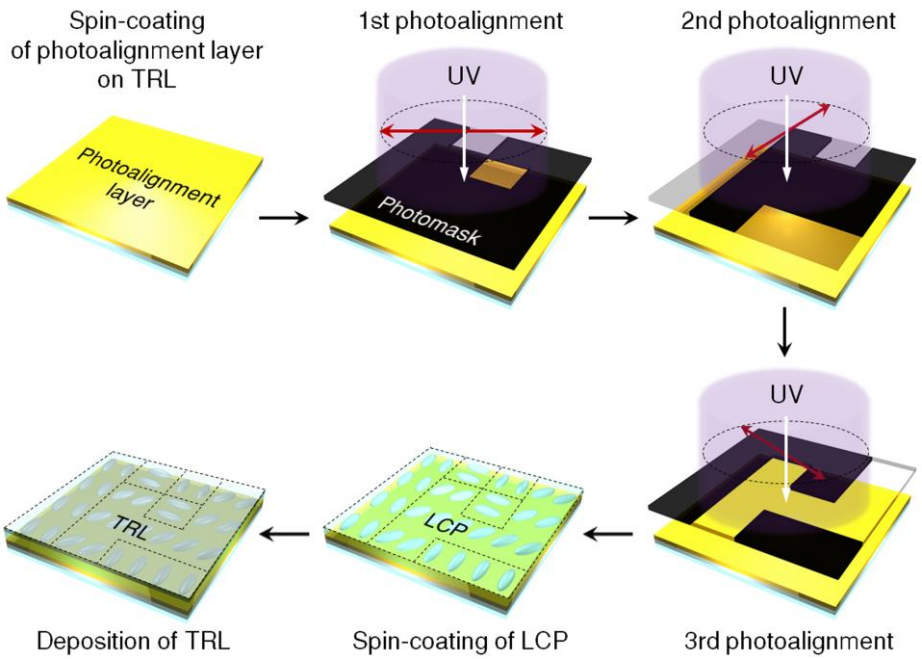

Figure 5.7: Fabrication process for recording different images in an anisotropic OMR.

5.5.3. Reading dual images

Figure 5.8 shows the microscopic images of the fabricated OMR where three domains are exposed by UV light polarized in different directions. Three domains correspond to the letters of 'SNU' and 'MIPD', and background. The corresponding angles of recording polarization are 30°, 150°, and 90° (Fig. 5.8(a)). Figure 5.8(b) schematically illustrates the reading configuration. Figure 5.8(c) shows the microscopic image of OMR under unpolarized white backlight. No image is observed in this case since the optical response from three domains are essentially identical. Figures 5.8(d), 5.8 (e), and 5.8 (f) show the

microscopic images for different reading polarizations identical with those for recording.

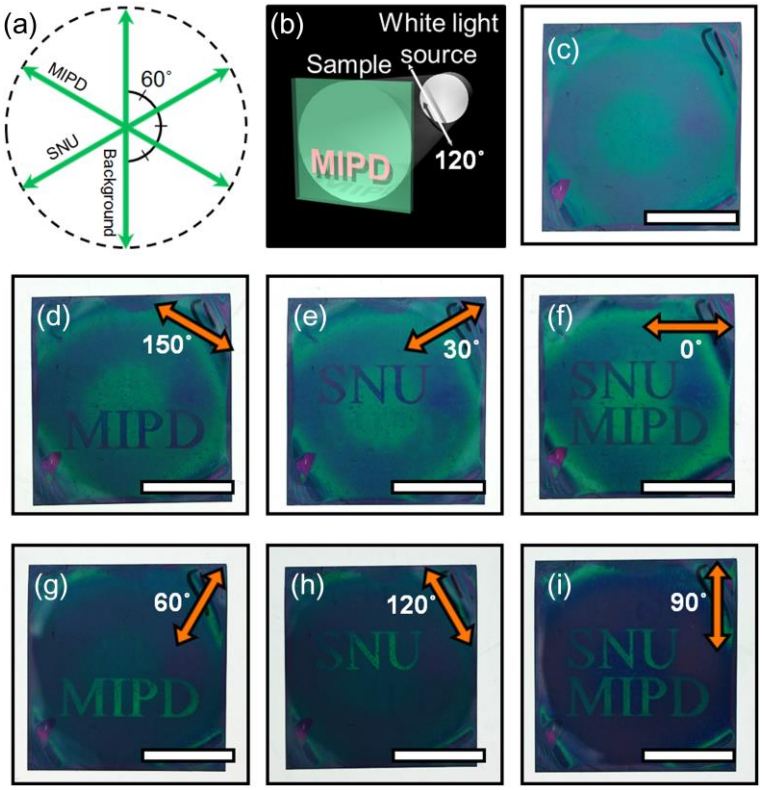

Figure 5.8: Reading of images recorded in different polarized directions. (a) The recording directions for two images and background. (b) Experimental setup for reading process. Microscopic image of an anisotropic OMR under unpolarized light. Microscopic images for different polarized angle of (d) 150°, (e) 30°, (f) 0°, (g) 60°, (h) 120°, and (i) 90°. The scale bars represent 1 cm.

As can be seen in the figure, the images of ‘MIPD’ and ‘SNU’ are resolved for the reading polarizations of 150° and 30°, respectively. For 0°, two image are simultaneously observed. Figures 5.8(g), 5.8(h), and 5.8(i) show the microscopic images for the reading polarizations perpendicular to those for 5.8(d), 5.8(e), and 5.8(f), respectively. In this case, the same images are observed with the colors for image and background being exchanged.

The above concept can be utilized for Quick Response (QR) code application. Figure 5.9 shows the microscopic images of polarization-dependent QR code. Here, ‘A’ and ‘B’ are randomly generated QR codes. Two sets corresponding to the QR codes of ‘A’ and ‘B’ are denoted by A and B, and their intersection is C. Here, three orthogonal images of A-C, C, and B-C instead of A and B are recorded to avoid multiple writing in intersection area. The recording directions are represented in Fig. 5.9(a). To observe the effect of recording angle between images on contrast, 0°, 45°, and 90° are selected for recording polarizations. Under unpolarized light, no image is observed as in Fig. 5.8(b). For three reading polarizations identical with those for recording, three recorded images are reproduced as shown in 5.9(c), 5.9(e), and 5.9(g), respectively. For reading polarizations that are at the middle of these polarizations, i.e., 22.5°, and 67.5°, QR code ‘A’ and ‘B’ are generated since two adjacent recorded images appear simultanesouly. Despite of crosstalk, the reconstructed images are well observed by naked eyes. There are three main advantages of polarization dependent QR codes. First, in contrast to conventional QR codes storing one bit per unit pixel, the polarization-dependent QR codes allow for the storage of more than three polarization states.

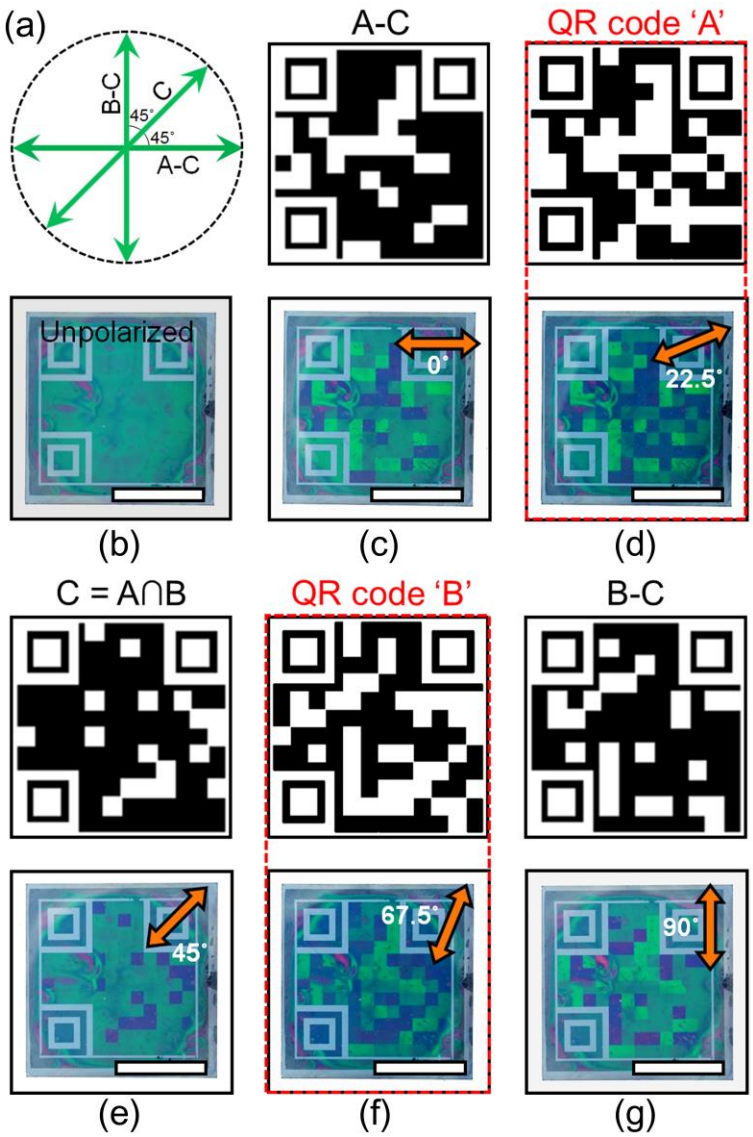

Figure 5.9: (a) Reading directions for images. (b) Microscopic image of an anisotropic OMR under unpolarized light. Original and microscopic images for different polarized angle of (c) 0°, (d) 22.5°, (e) 45°, (g) 67.5°, (g) 90°. The scale bars represent 1 cm.

Second, our QR codes cannot be easily replicable and readable ensuring more data security. Third, data classification becomes possible, providing faster access to certain category of information. Although QR code application is demonstrated here, this approach would be applicable to other areas such as anti-counterfeiting.

5.6. Dual holographic image storage

5.6.1. Hologram recording scheme

Another interesting application of above concept is the recording and reconstructing of dual binary holograms. The basic concept is schematically illustrated in Fig 5.10. First, two original images are Fourier-transformed into holograms. Two sets of binary-type pixels of A and B corresponding to the original images of 'A' and 'B' are divided into three orthogonal sets of A∩B (= C), A-C, and B-C. These three images are recorded under different recording polarizations into OMRs. As in the case of dual image reading, the original holograms corresponding to A and B appear under the reading polarizations at the middle of those for recording. Under the illumination of coherent light source, two different holographic images are reconstructed according to the reading polarizations as shown in Fig. 5.11.

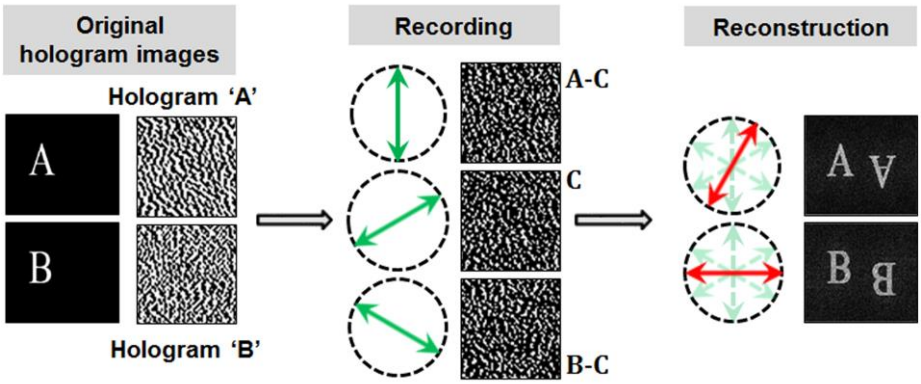

Figure 5.10: Schematic illustration of recording and reconstructing dual binary holograms. Original hologram images of A and B are divided into three orthogonal sets of C (=A∩B), A-C, and B-C. These three images are combined for intermediate polarizations for reconstruction of holographic images.

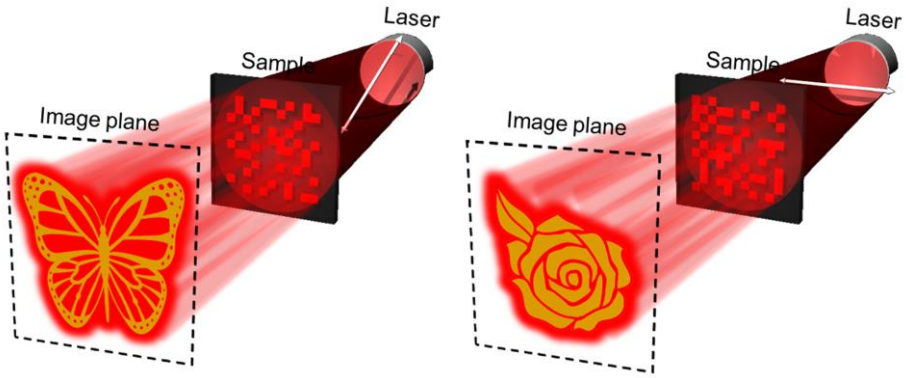

Figure 5. 11: Schematic illustration of reconstructed holographic images for different polarizations.

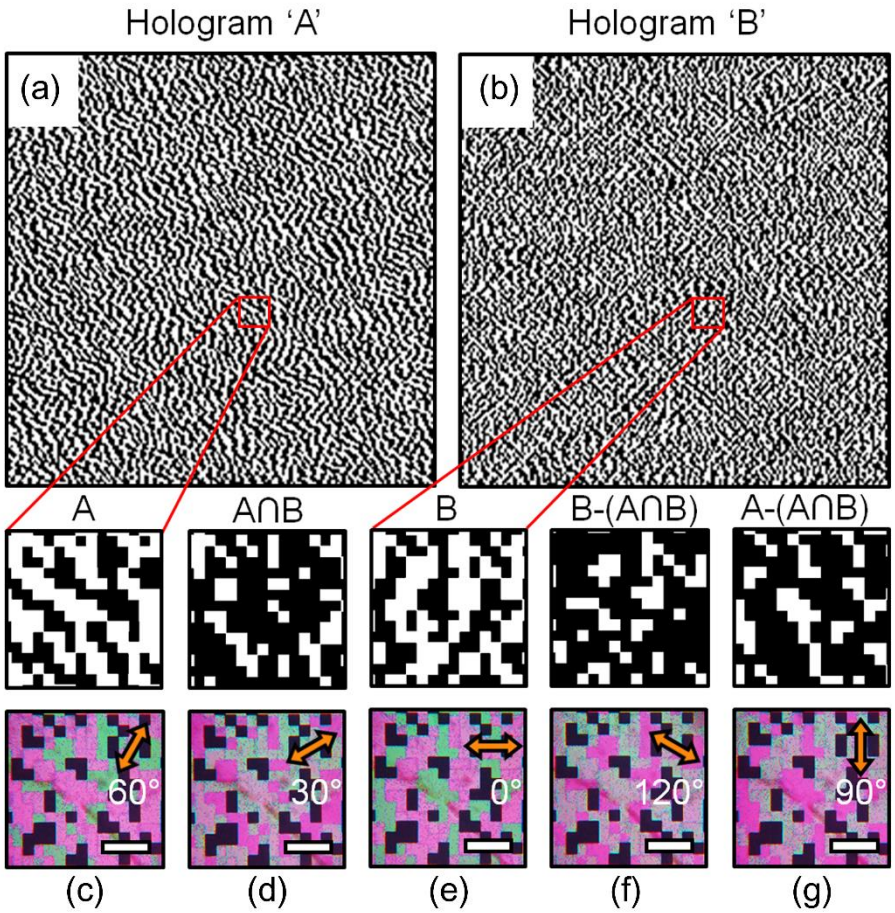

Figure 5.12: The original holograms of the letters of (a) 'A' and (b) 'B'. Microscopic images of an anisotropic OMR under different polarized angle of (c) 60°, (d) 30°, (e) 0° (f) 120°, and (g) 90°. The scale bars represent 300 μm.

5.6.2. Recording dual holograms

For the proof of concept, three images of A-C, C, and B-C are recorded under different recording polarizations of 90°, 30°, and 120° following the process mentioned in section 5.5.2. Here, d_1 is 603 nm and the pixels for

$(AUB)^C$ are blocked by 30 nm-thick aluminum film for intensity contrast of holograms. Figure 5.12 shows the microscopic images of holograms recorded in OMR under white backlight having different polarizations. Under the reading polarizations parallel to those for recording, the red-colored images of A-C, B-C, and C are observed in (c), (d), and (f). For the reading polarizations at the middle of them, the original holograms of 'A' and 'B' appear which are given in Fig 5.12(a) and 5.12(b).

5.6.3. Reconstructing dual holographic images

Let us now describe the reconstruction of holographic images from the recorded holograms in OMR. The center wavelength of light source for reconstruction should be overlapped with one of resonant peaks of optical transmittance in Fig. 5.3. We select He-Ne laser having the center wavelength of 660 nm for overlap with the longest resonant wavelength for image quality. For the estimation of intensity contrast as a function of reading polarization at the wavelength of 660 nm, the normalized intensity in red channel are first extracted from microscopic images for different reading polarizations in Fig. 5.12. The results are plotted in Fig 5.13. As can be seen clearly, the intensities of three recorded images of C, A-C, and B-C become minimized at the polarized angle of -60°(120°), 0°, and 60°, which is consistent with their recording polarization.

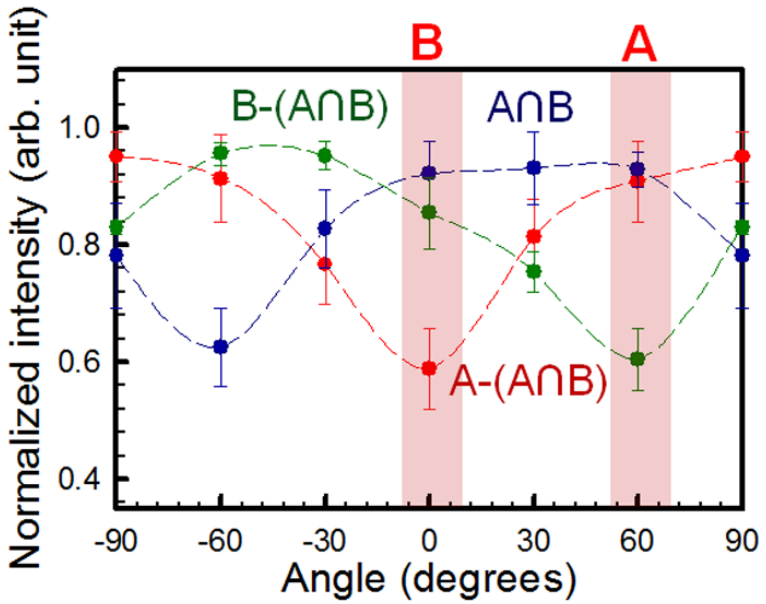

Figure 5.13: The normalized intensity in red channel as a function of polarized angle through different image regions of A∩B, B- A∩B, and A- A∩B.

Near the angle of 0°, the intensities for B-C and C become identical and hologram 'B' accordingly appears as in Fig. 5.12(e). The same principle holds for hologram 'A' at the angle of 60°. Therefore, it is expected that holographic images of 'A' and 'B' are reconstructed for the reading polarizations of 0° and 60°.

Figure 5.14(a) show the optical setup for the reconstruction of holographic images from recording medium. The monochromatic light from the laser is incident on the sample and their polarization changes by rotating half-wave retarder between them. We used Fourier lens to reduce the distance to image plane. Figure 5.14(b) shows the photograph of reconstructed holographic image

for the polarized angle of 60°. The original image of ‘A’ is clearly reproduced as expected from the microscopic image. Also, the image of ‘B’ is well reproduced at the angle of 0° as shown in Fig. 5.14(c).

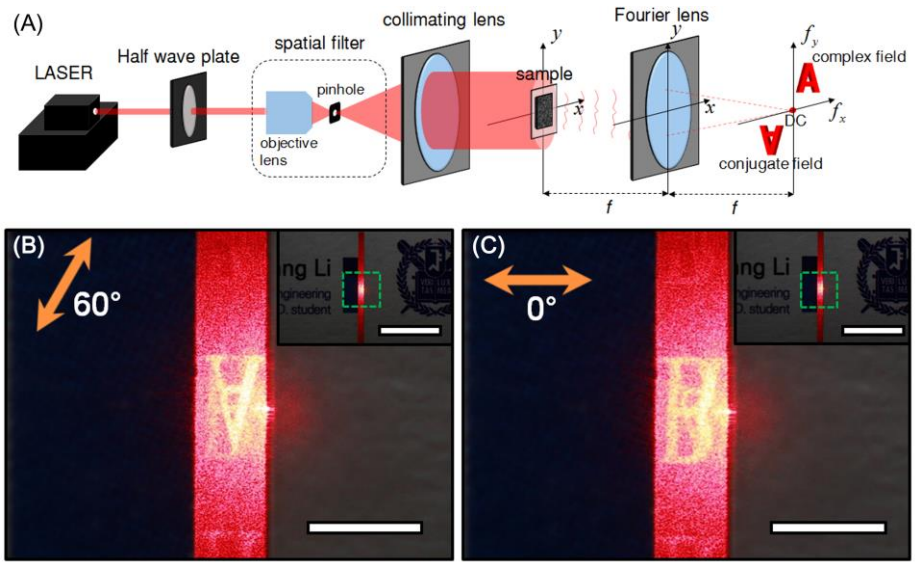

Figure 5.14: (a) Optical setup for the reconstruction of holographic images. Photographs of the holographic images of (b) the letter ‘A’ and (c) the letter ‘B’. Scale bars represents 1 mm while those for insets are 5 mm.

5.7. Summary

In summary, we presented the novel concept of recording and reading dual color images resolved by the polarization of incident light. In our approach, an OMR having photoalignment and LCP layers as RC was used as a polarization-dependent color pixel. The polarization direction of exposure light for photoalignment was directly recorded into the alignment direction of LCP

molecules within a color pixel. For recording dual images, the original images were divided into three orthogonal parts including the intersection of two images, and two complementary sets excluding intersection. Different sets of image pixels for three parts were fabricated within the same device area by a series of photoalignment processes under different recording polarizations. For the reading polarizations parallel or perpendicular to those for recording, three elementary images appear while for mid-polarizations, two original images are reproduced. In the light of this concept, we also demonstrated recording and reconstructing two different holographic images according to the polarization direction of monochromatic light source.

Chapter 6. Concluding Remarks

In this thesis, we demonstrated novel device architectures and fabrication techniques toward the realization of structural colors based on etalon-type OMRs. Four main challenges impeding the practical implementation of this type of structural colors were addressed; the integration of different color elements, the improvement of color gamut and angle dependency, the assignment of dynamic tunability, and the development of novel color applications. This thesis contains the theoretical considerations, architecture designs, and experimental demonstrations for resolving all these challenges.

In **Chapter 3**, we demonstrated the monolithic integration of different color elements by a series of transfer-printings of dielectric patterns for RCs. Two types of combinatorial color arrays were fabricated depending on whether dielectric patterns for different OMRs were transfer-printed in a pattern-by-pattern or a pattern-on-pattern manner. By using this concept, we demonstrated the prototype of LCDs incorporating the array of R, G, and B color elements as a color filtering unit. Our approach, allowing for the low-cost integration of different color elements over large area in a massively parallel manner, provides powerful solution for color integration challenge. In **Chapter 4**, we investigated the effect of embedded silver nanofilm and nanoislands on the cavity mode of OMRs for full-color generation within uniform RC layer and improvement of angle dependency. It was found that, in both cases, the direction of the shift of the cavity mode was opposite to each other and the

magnitude of the shift depended on the geometrical parameters of silver nanostructures. From the numerical results, the opposite effect by nanoislands and nanofilm was found to come from the different sign of phase retardation on transmission through these nanostructrues. The experimental results agreed well with the numerical results. In addition, the color element constructed on a flexible substrate showed no significant color changes during being bent owing to the angle independent nature of the cavity modes. The effect of embedded metallic nanostructure investigated here will enable the development of angle-independent full-color elements. In **Chapter 5**, we demonstrated the novel concept of recording and reading dual color images resolved by the polarization of incident light. In our approach, an OMR having photoalignment and LCP layers as RC was used as a polarization-dependent color pixel. For recording dual color images, different sets of polarization-dependent pixels for each image were integrated in an orthogonal manner by a series of photoalignment processes. During reading process, these images were resolved by polarization of incident light. In the light of this concept, we also demonstrated recording and reconstructing two different holographic images according to the polarization direction of monochromatic light source. The novel concept of recording and reading dual color images by polarization would help to develop high-density image storage systems for anti-counterfeiting systems and security labels.

The new device architectures and fabrication techniques presented here would pave the way toward the practical implantation of structural colors for a

wide range of visual applications ranging from color image storage to advanced display systems.

Bibliography

[1] S. Kinoshita and S. Yoshioka, "Structural colors in nature: the role of regularity and irregularity in the structure," ChemPhysChem **6**, 1442-1459 (2005).

[2] J. D. Joannopoulos, S. G. Johnson, J. N. Winn, and R. D. Meade, *Photonic crystals: molding the flow of light* (Princeton university press, 2011).

[3] O. Sato, S. Kubo, and Z.-Z. Gu, "Structural color films with lotus effects, superhydrophilicity, and tunable stop-bands," Accounts of Chemical Research **42**, 1-10 (2008).

[4] C. I. Aguirre, E. Reguera, and A. Stein, "Tunable colors in opals and inverse opal photonic crystals," Advanced Functional Materials **20**, 2565-2578 (2010).

[5] J. Ge and Y. Yin, "Responsive photonic crystals," Angewandte Chemie International Edition **50**, 1492-1522 (2011).

[6] H. S. Lee, T. S. Shim, H. Hwang, S.-M. Yang, and S.-H. Kim, "Colloidal photonic crystals toward structural color palettes for security materials," Chemistry of Materials **25**, 2684-2690 (2013).

[7] Y. Xia, B. Gates, and Z. Y. Li, "Self-assembly approaches to three-dimensional photonic crystals," Advanced Materials **13**, 409-413 (2001).

[8] Z. Z. Gu, H. Uetsuka, K. Takahashi, R. Nakajima, H. Onishi, A. Fujishima, and O. Sato, "Structural color and the lotus effect," Angewandte Chemie International Edition **42**, 894-897 (2003).

[9] Z. Wu, D. Lee, M. F. Rubner, and R. E. Cohen, "Structural color in porous, superhydrophilic, and self-cleaning SiO2/TiO2 Bragg stacks," Small **3**, 1445-1451 (2007).

[10] H. Kim, J. Ge, J. Kim, S.-E. Choi, H. Lee, H. Lee, W. Park, Y. Yin, and S. Kwon, "Structural colour printing using a magnetically tunable and lithographically fixable photonic crystal," Nature Photonics **3**, 534-540 (2009).

[11] W. L. Barnes, A. Dereux, and T. W. Ebbesen, "Surface plasmon subwavelength optics," Nature **424**, 824-830 (2003).

[12] C. Genet and T. Ebbesen, "Light in tiny holes," Nature **445**, 39-46 (2007).

[13] Q. Chen and D. R. Cumming, "High transmission and low color cross-talk plasmonic color filters using triangular-lattice hole arrays in aluminum films," Optics Express **18**, 14056-14062 (2010).

[14] D. Inoue, A. Miura, T. Nomura, H. Fujikawa, K. Sato, N. Ikeda, D. Tsuya, Y. Sugimoto, and Y. Koide, "Polarization independent visible color filter comprising an aluminum film with surface-plasmon enhanced transmission through a subwavelength array of holes," Applied Physics Letters **98**, 093113 (2011).

[15] S. Yokogawa, S. P. Burgos, and H. A. Atwater, "Plasmonic color filters for CMOS image sensor applications," Nano Letters **12**, 4349-4354 (2012).

[16] Q. Chen, D. Chitnis, K. Walls, T. D. Drysdale, S. Collins, and D. R. Cumming, "CMOS photodetectors integrated with plasmonic color filters," Photonics Technology Letters, IEEE **24**, 197-199 (2012).

[17] K. Kumar, H. Duan, R. S. Hegde, S. C. Koh, J. N. Wei, and J. K. Yang, "Printing colour at the optical diffraction limit," Nature Nanotechnology **7**, 557-561 (2012).

[18] A. S. Roberts, A. Pors, O. Albrektsen, and S. I. Bozhevolnyi, "Subwavelength plasmonic color printing protected for ambient use," Nano Letters **14**, 783-787 (2014).

[19] S. J. Tan, L. Zhang, D. Zhu, X. M. Goh, Y. M. Wang, K. Kumar, C.-W. Qiu, and J. K. Yang, "Plasmonic color palettes for photorealistic printing with aluminum nanostructures," Nano Letters **14**, 4023-4029 (2014).

[20] J. S. Clausen, E. Højlund-Nielsen, A. B. Christiansen, S. Yazdi, M. Grajower, H. Taha, U. Levy, A. Kristensen, and N. A. Mortensen, "Plasmonic metasurfaces for coloration of plastic consumer products," Nano Letters **14**, 4499-4504 (2014).

[21] Y.-T. Yoon and S.-S. Lee, "Transmission type color filter incorporating a silver film based etalon," Optics Express **18**, 5344-5349 (2010).

[22] C.-S. Park, V. R. Shrestha, S.-S. Lee, E.-S. Kim, and D.-Y. Choi, "Omnidirectional color filters capitalizing on a nano-resonator of Ag-TiO2-Ag integrated with a phase compensating dielectric overlay," Scientific Reports **5** (2015).

[23] C.-S. Park, V. R. Shrestha, S.-S. Lee, and D.-Y. Choi, "Trans-reflective color filters based on a phase compensated etalon enabling adjustable color saturation," Scientific Reports **6**, 25496 (2016).

[24] R. W. Sabnis, "Color filter technology for liquid crystal displays," Displays **20**, 119-129 (1999).

[25] E. Olczak, "Display substrate with reflective color filters," (Google Patents, 2005).

[26] Y. Ye, Y. Zhou, H. Zhang, and L. Chen, "Polarizing color filter based on a subwavelength metal–dielectric grating," Applied Optics **50**, 1356-1363 (2011).

[27] J. Guo, C. M. Huard, Y. Yang, Y. J. Shin, K. T. Lee, and L. J. Guo, "ITO-free, compact, color liquid crystal devices using integrated structural color filters and graphene electrodes," Advanced Optical Materials **2**, 435-441 (2014).

[28] H. J. Park, T. Xu, J. Y. Lee, A. Ledbetter, and L. J. Guo, "Photonic color filters integrated with organic solar cells for energy harvesting," ACS Nano **5**, 7055-7060 (2011).

[29] L. Frey, P. Parrein, J. Raby, C. Pellé, D. Hérault, M. Marty, and J. Michailos, "Color filters including infrared cut-off integrated on CMOS image sensor," Optics Express **19**, 13073-13080 (2011).

[30] Y. H. Chen, C. W. Chen, Z. Y. Huang, W. C. Lin, L. Y. Lin, F. Lin, K. T. Wong, and H. W. Lin, "Microcavity-embedded, colour-tuneable, transparent organic solar cells," Advanced Materials **26**, 1129-1134 (2014).

[31] F. Cheng, J. Gao, T. S. Luk, and X. Yang, "Structural color printing based on plasmonic metasurfaces of perfect light absorption," Scientific Reports **5** (2015).

[32] F. Cheng, J. Gao, L. Stan, D. Rosenmann, D. Czaplewski, and X. Yang, "Aluminum plasmonic metamaterials for structural color printing," Optics Express **23**, 14552-14560 (2015).

[33] X. M. Goh, Y. Zheng, S. J. Tan, L. Zhang, K. Kumar, C.-W. Qiu, and J. K. Yang, "Three-dimensional plasmonic stereoscopic prints in full colour," Nature Communications **5** (2014).

[34] D. Franklin, Y. Chen, A. Vazquez-Guardado, S. Modak, J. Boroumand, D. Xu, S.-T. Wu, and D. Chanda, "Polarization-independent actively tunable colour generation on imprinted plasmonic surfaces," Nature Communications **6** (2015).

[35] H. Fudouzi and T. Sawada, "Photonic rubber sheets with tunable color by elastic deformation," Langmuir **22**, 1365-1368 (2006).

[36] B. Viel, T. Ruhl, and G. P. Hellmann, "Reversible deformation of opal elastomers," Chemistry of Materials **19**, 5673-5679 (2007).

[37] E. P. Chan, J. J. Walish, A. M. Urbas, and E. L. Thomas, "Mechanochromic photonic gels," Advanced Materials **25**, 3934-3947 (2013).

[38] A. C. Arsenault, D. P. Puzzo, I. Manners, and G. A. Ozin, "Photonic-crystal full-colour displays," Nature Photonics **1**, 468-472 (2007).

[39] I. Lee, D. Kim, J. Kal, H. Baek, D. Kwak, D. Go, E. Kim, C. Kang, J. Chung, and Y. Jang, "Quasi-amorphous colloidal structures for

electrically tunable full-color photonic pixels with angle-independency," Advanced Materials **22**, 4973-4977 (2010).

[40] K. Hwang, D. Kwak, C. Kang, D. Kim, Y. Ahn, and Y. Kang, "Electrically tunable hysteretic photonic gels for nonvolatile display pixels," Angewandte Chemie International Edition **50**, 6311-6314 (2011).

[41] J. Ge, H. Lee, L. He, J. Kim, Z. Lu, H. Kim, J. Goebl, S. Kwon, and Y. Yin, "Magnetochromatic microspheres: rotating photonic crystals," Journal of the American Chemical Society **131**, 15687-15694 (2009).

[42] J. Kim, Y. Song, L. He, H. Kim, H. Lee, W. Park, Y. Yin, and S. Kwon, "Real-Time optofluidic synthesis of magnetochromatic microspheres for reversible structural color patterning," Small **7**, 1163-1168 (2011).

[43] J. Kim, S. E. Choi, H. Lee, and S. Kwon, "Magnetochromatic microactuators for a micropixellated color-changing surface," Advanced Materials **25**, 1415-1419 (2013).

[44] Z. Wang, J. Zhang, J. Li, J. Xie, Y. Li, S. Liang, Z. Tian, C. Li, Z. Wang, and T. Wang, "Colorful detection of organic solvents based on responsive organic/inorganic hybrid one-dimensional photonic crystals," Journal of Materials Chemistry **21**, 1264-1270 (2011).

[45] C. Fenzl, T. Hirsch, and O. S. Wolfbeis, "Photonic crystals for chemical sensing and biosensing," Angewandte Chemie International Edition **53**, 3318-3335 (2014).

[46] R. A. Barry and P. Wiltzius, "Humidity-sensing inverse opal hydrogels," Langmuir **22**, 1369-1374 (2006).

[47] E. Tian, J. Wang, Y. Zheng, Y. Song, L. Jiang, and D. Zhu, "Colorful humidity sensitive photonic crystal hydrogel," Journal of Material Chemistry **18**, 1116-1122 (2008).

[48] J. H. Kim, J. H. Moon, S.-Y. Lee, and J. Park, "Biologically inspired humidity sensor based on three-dimensional photonic crystals," Applied Physics Letters **97**, 103701 (2010).

[49] A. W. Clark and J. M. Cooper, "Plasmon shaping by using protein nanoarrays and molecular lithography to engineer structural color," Angewandte Chemie **124**, 3622-3626 (2012).

[50] M. M. Hawkeye and M. J. Brett, "Optimized colorimetric photonic-crystal humidity sensor fabricated using glancing angle deposition," Advanced Functional Materials **21**, 3652-3658 (2011).

[51] H. S. Lim, J.-H. Lee, J. J. Walish, and E. L. Thomas, "Dynamic swelling of tunable full-color block copolymer photonic gels via counterion exchange," ACS nano **6**, 8933-8939 (2012).

[52] G. A. Ozin and A. C. Arsenault, "P-Ink and elastiInk from lab to market," Materials Today **11**, 44-51 (2008).

[53] J. Homola, S. S. Yee, and G. Gauglitz, "Surface plasmon resonance sensors: review," Sensors and Actuators B: Chemical **54**, 3-15 (1999).

[54] J. Homola and M. Piliarik, Surface plasmon resonance (SPR) sensors (Springer, 2006).

[55] K. A. Willets and R. P. Van Duyne, "Localized surface plasmon resonance spectroscopy and sensing," Annual Revivew of Physical Chemistry **58**, 267-297 (2007).

[56] X. Zhu, L. Shi, X. Liu, J. Zi, and Z. Wang, "A mechanically tunable plasmonic structure composed of a monolayer array of metal-capped colloidal spheres on an elastomeric substrate," Nano Research **3**, 807-812 (2010).

[57] X. Han, Y. Liu, and Y. Yin, "Colorimetric stress memory sensor based on disassembly of gold nanoparticle chains," Nano Letters **14**, 2466-2470 (2014).

[58] Z. Li, S. Butun, and K. Aydin, "Large-area, lithography-free super absorbers and color filters at visible frequencies using ultrathin metallic films," ACS Photonics **2**, 183-188 (2015).

[59] M. Vaughan, The Fabry-Perot interferometer: history, theory, practice and applications (CRC press, 1989).

[60] V. R. Shrestha, S.-S. Lee, E.-S. Kim, and D.-Y. Choi, "Non-iridescent transmissive structural color filter featuring highly efficient transmission and high excitation purity," Scientific Reports **4** (2014).

[61] M. A. Kats, R. Blanchard, P. Genevet, and F. Capasso, "Nanometre optical coatings based on strong interference effects in highly absorbing media," Nature Materials **12**, 20-24 (2013).

[62] K.-T. Lee, S. Seo, J. Y. Lee, and L. J. Guo, "Ultrathin metal-semiconductor-metal resonator for angle invariant visible band transmission filters," Applied Physics Letters **104**, 231112 (2014).

[63] K. T. Lee, S. Seo, and L. J. Guo, "High-Color-Purity Subtractive Color Filters with a Wide Viewing Angle Based on Plasmonic Perfect Absorbers," Advanced Optical Materials **3**, 347-352 (2015).

[64] K.-T. Lee, J. Y. Lee, S. Seo, and L. J. Guo, "Colored ultrathin hybrid photovoltaics with high quantum efficiency," Light: Science & Applications **3**, e215 (2014).

[65] L. Hu and M. J. Serpe, "Color-tunable etalons assembled from poly (n-isopropylacrylamide) based microgels," Polymers **4**, 134-149 (2012).

[66] H. Kwon and S. Kim, "Chemically Tunable, Biocompatible, and Cost-Effective Metal–Insulator–Metal Resonators Using Silk Protein and Ultrathin Silver Films," ACS Photonics **2**, 1675-1680 (2015).

[67] K. J. Vahala, "Optical microcavities," Nature **424**, 839-846 (2003).

[68] B. Glance, "Tunable add drop optical filtering method and apparatus," (Google Patents, 1996).

[69] M. B. Frish, P. B. Keating, W. J. Kessler, and S. J. Davis, "Miniature monolithic optical add-drop multiplexer," (Google Patents, 2002).

[70] M. Moharam, T. Gaylord, E. B. Grann, and D. A. Pommet, "Formulation for stable and efficient implementation of the rigorous coupled-wave analysis of binary gratings," Journal of Optical Society of America A **12**, 1068-1076 (1995).

[71] L. Li, "New formulation of the Fourier modal method for crossed surface-relief gratings," Journal of Optical Society of America A 14, 2758-2767 (1997).

[72] M. Moharam, T. Gaylord, D. A. Pommet, and E. B. Grann, "Stable implementation of the rigorous coupled-wave analysis for surface-relief gratings: enhanced transmittance matrix approach," Journal of Optical Society of America A **12**, 1077-1086 (1995).

[73] A. D. Rakić, A. B. Djurišić, J. M. Elazar, and M. L. Majewski, "Optical properties of metallic films for vertical-cavity optoelectronic devices," Applied Optics **37**, 5271-5283 (1998).

[74] W. Choi, M.-H. Kim, Y.-J. Na, and S.-D. Lee, "Complementary transfer-assisted patterning of high-resolution heterogeneous elements on plastic substrates for flexible electronics," Organic Electronics **11**, 2026-2031 (2010).

[75] A. Carlson, A. M. Bowen, Y. Huang, R. G. Nuzzo, and J. A. Rogers, "Transfer printing techniques for materials assembly and micro/nanodevice fabrication," Advanced Materials **24**, 5284-5318 (2012).

[76] N. Yu, P. Genevet, M. A. Kats, F. Aieta, J.-P. Tetienne, F. Capasso, and Z. Gaburro, "Light propagation with phase discontinuities: generalized laws of reflection and refraction," Science **334**, 333-337 (2011).

[77] A. V. Kildishev, A. Boltasseva, and V. M. Shalaev, "Planar photonics with metasurfaces," Science **339**, 1232009 (2013).

[78] N. Yu and F. Capasso, "Flat optics with designer metasurfaces," Nature Materials **13**, 139-150 (2014).

[79] A. Mitra, H. Harutyunyan, S. Palomba, and L. Novotny, "Tuning the cavity modes of a Fabry–Perot resonator using gold nanoparticles," Optics Letters **35**, 953-955 (2010).

[80] B. Vasić and R. Gajić, "Tunable Fabry–Perot resonators with embedded graphene from terahertz to near-infrared frequencies," Optics Letters **39**, 6253-6256 (2014).

[81] A. Vázquez-Guardado, A. Safaei, S. Modak, D. Franklin, and D. Chanda, "Hybrid coupling mechanism in a system supporting high order diffraction, plasmonic, and cavity resonances," Physical Review Letters **113**, 263902 (2014).

[82] Z. Xi, Y. Lu, W. Yu, P. Yao, P. Wang, and H. Ming, "Strong coupling between plasmonic Fabry–Pérot cavity mode and magnetic plasmon," Optics Letters **38**, 1591-1593 (2013).

[83] L. Ward, "Geometric form of the equations for the phase changes on reflection and transmission at a thin absorbing film," Optics & Laser Technology **28**, 229-232 (1996).

[84] J. R. Lakowicz, "Radiative decay engineering 3. Surface plasmon-coupled directional emission," Analytical Biochemistry **324**, 153-169 (2004).

[85] W.-Y. Chen, C.-H. Lin, and W.-T. Chen, "Plasmonic phase transition and phase retardation: essential optical characteristics of localized surface plasmon resonance," Nanoscale **5**, 9950-9956 (2013).

[86] W. Rechberger, A. Hohenau, A. Leitner, J. Krenn, B. Lamprecht, and F. Aussenegg, "Optical properties of two interacting gold nanoparticles," Optics Communications **220**, 137-141 (2003).

[87] H. Tamaru, H. Kuwata, H. T. Miyazaki, and K. Miyano, "Resonant light scattering from individual Ag nanoparticles and particle pairs," Applied Physics Letters **80**, 1826-1828 (2002).

[88] S. Link, M. Mohamed, and M. El-Sayed, "Simulation of the optical absorption spectra of gold nanorods as a function of their aspect ratio and

the effect of the medium dielectric constant," The Journal of Physical Chemistry B **103**, 3073-3077 (1999).

[89] W. Ni, X. Kou, Z. Yang, and J. Wang, "Tailoring longitudinal surface plasmon wavelengths, scattering and absorption cross sections of gold nanorods," ACS Nano **2**, 677-686 (2008).

[90] Y.-Y. Yu, S.-S. Chang, C.-L. Lee, and C. C. Wang, "Gold nanorods: electrochemical synthesis and optical properties," The Journal of Physical Chemistry B **101**, 6661-6664 (1997).

[91] T. Smith and J. Guild, "The CIE colorimetric standards and their use," Transactions of the Optical Society **33**, 73 (1931).

[92] K. Liu, X. Zeng, S. Jiang, D. Ji, H. Song, N. Zhang, and Q. Gan, "A large-scale lithography-free metasurface with spectrally tunable super absorption," Nanoscale **6**, 5599-5605 (2014).

[93] Y. Zhang, T. Wei, W. Dong, K. Zhang, Y. Sun, X. Chen, and N. Dai, "Vapor-deposited amorphous metamaterials as visible near-perfect absorbers with random non-prefabricated metal nanoparticles," Scientific Reports **4** (2014).

[94] R. Santbergen, T. Temple, R. Liang, A. Smets, R. van Swaaij, and M. Zeman, "Application of plasmonic silver island films in thin-film silicon solar cells," Journal of Optics **14**, 024010 (2012).

[95] M. Yan, J. Dai, and M. Qiu, "Lithography-free broadband visible light absorber based on a mono-layer of gold nanoparticles," Journal of Optics **16**, 025002 (2014).

[96] A. Moreau, C. Ciracì, J. J. Mock, R. T. Hill, Q. Wang, B. J. Wiley, A. Chilkoti, and D. R. Smith, "Controlled-reflectance surfaces with film-coupled colloidal nanoantennas," Nature **492**, 86-89 (2012).

[97] X. Zhao, Y. Cao, F. Ito, H. H. Chen, K. Nagai, Y. H. Zhao, and Z. Z. Gu, "Colloidal crystal beads as supports for biomolecular screening," Angewandte Chemie International Edition **45**, 6835-6838 (2006).

[98] H. Lee, J. Kim, H. Kim, J. Kim, and S. Kwon, "Colour-barcoded magnetic microparticles for multiplexed bioassays," Nature Materials **9**, 745-749 (2010).

[99] B. Ye, H. Ding, Y. Cheng, H. Gu, Y. Zhao, Z. Xie, and Z. Gu, "Photonic crystal microcapsules for label-free multiplex detection," Advanced Materials **26**, 3270-3274 (2014).

[100] R. Xuan and J. Ge, "Photonic printing through the orientational tuning of photonic structures and its application to anticounterfeiting labels," Langmuir **27**, 5694-5699 (2011).

[101] H. Hu, J. Tang, H. Zhong, Z. Xi, C. Chen, and Q. Chen, "Invisible photonic printing: computer designing graphics, UV printing and shown by a magnetic field," Scientific Reports **3** (2013).

[102] P. Zijlstra, J. W. Chon, and M. Gu, "Five-dimensional optical recording mediated by surface plasmons in gold nanorods," Nature **459**, 410-413 (2009).

Publication

International journals

1. **I.-H. Lee**, E.-S. Yu, S.-U. Kim, S.-H. Lee, and S.-D. Lee, “Recording and reading dual images resolved by polarization”, to be submitted in 2016.
2. **I.-H. Lee**, E.-S. Yu, H.-J. Kim, and S.-D. Lee, “Effect of silver nanostructures on cavity mode for full-color generation in optical micro-resonator”, to be submitted in 2016.
3. H.-L. Park, **I.-H. Lee**, C.-H. Keum, S.-H. Lee, and S.-D. Lee, “Effect of morphological and physicochemical properties of dielectric-organic semiconductor interfaces on photoresponse of organic phototransistors”, Semicon. Sci. Technol. submitted (2016).
4. W.-W. Noh, S.-H. Lee, G. Lee, **I.-H. Lee**, H.-L. Park, M.-H. Kim, and S.-D. Lee, “Dependence of bias stress on hydrophobicity of gate insulator in solution-processed organic thin-film transistors”, J. Nanosci. Nanotechnol. accepted for publication (2016).
5. S.-H. Lee, **I.-H. Lee**, J. Kim, C.-H. Keum, E.-S. Yu, and S.-D. Lee, “Electrowetting-on-dielectric device controlled by embedded undulating electrode for liquid transport”, J. Nanosci. Nanotechnol. **16**, 6455 (2016).
6. **I.-H. Lee**, S.-C. Park, and S.-D. Lee, “Submicro-pillars and holes from the depth-wise Talbot images of a conical phase mask”, Opt. Express **23**, 25866 (2015).

7. S.-U. Kim, J. Kim, E.-S. Yu, **I.-H. Lee**, B.-Y. Lee, Y. Sohn, and S.-D. Lee, “Colloidal assembling template with wrinkled patterns based on liquid crystalline polymer”, Mol. Cryst. Liq. Cryst. **610**, 221 (2015).
8. Y.-S. Ryu, **I.-H. Lee**, J.-H. Suh, S.-C. Park, S. Oh, L. R. Jordan, N. J. Wittenberg, S.-H. Oh, N. L. Jeon, B. Lee, A. N. Parikh, and S.-D. Lee, “Reconstituting ring-rafts in bud-mimicking topography of model membranes”, Nat. Commun. **5**, 4507 (2014).
9. **I.-H. Lee**, S.-H. Lee, C.-H. Keum, S.-U. Kim, and S.-D. Lee, “Combinatorial color arrays based on optical mircro-resonators in monolithic architecture”, Opt. Express **22**, 15320 (2014).
10. C.-M. Keum, **I.-H. Lee**, S.-H. Lee, G.-J. Lee, M.-H. Kim, and S.-D. Lee, “Quasi-surface emission in vertical organic light-emitting transistors with network electrode”, Opt. Express **22**, 14750 (2014).
11. S.-C. Park, **I.-H. Lee**, J.-H. Na, and S.-D. Lee, “Liquid-bridging in particle self-assemblies toward constructing periodic nano-mesh structures and nano-dot arrays”, J. Appl. Phys. **114**, 154302 (2013).

Abstract (Korean)

최근, 기존 색안료의 대안으로서 구조색이 많은 관심을 받고 있다. 물질 본연의 흡광도에 의존하는 기존 발색 방법과 달리, 구조색은 나노구조에서의 광학 공진 현상에 의해 나타난다. 이에 따라 구조색은 안료와 차별화되는 다음과 같은 특징들을 가진다. 첫째, 이론적으로 어떠한 물질이라도 발색이 가능하기 때문에, 물질 선택에 제한이 상대적으로 적다. 둘째, 흡광도가 적어 전체적인 광효율이 높다. 셋째, 색화소의 크기를 회절한계까지 줄일 수 있다. 넷째, 활성물질을 이용하면 외부자극에 의한 색상 변화가 가능하다. 이러한 특징들로 인해, 구조색은 고효율의 나노 색소자 개발을 가능케 하고, 기존 안료기술로는 불가능했던 새로운 응용분야를 창출해낼 것으로 기대된다.

지금까지 구조색 구현을 위해, 크게 광학결정, 플라즈모닉 나노구조, 광학 공진기 기반의 세 가지 접근 방법이 제시되었다. 그 중에서도 광학 공진기 기반 구조색은 높은 광효율, 간단한 공정과정, 그리고 편광에 대한 의존성이 없다는 장점으로 인해 가장 유망한 접근방법으로 여겨지고 있다. 하지만, 실질적인 응용을 위해서는 해결해야 할 기술적 과제들이 있다. 첫째, 저가격, 고수율의 색요소 집적 기술 개발되어야 한다. 둘째, 각도 의존성이나 색재현도와

같은 특성들이 향상되어야 한다. 셋째, 더 넓은 응용분야에 사용되기 위해선 새로운 기능성이 부과되어야 한다.

본 논문에서는 이러한 기술적 난제를 해결하기 위해 새로운 소자구조와 공정방법을 제안하고, 이를 이용한 새로운 응용기술을 개발하였다. 먼저, 광공진층 역할을 하는 유전물질 패턴을 전사공정하는 방법을 이용하여, 대면적에 높은 수율로 색 요소를 집적할 수 있는 기술을 제안하였다. 제안된 기술을 이용하여, 광학 공진기 기반의 칼라 필터를 포함한 액정 디스플레이를 시현하였다. 둘째, 소자 특성 향상을 위하여 광공진층 내부에 금속 나노구조를 도입할 경우에 나타나는 광학 현상을 연구하였다. 그 결과, 나노구조의 기하구조에 따라, 공진 조건을 단파장 혹은 장파장으로 조절할 수 있음이 밝혀졌다. 이를 통해 정해진 두께의 광공진층에서 색재현성을 확대하고, 서로 다른 색을 집적할 수 있었다. 또한, 불연속적인 금속 나노구조를 도입한 경우 각도 의존성이 크게 줄어들어는 점을 이용하여 구부림에 대해서 색상이 변하지 않는 유연 색 소자를 구현하였다. 마지막으로, 광공진층에 액정 고분자층을 포함하여 편광에 따라 색이 변하는 소자를 개발하였다 광배향 방법을 이용하여 서로 다른 방향으로 정렬된 액정 고분자층을 포함하는 변색소자들을 대면적에 간편하게 집적할 수 있었다. 이를 통하여 서로 다른 두 가지 이미지를 같은 위치에 저장하고, 편광에

따라 구별하여 읽을 수 있는 새로운 개념의 광학 저장장치를 시현하였다.

본 논문에서 제안된 새로운 소자구조와 공정방법은 차세대 디스플레이 및 이미지 저장장치 등을 포함한 응용분야에서 구조색의 실질적 활용을 위한 초석이 될 것이다.

주요어: 구조색, 광학 공진기, 페브리-페로 공진기, 광학 정보 저장장치, 칼라필터

학번: 2012-30223